International Journal of Machine Tools & Manufacture 162 (2021) 103687

Contents lists available at ScienceDirect

International Journal of Machine Tools and Manufacture

journal homepage: http://www.elsevier.com/locate/ijmactool

Surface integrity in metal machining - Part I: Fundamentals of surface characteristics and formation mechanisms

Zhirong Liao [a], Andrea la Monaca [a], James Murray [b], Alistair Speidel [b], Dmitrii Ushmaev [a], Adam Clare [b,c], Dragos Axinte [a,c,*], Rachid M'Saoubi [d]

[a] Machining and Condition Monitoring Group, University of Nottingham, UK
[b] Advanced Component Engineering Laboratory, University of Nottingham, UK
[c] Faculty of Engineering, University of Nottingham, Ningbo, China
[d] R&D Material and Technology Development, Seco Tools AB, SE-73782, Fagersta, Sweden

ARTICLE INFO

Keywords:
Metal machining
Surface integrity
Microstructural alterations
Materials characterisation
Post processing

ABSTRACT

The surface integrity of machined metal components is critical to their in-service functionality, longevity and overall performance. Surface defects induced by machining operations vary from the nano to macro scale, which cause microstructural, mechanical and chemical effects. Hence, they require advanced evaluation and post processing techniques. While surface integrity varies significantly across the range of machining processes, this paper explores the state-of-the-art of surface integrity research with an emphasis on their governing mechanisms and emerging evaluation approaches. In this review, removal mechanisms are grouped by their primary energy transfer mechanisms; mechanical, thermal and chemical based. Accordingly, the resultant multi-scale phenomena associated with metal machining are analyzed. The contribution of these material removal mechanisms to the workpiece surfaces/subsurface characteristics is reviewed. Post-processing options for the mitigation of induced surface defects are also discussed.

1. Introduction

Machining generates final component geometries by exploiting a range of physical effects, which can be generically described as mechanical, thermal and chemical loadings, as well as various combinations of these mechanisms (Fig. 1). Due to the nature of the material removal mechanisms in these machining processes, surface damage is inevitable at macro and micro scales [1]. These surface alterations, which include changes to surface topography (e.g. surface roughness and waviness) [2], metallurgical state (e.g. microstructure and micro-defects) [3,4], mechanical characteristics (e.g. microhardness and residual stresses) and chemical state (e.g. reaction layers) [5,6], on the machined surface and in the sub-surface layer, are considered under the generic umbrella term of surface integrity [7]. The formation mechanisms of these surface defects (anomalies) originate from the external and internal loads (mechanical, thermal, chemical) that act on the workpiece material during machining, which cause physical or chemical changes to the workpiece material [8].

It is well known that poor surface integrity is detrimental to the functional performance characteristics (e.g. fatigue, creep, corrosion and wear resistance) of manufactured components. This is of particular importance when machining high performance metals such as superalloys and hardened steels since they are widely used for high value, high performance components in industries such as aerospace, biomedical and automotive [9,10]. Generally, machining-induced residual stresses and surface roughness largely affect high cycle fatigue (HCF) lifetimes, while they have a much lower impact on low cycle fatigue (LCF) [11]. However, surface defects (e.g. grain deformation, cracks and white layer) can affect fatigue performance under both LCF/HCF regimes [12,13]. For instance, white layers on the surface of Ni-superalloys generated by mechanical machining can lead to a 40% reduction in LCF lifetime [13]. This is important for safety critical applications, e.g. the aeroengine industry, whereby safety criteria are defined around properties such as fatigue; hence an understanding of surface integrity is needed here.

With increasing demand for high component performance, significant efforts have been made at academic and industrial levels in recent years, to elucidate the mechanisms of surface defect generation during

* Corresponding author. Machining and Condition Monitoring Group, University of Nottingham, UK.
E-mail address: dragos.axinte@nottingham.ac.uk (D. Axinte).

https://doi.org/10.1016/j.ijmachtools.2020.103687
Received 6 October 2020; Received in revised form 13 December 2020; Accepted 13 December 2020
Available online 30 December 2020

machining and their influence on component functional performance, as well as to develop methods to reduce this damage. In general, the extent and magnitude of these surface defects depends on the machining conditions, e.g. machining parameters, tool wear and cutting fluid application [14–17]. Generally, by applying 'gentle/softer' machining conditions, such as small depths of cut and low feed speeds, higher surface integrity can be generated, however this leads to increased machining costs (e.g. tooling and human resources) and lower productivity caused by lower material removal rates. However, in some situations, reducing certain process parameters can also detrimentally affect surface integrity (e.g. cutting edge ploughing effects at very low depth of cut without shearing the material). While surface alterations cannot be avoided during machining processes, in industrial applications, companies typically have their own standards to quantify these surface anomalies to optimise manufacturing costs and maximise component performance. However, setting up surface integrity standards over the full range of machining conditions and operations requires significant resource allocation [18]. Nevertheless, while aggressive cutting conditions are applied to maximise material removal rates, different post-processing techniques are also applied to reduce or remove surface anomalies, thus mitigating further machining costs and improving component performance.

Metal machining processes are applied to a wide range of materials and involve a range of material removal phenomena for different functional components/products, as shown in Fig. 1. While existing reviews mainly focus on surface characterisation after particular operations (e.g. conventional machining only [19,20]) or materials (e.g. nickel/titanium-base superalloys [18,21]), the relationship between the physical mechanisms of surface integrity generation and the different loading regimes (e.g. mechanical/thermal/chemical) induced by machining operations have not been addressed in these reports. Hence, Part I of this review paper presents a scientific investigation of the surface and subsurface alterations induced by different machining methods and details the state-of-the-art in the nature of metal

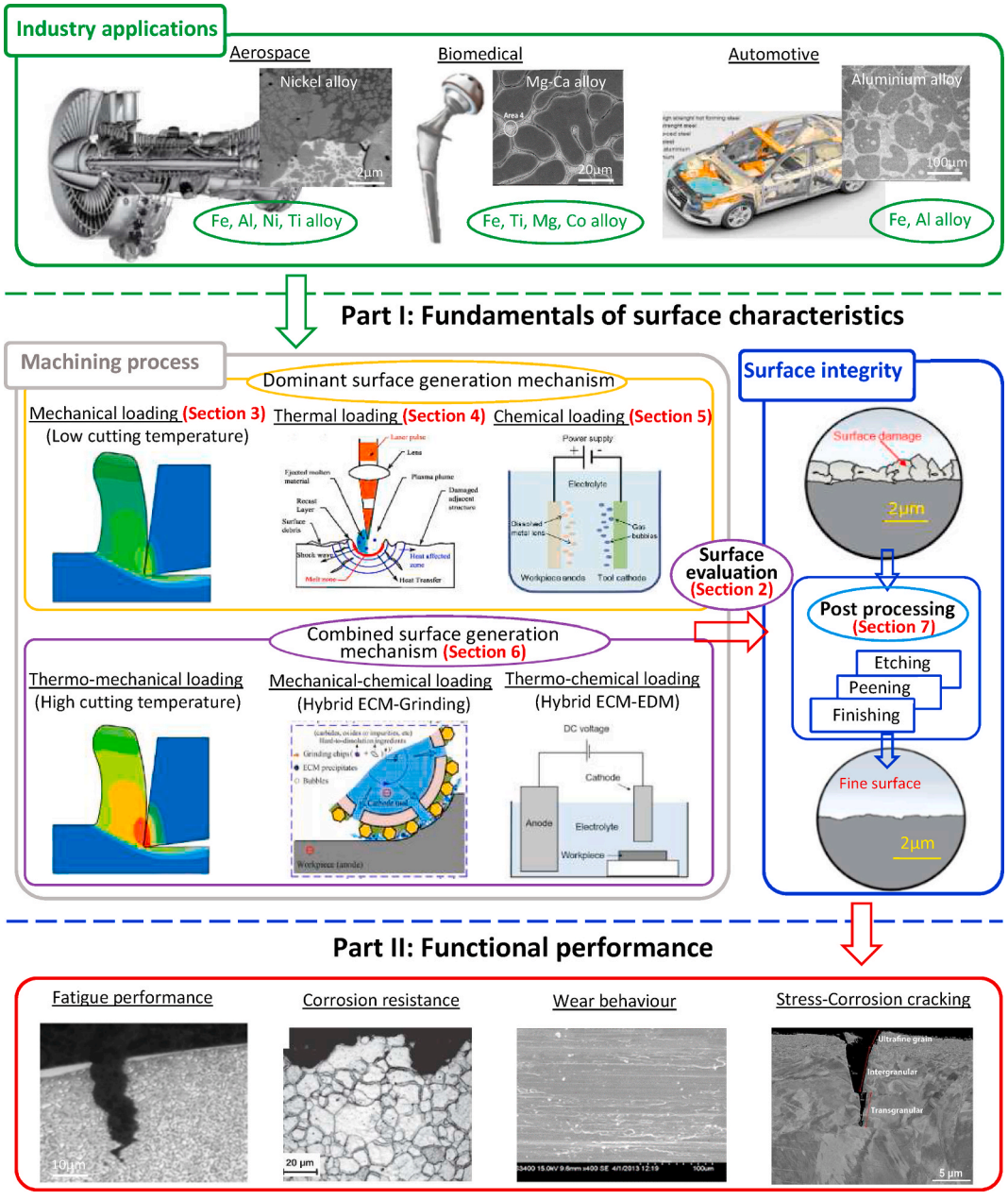

Fig. 1. Surface integrity and formation mechanisms induced by different metal material removal processes and their influences in functional performance [5,22–35].

machining-induced surface integrity. This is aimed at providing an in-depth understanding of the physics that govern the generation of surface alterations/defects in machining based on the outcomes of mechanical, thermal, chemical and combined loading, which machining processes induce on a workpiece surface/near surface, as shown in Fig. 1. This not only includes recent advances in surface characterisation methods (e.g. microstructural, mechanical and chemical characterisation), but also the material removal mechanisms that drive the resulting surface alterations. Furthermore, a range of viable post processing solutions for removing, reducing and nullifying the surface defects have also been studied to support their further application. On this basis, a Part II investigation on the influence of surface integrity upon component functional performance will also be conducted, also shown in Fig. 1.

2. Mechanisms of surface generation and methods for integrity evaluation

2.1. Surface generation mechanisms

Machining includes various techniques employing different physical mechanisms to remove material from the workpiece. These expose the workpiece material to mechanical, thermal and chemical loads, which result in the machined workpiece exhibiting various surface and subsurface alterations, hence modifying surface integrity [36]. Depending on the nature of the loads induced by machining upon the workpiece material, the generation of these surface alterations over different scales (Fig. 2), is driven by the following mechanisms:

Mechanical dominant mechanism: This includes processes where the surface generation mechanism is primarily determined by mechanical loading, including conventional processes such as turning, drilling, milling, grinding and polishing [37–40], as well as nonconventional processes such as plain or abrasive water/air jet machining [41]. It is notable that although conventional mechanical machining was defined as a thermo-mechanical process [42,43], thermal damage does not always occur at the machined surface. Hence, in this paper the mechanical dominant mechanism refers to those processes at low cutting temperatures, where surface integrity is not influenced by thermal effects. This normally occurs at low material removal rates with abundant/intensive application of coolant [44], for which the resultant cutting temperature is kept relatively low and the influence of heat on the surface integrity is negligible. Hence, mechanically induced surface defects (e.g. grain deformation and scratches shown in Fig. 2) are dominant. With mechanical loading applied, resulting surface damage depths can cover a wide range of length scales from the micron (e.g. finishing) to the millimetre (roughing) scale.

Thermal dominant mechanism: This includes processes that remove material by melting or vaporizing the workpiece, through sparks, e.g. electric discharge machining (EDM) [45,46], or high energy beams, e.g. laser beam machining (LBM) [47,48], shown in Fig. 2. Under these material removal processes, the surface damage is normally induced by thermal loading, whereby the dimension of defects is within the microns to hundreds of microns scale defined by melt formation and associated microstructural changes.

Chemical dominant mechanism: This includes processes that mainly employ chemical dissolution or electrolysis to remove material, such as electrochemical machining [49,50]. Surface damage results from the chemical action between the solution and the workpiece, although the chemical effect does not typically penetrate deeply beneath the surface. Hence, surface damage is usually below the micron scale.

Combined loading mechanism: This is usually achieved by combining two (or more) different material removal modalities, often conventional machining (mechanical loading) and nonconventional machining (thermal/chemical loading) to improve workpiece machinability, e.g. laser assisted machining (LAM), electrochemical discharge machining or electrochemical grinding [51–53]. In these scenarios, the combination of modalities can not only enhance the machining process, but can also improve surface integrity. However, in some singular processes (e.g. conventional machining with aggressive cutting conditions), due to the transformation of mechanical energy into thermal energy, combined thermo-mechanical loading can also occur where a high cutting temperature is yielded [54,55]. This can occur in a wide range of machining conditions, but especially in conditions of low thermal conductivity of workpiece and/or tooling, limiting heat dissipation during cutting, enabling severe plastic deformation with a phase transition in the workpiece, shown in Fig. 2.

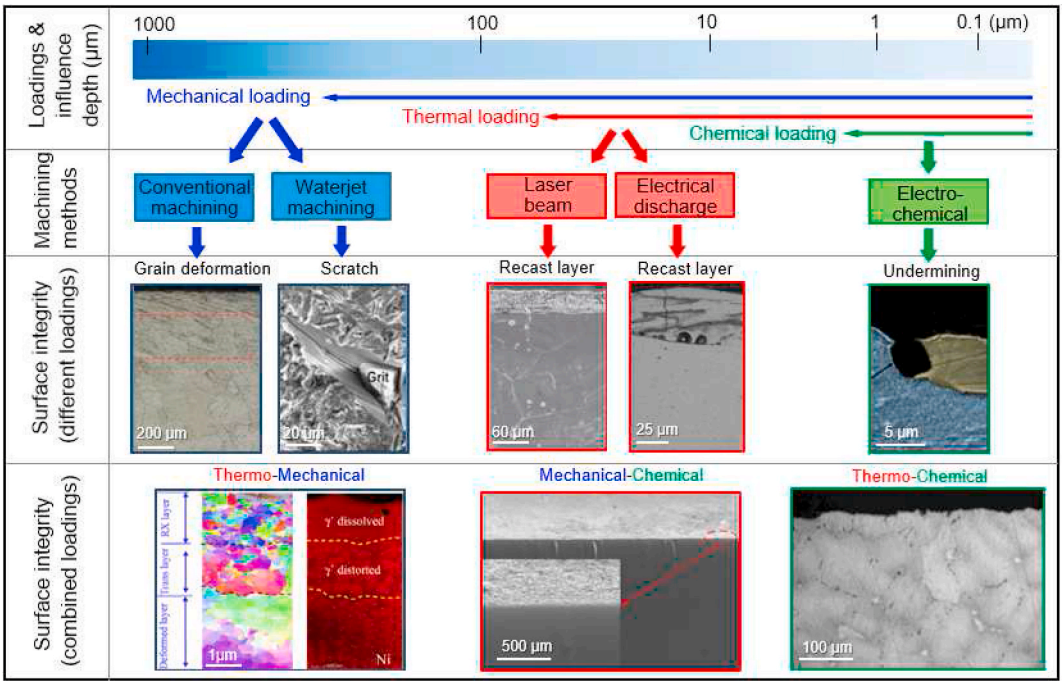

Fig. 2. Classifications and scales of surface integrity and their formation mechanisms with corresponding different loadings and machining methods [23,56–60].

2.2. Emerging approaches in surface integrity evaluation

2.2.1. Advances in the microstructural characterisation of machined surfaces

A material's microstructure determines its macroscopic behaviour and mechanical response [61]. Depending on the mechanisms through which material is removed in a particular machining operation, different microstructural alterations may be induced in the near-surface [62].

For standard metallographic inspection, machined surfaces are sectioned and polished through subsequent steps to a smooth finish that can enable microscopic observation. To reveal the presence of different phases or grain boundaries, chemical, ion, or electrochemical etching strategies can be used. Optical microscopy (OM) can reveal the presence of machining-induced material deformation in the form of white layers (WL) or highly strained swept grain structures, which appear clearly when distorted areas are relatively thick, shown in Fig. 3 (a) for the case of Ti–6Al–4V after a mechanical milling operation [63]. OM finds extensive application in surface integrity assessment in industrial contexts. However, OM alone is often insufficient to collect high-resolution surface integrity data at the microstructural scale.

To perform high-magnification imaging, scanning electron microscopy (SEM) can provide smaller-scale information. The two main imaging modes commonly employed within SEM are secondary electron (SE) and backscatter electron (BSE) detection, shown in Fig. 3 (b)–(c) for surfaces generated by laser and mechanical drilling, respectively. For general surface inspection, SE and BSE modes can often be used interchangeably as their imaging output is in many ways similar in showing the main features of machined surfaces. However, as SE and BSE

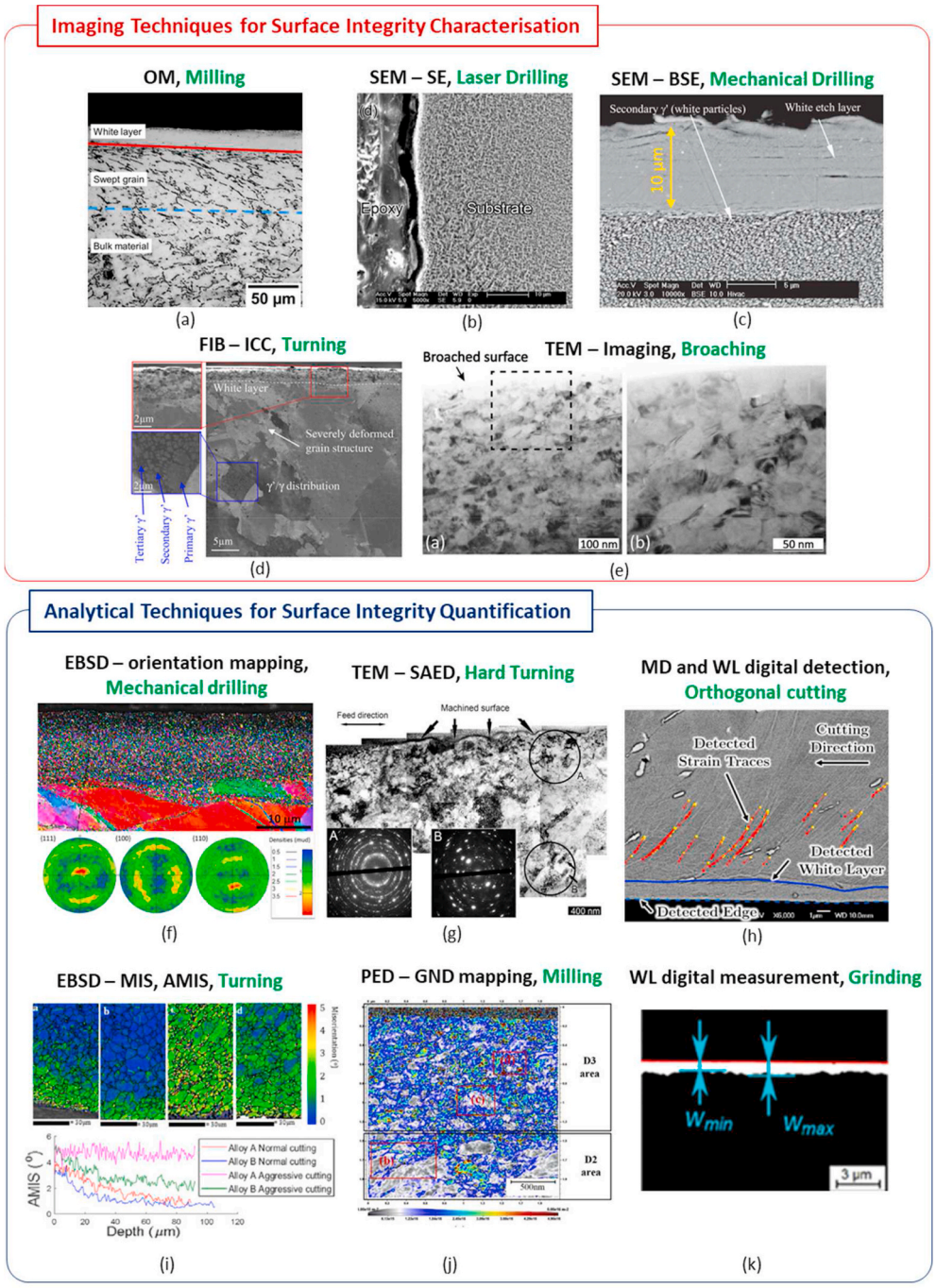

Fig. 3. Example of machined surface integrity analysis and quantification through different techniques. (a) Optical microscopy [63]. (b) SEM – SE Imaging [6]. (c) SEM – BSE Imaging [64]. (d) FIB – Ion contrast channelling [65]. (e) TEM – Imaging [68]. (f) EBSD mapping – Inverse pole figures and pole figures [71]. (g) TEM – SAED analysis [70]. (h) Digital surface integrity analysis – detection of material drag and white layers [72]. (i) EBSD mapping – Misorientation mapping and AMIS plots [30]. (j) PED – GND mapping [73]. (k) Digital measurement of WL's [74].

imaging give rise to different levels of atomic mass contrast and electrons are produced from different depths in the sample interaction volume. SE micrographs tend to enhance topographical aspects of the surface being observed, and detection of secondary electrons can be more efficient when surface features are to be reconstructed compared to backscattered ones. Hence, SE imaging is convenient when morphological aspects are of interest (e.g. micro-cracks and burrs). On the other hand, backscattered electrons are elastically scattered from the nucleus of atoms at greater depths of the interaction volume and BSE imaging provides atomic mass contrast in the scanned area. BSE is particularly convenient when studying machined surfaces to highlight the presence of different metallurgical phases in strain-affected microstructures.

As understanding the micro and nanoscale material state after machining processes has gained significant interest, other advanced microscopy techniques have been applied to assess machining-induced surface integrity.

Focused ion beam (FIB) microscopy enables imaging through ion contrast channelling, which can reveal the presence and extent of plastic deformation in the machined sub-surface [64]. It can reveal changes in grain morphology and size, shown in Fig. 3 (d), where white layers and grain deformation can be observed in the turned subsurface of a Ni-base superalloy [65]. FIB can also deliver sufficient energy to selectively mill small portions of the workpiece, allowing the generation of lamellae with sub 200 nm thickness. These can be used for very high magnification electron imaging with transmission election microscopy (TEM).

Although TEM has been employed for many years in material science, its application to studying surface integrity after machining is relatively recent and growing, enabling understanding of surface integrity at the sub-micron scale. In fact, TEM imaging on the near atomic scale allows the observation of subtle sub-granular defects in the crystal lattice, which cannot be captured by SEM. TEM has enabled the characterisation of ultra-fine grain structures locally induced by machining processes, such as drilling [66], turning [67], or broaching [68] as shown in Fig. 3 (e). TEM also allows quantitative understanding of local crystal lattice parameters through analysis of the so-called selected area electron diffraction (SAED) patterns. As shown in Fig. 3 (g), TEM is applied to investigate machining-induced surfaces to elucidate the different crystallographic structures present in highly-strained machined layers [69,70].

Electron backscatter diffraction (EBSD) is perhaps the most practical and detailed method for spatially characterising and quantifying material microstructures from the μm to the mm scale. EBSD provides detailed information on the crystallographic state, orientation and texture induced by machining processes, e.g. as a consequence of plastic deformation induced by mechanical material removal [71,75], shown in Fig. 3 (f) for the case of aggressive drilling of the advanced Ni-base superalloy RR1000. Misorientation analysis of EBSD data can also provide quantitative information on the relative differences in crystallographic angle in machining-affected regions, shown in Fig. 3 (i). The thickness of material exhibiting high lattice distortion in EBSD analysis has been shown to match well with layers displaying microstructural deformation apparent in SEM imaging [72]. Furthermore, a relevant technique to understand the severity of plastic deformation induced in the workpiece sub-surfaces involves the calculation of the average intra-grain misorientation (AMIS) profile from EBSD orientation maps. When analysing EBSD map data from material sites presenting machining-induced microstructural deformation, the AMIS over M grains belonging to a line of N points can be expressed as in Eq. (1), where Θ_{jk} represents the misorientation angle existing between two points j and k within the grain i [76].

$$AMIS = \frac{\sum_{i=1}^{M} \left(\frac{1}{2} \frac{\sum_{j}^{N} \sum_{k}^{j} \theta_{jk}}{N_i} \right)_{grain(i)}}{M} \quad (1)$$

In this context, large AMIS values indicate the presence and extent of microstructural distortion induced by the machining process, with the AMIS trend decreasing when moving away from the machined free-surfaces towards the bulk material [30,76,77]. Nevertheless, severe deformation states that can be induced by machining processes lead to high levels of lattice distortion. This challenges diffraction pattern indexing at the most strained surface locations, even when small step sizes are used (typically below 100 nm [30,72]). Hence, subsequent post-processing techniques (e.g. noise reduction or filling) might be needed in some cases to improve the map data. Thus, EBSD analysis of machined surface layers is often unable to quantify machining-induced plastic strain in absolute values. Nevertheless, in most cases this technique still allows a convincing distinction between machining-affected areas and un-deformed material sites, by identification of the subsurface areas where lattice distortion is predominant. More advanced techniques for grain orientation mapping in the machined surfaces can be performed through electron transmission in the SEM, using transmission Kikuchi diffraction (TKD) analysis [65,78], or in a TEM environment, through precession electron diffraction (PED) mapping [73]. Although the output datasets given by these techniques are similar, there are fundamental differences in complexity, sample preparation technique and range of application of these techniques. While TKD and PED require FIB lamellae for material analysis, EBSD can be performed on fine polished surfaces. However, EBSD indexing is challenged by severely strained machining-induced nano-crystalline structures. As such, it is often difficult to completely quantify the metallurgical state. In this context, TKD and PED strategies can provide better nanoscale indexing, but observation regions are limited to areas of a few μm^2. Furthermore, when analysing highly-strained regions, the distribution of geometrically necessary dislocations (GNDs) can be obtained from lattice orientation maps [79]. In the context of surface integrity, emerging approaches have now adopted GND density mapping to reveal the nanoscale mechanisms of surface plastic deformation in relationship to the machining-induced condition, as shown in Fig. 3 (j) for the case of a milled surface indexed through PED [73]. In parallel to the application of more advanced material science techniques for the understanding of machined surfaces, such as development of a tri-beam system incorporating a femtosecond laser into a FIB set-up [80], the surface integrity community is adopting approaches from other developing engineering fields, such as computer science and digital data analysis. Fig. 3 (h) shows the development of a digital approach to automatically identify the presence of machining-induced deformation in the form of material drag (MD) or white layers (WL) resulting from mechanical material removal [72]. Similarly, digital approaches have been developed also in the context of grinding-induced white layers [74], as in Fig. 3 (k), and grain size and phase content resulting from milling of Ti–6Al–4V [81]. As the development of digital techniques for the automation of engineering tasks is accelerating in many disciplines, in particular in materials science, their application within the machining community will further grow with the development of next-generation approaches for surface integrity investigation.

Thus, a wide spectrum of techniques is available to enable microstructural analysis of machined surfaces. As summarised in Table 1, selection of a suitable surface integrity characterisation approach should be carried out considering the effects of the surface features to be investigated and their typical lengths. In fact, the existing strive to investigate the metallurgy of machined surfaces on ever smaller scales coexists with the necessity of ensuring that such properties are representative of the surface condition, which plays a crucial role especially when focusing on material sites of small scale. Hence, emerging approaches for characterisation of machining-induced surface integrity should still rely on well-established research techniques, which represent a fundamental basis for future investigations aiming at analysing the properties of machined surfaces on ever smaller scales.

2.2.2. Mechanical characterisation

Mechanical properties of machining-induced surface layers, such as

Table 1
The main characteristics of widely employed research techniques for microstructural analysis of machining-induced surface integrity. In particular: applicable length scales, benefits, limitations and features of interests are discussed for each technique.

Length scale [m]	Microstructural Surface Integrity analysis technique	Benefits	Limitations	Machining-induced microstructural features
10^{-3} – 10^{-4}	Optical Microscopy (OM)	Fastest implementation; Lowest complexity; Limited costs;	Limited level of detail; Very limited magnification;	Imaging of micro-scale machining anomalies, e.g. Material Drag [64,72], White layers [82–84], Micro-cracks [32,85], Corrosion pits [82,86], etc.
10^{-4} – 10^{-5}	Secondary Electron Microscopy (SEM)	Low complexity; Good level of detail;	Limited beam stability; Moderate magnifications;	
10^{-4} – 10^{-6}	Field Emission Gun -SEM (FEG-SEM)	Higher magnifications and better beam stability than standard SEM;	Higher costs and operational complexity than standard SEM;	
10^{-4} – 10^{-7}	Ion Contrast Channelling (ICC)	Better channelling contrast than electrons		
10^{-4} – 10^{-8}	Electron Backscatter Diffraction (EBSD)	High-detail analysis of material lattice condition	High implementation complexity; Long scanning times; Reduced extent of observable material sites;	Orientation mapping and texture analysis [71,72,75,87] Misorientation map analysis [30,76];
10^{-5} – 10^{-8}	Transmission Kikuchi Diffraction (TKD)	Higher indexing accuracy than EBSD;	Very high implementation complexity; Onerous sample preparation through FIB milling;	GNDs calculation [73];
10^{-5} – 10^{-9}	Precession Electron Diffraction (PED)	Highest-nanoscale accuracy and resolution;	Most limited in extent of observable material sites;	
10^{-5} – 10^{-9}	Transmission Electron Microscopy (TEM)	Highest magnifications; Allows nanoscale crystallographic analysis;		Imaging of nano-scale machining-induced features (e.g. nanocrystalline layers) [65,70,88]

micro-hardness, residual stresses and micro-mechanical material behaviour are critical to the functional performance of the overall component. In fact, because of the strain induced by material removal processes to the machined workpiece microstructure, significant changes in its elasto-plastic mechanical behaviour can be induced at the micro and nanoscales. Therefore, micro- and nano-hardness represents a key surface integrity metric providing relevant indications of the surface metallurgical condition, affecting the in-service performance of machined parts. Surface hardness testing can be performed at different scales, with indentation hardness protocols similar to well-known macro-hardness approaches e.g. Vickers, Knoop, Brinnel. As machining processes can induce intensive thermo-mechanical gradients in the workpiece volume, a steep variation of their mechanical properties can be produced in the vicinity of the new surface. Approaches to evaluate the subsurface hardness of machined workpieces are hence designed to characterise their mechanical response over length-scales typically in the range of 1 μm–100 μm [89,90].

To further understand the nature of machining-induced material layers resulting from the localised loading conditions under which they are generated, advanced approaches have been developed to investigate and characterise the nano-hardness induced by material removal up to the sub-micron scale. In the presence of severe grain refinement and recrystallization induced by machining processes, micro-hardness approaches only allow measurements taken on a relatively large number of grains. In these cases, nano-hardness techniques enable the investigation of machining-induced layers and extracting their mechanical response in much more detail, as shown in Fig. 4 (a) for the analysis of machined and burnished subsurfaces [91], and in Fig. 4 (b)–(c) for the case of broaching-induced white layers [68].

Micro-pillar compression testing has been successfully demonstrated for micro-mechanical characterisation of machining-induced layers. As shown in Fig. 4 (d), testing requires the preparation of microscale "pillars" (e.g. through FIB milling), which are then loaded under uniaxial compression conditions to reveal the failure mechanism and plastic response of highly strained regions that can be induced by machining, as shown in Fig. 4 (e) for an advanced Ni-base superalloy [30]. Hence, this approach not only provides a deep understanding on the metallurgy of machining-induced layers, and allows relation of such properties to the macroscale component load-bearing performance and failure mechanism.

A well-established approach for the analysis of the mechanical condition of machined surfaces is represented by analysis of the residual stress (RS) field. As RS can influence component performance, understanding the magnitude and extent of RS-affected region represents a primary aspect of machined surface integrity assessment. Different machining effects (e.g. mechanical, thermal, thermo-mechanical) can induce characteristic RS distributions beneath machined surfaces. Measurement of machining-induced RS states can be performed by means of different strategies, which can be broadly categorised as destructive, semi-destructive and non-destructive [92]. The selection of the residual stress measurement technique depends on the information required (e.g. surface vs. through-thickness analysis, macroscopic vs. microscopic evaluation) and on the measurement application context (e.g. laboratory analysis or on-site applications). Techniques that can be applied in a non-destructive way (e.g. neutron diffraction, X-ray diffraction) are used in several applied and academic contexts and are necessary when the integrity of the machined workpiece must be retained. Specifically, X-ray diffraction (XRD) allows the mapping of RS in the machined workpiece subsurface with typical penetration depths in the range of 10–20 μm.This technique can also be employed in a destructive way to map the machining-induced residual stress field at greater depths. To this aim, electro-polishing can be used to remove subsequent layers of material and carry out measurements at deeper subsurface sites. XRD is one of the most-widely employed techniques for measurements of the RS state of machined surfaces, shown in Fig. 4 (g)–(h) where the hoop (Fig. 4 (g)) and axial (Fig. 4 (h)) RS field induced by mechanical hole-making have been linked to the workpiece microstructural surface integrity from SEM analysis (e.g. the white layer in Fig. 4 (f)) [84]. Further approaches with increasing applications for RS analysis in machined surfaces include synchrotron diffraction and neutron diffraction strategies [93], with continuous focus being placed on the development and improvement of existing and emerging techniques to validate the importance of the RS state on surface integrity for its primary role in the functional performance of machined parts.

The most-widely employed research techniques discussed in sections 2.2.1 and 2.2.2 allow destructive microstructural and mechanical characterisation of machined surfaces. Nevertheless, it should be noted that non-destructive testing (NDT) strategies are applied to characterise machining-induced surface integrity. One of the most relevant approaches is represented by Barkhausen noise (BN) techniques, which enable the detection of surface anomalies through analysis of domain wall (DWs) motion under surface magnetisation cycles [94]. In this context, BN analysis represents a relevant research strategy to study machining-induced surface integrity, e.g. in presence of milling-induced

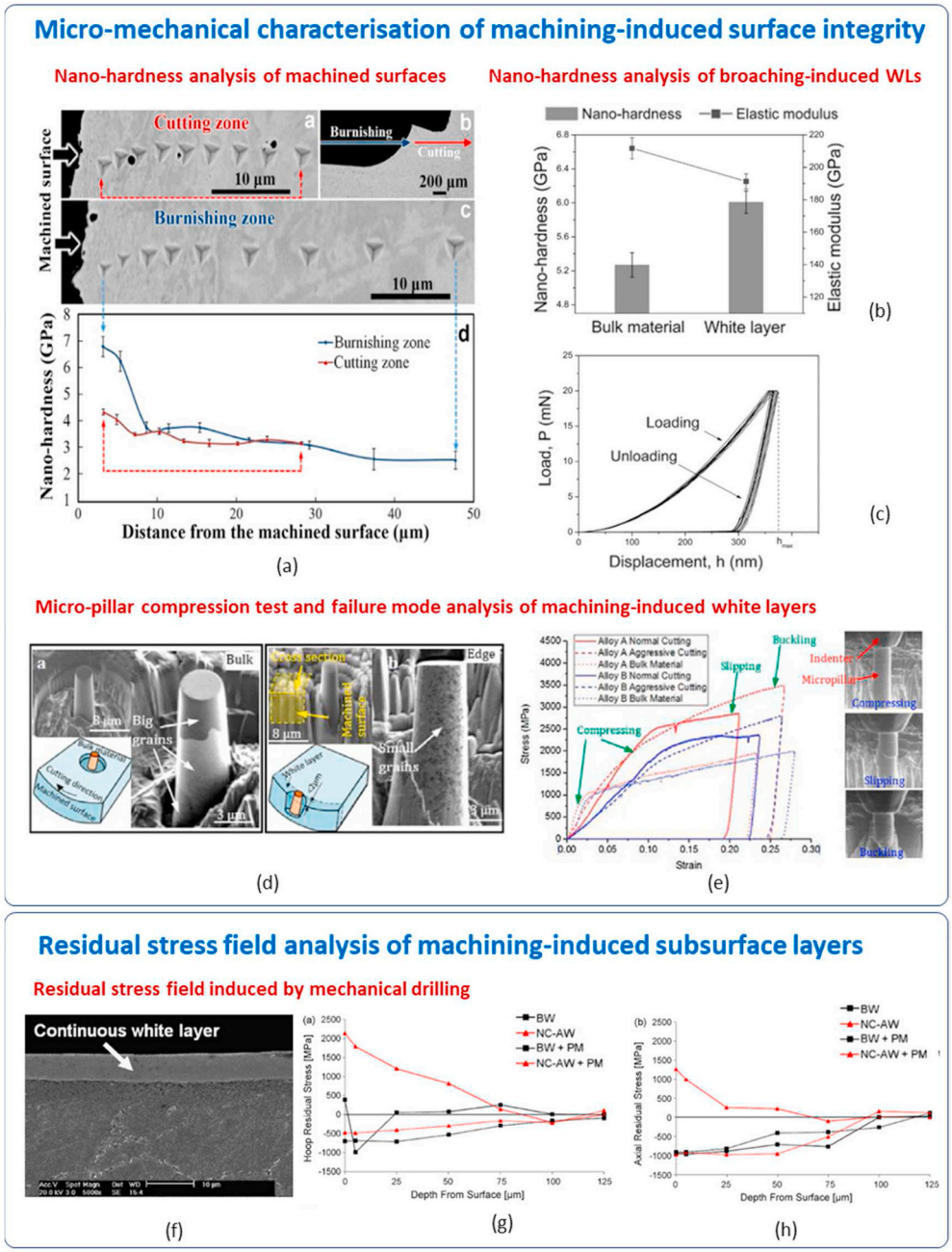

Fig. 4. (a) Nano-indentation and nano-hardness analysis of machined and burnished subsurface [91]. (b) Nano-hardness analysis of broaching-induced white layers [68]; (c) Load-displacement curves from nano-indentation testing of broached-induced layers [68]; (d) Micro-pillar geometry prior to testing for bulk material and near-surface white (recrystallised) layer regions induced by mechanical machining [30]; (e) Stress-strain characteristic obtained by micro-pillar compression testing to reveal the subsurface micro-mechanical behaviour [30]; (f) Continuous white layer induced by abusive drilling [84]; (g) Hoop RS profile [84]; (h) Axial RS profile [84] after different hole making operations in a Ni-base superalloy.

WLs [95], or heat-affected zones (HAZs) induced by grinding [96]. Therefore, NDT techniques can improve surface integrity assessment after machining and enable new research and development opportunities from both industrial and academic perspectives.

2.2.3. *Chemical characterisation*

Machining not only changes the microstructure and mechanical properties of the surface, but can also change both local composition and phases. Hence, chemical characterisation is also critical to understanding of surface integrity. Techniques which characterise surface chemistry reveal the elemental composition as well as chemical bonding of the machined layer. These can affect many properties of the final part, including mechanical and corrosive attributes. The techniques described in this section include energy dispersive X-ray spectroscopy, electron energy loss spectroscopy (EELS) electron probe micro-analysis (EPMA), X-ray diffraction, backscattered scanning electron microscopy and X-ray photoelectron spectroscopy.

Energy dispersive X-ray spectroscopy (EDX) is perhaps the most widely used chemical analysis technique in the field of machining, given it is available within many scanning electron microscopes [97]. By interrogating small material volumes (down to a few cubic microns) in the near surface, the technique can be used to rapidly map qualitative elemental distributions across surfaces by rastering the electron beam, or more targeted quantitative composition measurement. It should be noted that given the interaction volume associated with EDX (approximately 5 μm at 20 kV), improper conclusions can easily be made, and therefore reducing accelerating voltage may be necessary to limit the volume of interaction to that of interest, although quantitative analysis may suffer in this case. Due to the interaction volume, cross-sectional analysis may yield more accurate information than from the top surface. In EDX, characteristic X-rays generated by interactions between electrons and atoms are weighted and used to quantitatively and qualitatively assess the composition of materials. EDX is challenged when detecting low atomic number elements, as the ratio of Auger electrons to

X-ray photons yielded becomes significant enough to affect quantification. This ratio of X-rays to Auger electrons is known as fluorescence yield. In theory, all elements except, H, He and Li are identifiable [98]. However in practice, many instruments are not suited to detects elements with Z < 11 [99]). Qualitative analysis of lower atomic numbers however is still valid. EDX has become a staple chemical characterisation technique and would generally be the first port of call for identifying composition and contamination in machined layers. Since the technique is dependent on X-rays generated from incident electrons, EDX is also commonly used in TEM systems. The high resolution of TEM combined with EDX allows elements at very small scales to be identified, at the cost of a relatively complex sample preparation procedure. For example, Fig. 5 (a) reveals discrete deposits of tool electrode contaminants in the EDM surface of single crystal silicon. For assessment of carbon as well as other light elements, electron energy loss spectroscopy (EELS) is useful. Loss of energy of primary beam electrons, via inelastic interaction with electrons from the sample, can provide information regarding the composition, stoichiometry and bonding states of the sample [100]. Klink for example used EELS to determine the location and extent of graphitization of the surface layer of a wire-EDM machined grinding wheel [101]. Pacella et al. also used EELS in a TEM in the same manner to characterise the extent of graphitization of a laser ablated diamond composite [102].

X-ray diffraction (XRD) is commonly used to characterise the phase structure of mechanically and thermally machined surfaces. For example, XRD has been used to characterise and quantify the microstructural/phase transformations taking place in the mechanical machining induced white layers in Ti–6Al–4V [63], and for ED-machined metals [105]. An example of microstructural texturing, i.e. phase structure with a preferential orientation induced by mechanical milling of Ti–6Al–4V is shown in Fig. 5. XRD is a powerful materials characterisation technique for determining the crystal structure of typically polycrystalline materials [106]. It can also be used to detect changes in overall grain orientation (texture)in polycrystalline samples. Normal XRD typically has a significant penetration depth (1–10+ μm depending on material), and therefore care should be taken when assessing thin layers, or layers with multiple areas of interest. Grazing incidence XRD is an adaptation which may be considered assessing the very near surface of the sample (10s of nm depth).

Electron probe micro-analysis (EPMA) is another useful analysis

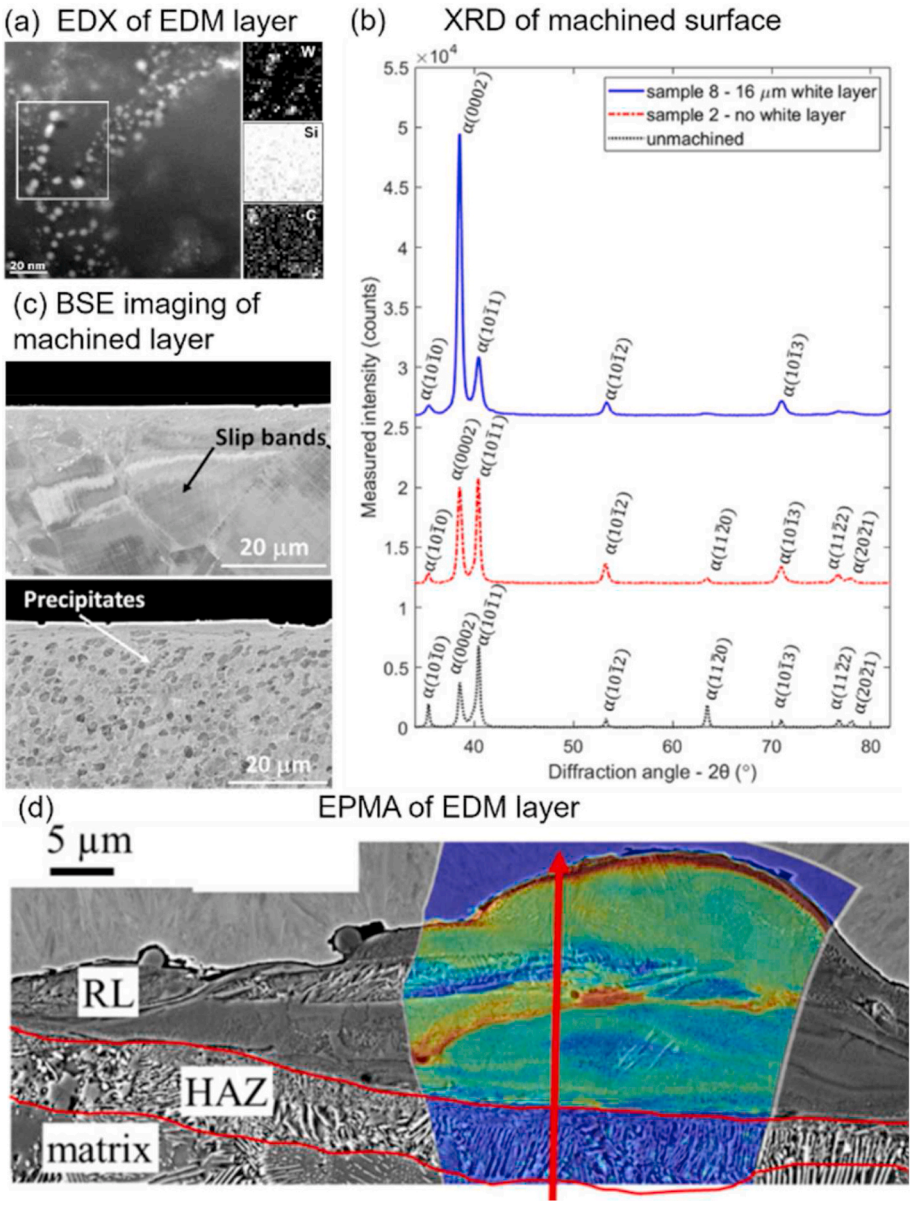

Fig. 5. (a) EDX using TEM of an EDM'd surface of single crystal silicon, revealing nano-scale deposition in a silicon workpiece during EDM [103] (b) Example of slip bands as well as precipitates easily identifiable using back-scattered electron imaging of a nickel-base alloy after abusive drilling [71] and (c) An example of preferential phase orientation induced by mechanical milling of Ti–6Al–4V [63] (d) EPMA map of carbon in the EDM recast layer with superior accuracy [104]. (For interpretation of the references to colour in this figure legend, the reader is referred to the Web version of this article.)

technique for the characterisation of the chemical composition of machined surfaces for example, recast layers produced by laser drilling of stainless steel [107]. The technique was used to determine the level of absorption of different assist gases (oxygen, argon and nitrogen). This would be challenging without EPMA given its better resolution at lower atomic numbers. In addition, it has been to map carbon in the EDM recast layer [104] (Fig. 5 (b)). Better resolution, particularly for low atomic number elements is produced by EPMA, hence the technique is appropriate for the assessment of uptake of carbon into the workpiece superficial layer from the dielectric during EDM. In the case of the recast layer in Fig. 5 (b) carbon is particularly concentrated at the edges of the re-melted material; however, it is clear that carbon still penetrates the entire recast layer. EPMA systems are similar to electron microscopes. A sample is bombarded with an electron beam, and X-rays at wavelengths characteristic to elements are emitted. Typically, wavelength dispersive spectroscopy (WDS) is performed in an EPMA system, whereby wavelengths of X-rays can be measured with greater accuracy, at an order of magnitude better accuracy, and for a larger range of lighter elements, than EDX.

Section 2.1 described the widespread use of scanning electron microscope imaging as well as backscattered electron (BSE) imaging. While secondary electron imaging allows topography imaging, BSE imaging offers a powerful, versatile tool to rapidly qualify compositional differences. Despite not offering an objective, quantifiable method for measuring composition, BSE is a highly useful method in identifying the location of precipitates for example, without having to etch the sample. This means the process is widely used for identifying recast and white layers. Examples of some structures in a severely plastically deformed nickel alloy by drilling [71], identifiable using simple BSE cross-sectional imaging are shown in Fig. 5 (e). BSE images typically do not offer as good topographic contrast and therefore it is advised to image the same location in secondary electron mode also to pair the elemental contrast with topographical features.

X-ray photoelectron spectroscopy (XPS) is an analytical tool used to measure elemental composition as well as, chemical and electronic state of the elements on the surface of a material (less than 10 nm) [108], compared to EDX which has a typical analysis depth of 1–3 μm. XPS data are obtained via irradiation of a material with an X-ray beam, while measuring the kinetic energy and number of electrons ejected from the top ~10 nm of the target material. By measuring the kinetic energy of the emitted electrons, it is possible to determine which surface elements and their chemical and electronic state. In terms of mechanical machining, XPS has been used in innovative ways. Small XPS penetration depths, have been exploited to correlate machining chip colour with cutting temperature [109]. FeO, Fe_3O_4 and Fe_2O_3 on the surface of dry-machined H13 steel were identified XPS showed that colour can effectively be used to understand cutting temperature and expected metallurgical transformations. Similarly, XPS has been used to study the oxide layers produced on iron by electrochemical machining [110], with the modified layers able to be compared from various current densities. The small depth of analysis associated with XPS is a benefit as well as a drawback. The sample must be cleaned extremely well as contamination will be detected. In the case of machined layers, it is essential that the area of interest is within this depth. In addition, XPS incurs a relatively long data collection time compared to other surface analysis techniques [111]. Another, somewhat more advanced technique for compositional and microstructural analysis is atom probe tomography (APT). APT is capable of three-dimensional nanoscale chemical mapping of individual atoms, and the technique is destructive, consuming the specimen during testing. The process works by the application of a strong electric field to a small, needle-shaped specimen, causing the atoms at the tip to evaporate [112]. Data analysis combines time-of-flight mass spectrometry with nanoscale 3D spatial coordinates [113]. This technique has been applied to white layers formed by hard turning of a Cr-containing high carbon steel, whereby the movement of carbon in mechanically and thermally was determined and for example segregation of carbon at grain boundaries was detected [114]. Despite the excellent resolution of APT and the unique ability to perform three-dimensional compositional analysis, the drawbacks of the process should also be considered. Preparation of a large number of samples is difficult, expensive and time consuming, and specimen fracture is common in the sample, given mechanical stresses may approach the cohesive strength of the material [112]. In addition, the maximum volume which can be analyzed is limited and on the order of 10^6 nm^3.

3. Mechanisms governing the mechanical effect upon surface integrity

The mechanical effect in machining refers to the mechanical load to which the workpiece is subjected to remove material, deforming the machined surface and superficial layer, thereby causing surface damage [115]. This mainly occurs in conventional machining carried out under particular conditions (e.g. low cutting speed, abundant coolant application) that yield relatively low cutting temperatures, therefore it is considered that mechanical loads are mainly responsible for both geometrical (e.g. crack and pluck) and metallurgical (e.g. grain deformation) damage occurring on the workpiece superficial layer.

3.1. Mechanical effects in conventional machining

In conventional metal machining, high strains are induced on the workpiece due to the contact between cutting tool and the material, creating three different deformation zones, shown in Fig. 6 [116,117]. The shear strain has highest values in the primary shear zone (Zone I – Fig. 6), which leads to severe dislocation cell structures that are greatly elongated, shown in Fig. 6 (b). This high strain deformation in the primary zone, combined with the friction/ploughing effect in the tertiary zone (Zone III – Fig. 6), leads to a (severe) plastically deformed layer, shown in Fig. 6 (c)–(f), in which a change from highly deformed microstructure to undeformed microstructure can be observed.

3.1.1. Plastic deformation

Severe workpiece plastic deformation near the free-surface caused by mechanical machining, mainly leads to two microstructural alterations: deformed grains and grain refinement. The extent of plastic deformation is correlated with cutting conditions such as high tool wear, cutting speed and feed rate as well as coolant application [118]. At less aggressive machining conditions (e.g. low uncut chip thickness and reduced level of tool wear), surface damage is mainly represented by deformed grains, also known as swept grains or material drag. This can easily occur when machining difficult-to-cut materials such as nickel and titanium based superalloys that have high mechanical properties (i.e. high yield and ultimate tensile strength, hardness), which yield a high cutting force and tool wear rate [119], hence deforming the surface and superficial layer [78], shown in Fig. 7 (a) and (b). In such cases, grain deformation is mainly induced by the glide of dislocations within the

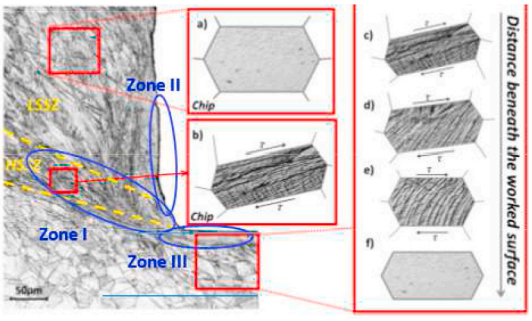

Fig. 6. The deformation mechanisms in chip and machined surface in orthogonal cutting [116].

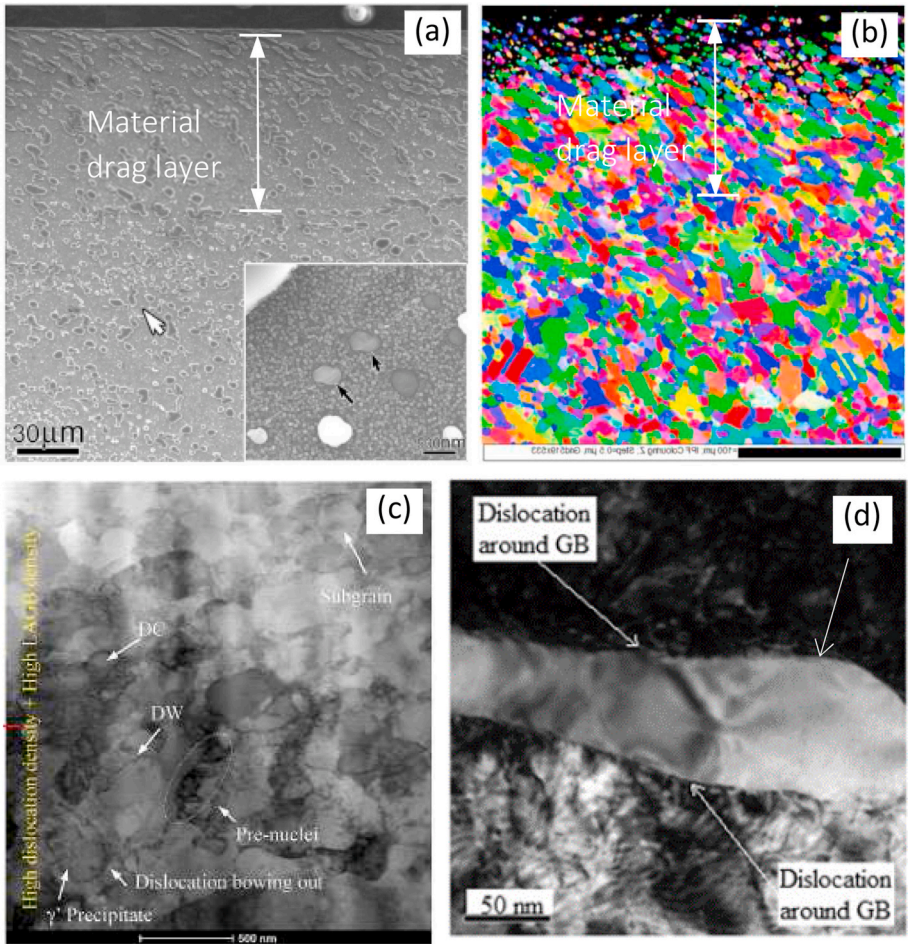

Fig. 7. Examples of features of superficial layers from machined nickel-based superalloy: (a) SEM and (b) EBSD observation of plastic deformed grains [78], (c) dislocations activities and (d) pile-ups around the grain boundary in the plastic deformation layer [65].

crystals, while the grain boundary stops dislocation accumulation due to its strengthening effect [65,120], shown in Fig. 7 (c) and (d). Hence, high dislocation densities within the grains in combination with dislocation pile-up at the grain boundaries, leads not only to plastic deformation of the grains, but also to a work hardening effect beneath the machined surface. In this scenario, the material drag direction represents the paths of dislocations of grain deformation occurring in the direction of cutting tool movement relative to the workpiece. This is also shown in the EBSD inverse pole figure colour map (Fig. 8), where clear grain deformation containing high dislocation densities can be observed, aligning with the cutting direction [75].

3.1.2. *Mechanically induced grain refinement*

When machining under aggressive cutting conditions, (e.g. large uncut chip thickness and tool wear), the resultant high mechanical load leads to severe workpiece plastic deformation with the possibility of grain refinement at the machined surface layer. This machining-induced grain refinement layer is also called the white layer as it appears white after etching, shown in Fig. 9. The white layer usually appears as a hard and brittle layer, which can facilitate crack initiation and propagation at the workpiece surface, which, in many cases, limits the fatigue strength of the end product [121]. Guo et al. (2010) [122] concluded that white layers could reduce the fatigue life by as much as eight times compared

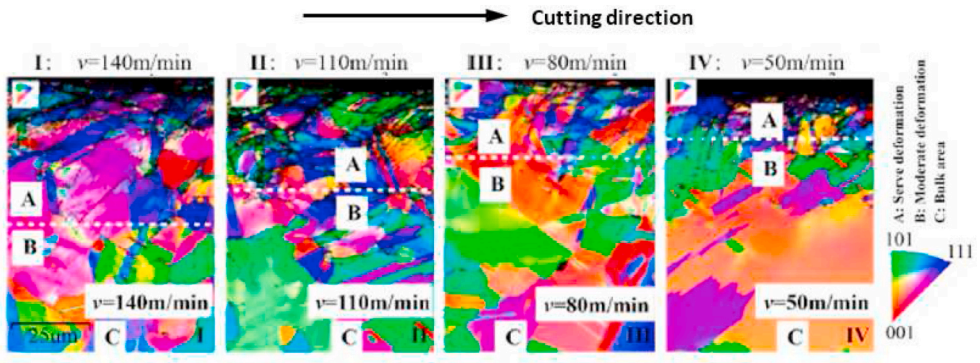

Fig. 8. EBSD-Inverse pole figure colour map showing plastic deformation areas in the superficial layer of orthogonal cut Inconel 718 [75]. (For interpretation of the references to colour in this figure legend, the reader is referred to the Web version of this article.)

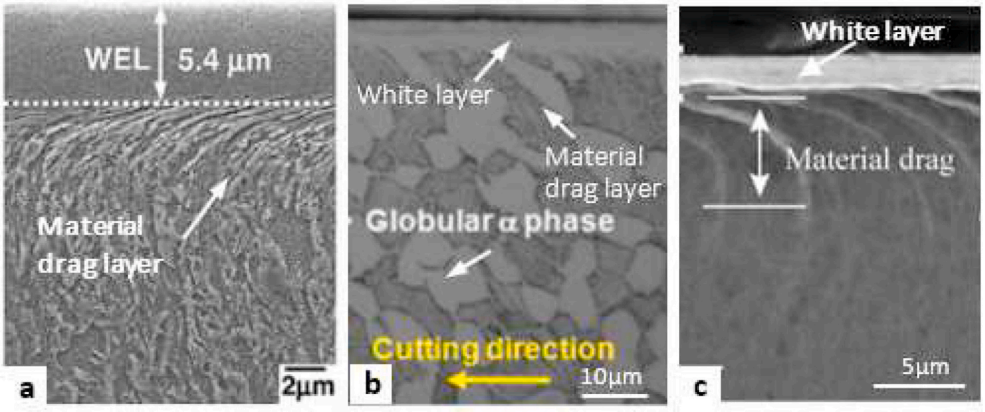

Fig. 9. White layer in mechanically machined (a) carbon steel [123], (b) titanium-based superalloy [124], and (c) nickel-base superalloy [125].

to surfaces free from white layers resulting after machining of AISI 52100 steel. Consequently, white layers require removal or minimisation when manufacturing safety-critical components for applications where high surface integrity is required (e.g. aerospace industry).

White layers can occur under both high and low cutting temperature modes. More specifically, when this is generated by high mechanical loading during low temperature cutting, it is also called the mechanically-induced white layer (M-WL) [70], where grain refinement is mainly due to the severe plastic deformation while there is no/limited thermal effect. However, the white layer can also occur under both high mechanical loading and cutting temperatures, whereby dynamic recrystallization occurs, namely the thermal induced white layer (T-WL). While this section is mainly focused on the mechanical effect of machining, the T-WL will be discussed in Section 6 – where combined effects are explored.

Although different white layer formation mechanisms have been elucidated when machining various materials with their specific characteristics, in general, it is agreed that grain refinement occurs in both M-WL and T-WL, leading to grains of tens or hundreds of nanometres in size. The M-WL, resulting from severe plastic deformation at relatively low temperatures, e.g. well below the parent phase transformation temperature, contains only the parent phases with no new phases. In this case, the parent grains are deformed and fragmented by the high strain induced by the mechanical load, resulting in breakage of the original grains or an elongated sub-grain structure where re-orientation occurs along the shear direction (Fig. 10 (b)) by the dynamic recovery mechanism [114]. Since this occurs at relatively low cutting temperature conditions (e.g. below the phase transformation temperature), the original phases remain unchanged in M-WL (e.g. θ-carbides in AISI 52100 steel, Fig. 10 (c)). It is also worth noting that, as a high mechanical load is imposed on the workpiece material, the M-WL is always accompanied by a layer of material drag/deformed grains beneath the layer due to the gradient of the plastic strain, shown in Fig. 9. In this case, the deformed grains can be considered as a pre-generation of the white layer where the induced dislocation is not dense enough to break the grains.

Nevertheless, the formation of this ultrafine grain structure is not only dependent on the cutting strain but also the strain rate promoted by cutting speed. A range of ultrafine grains and nanoscale dislocation structures in the mechanically induced white layer formed under various strains (1–15) and strain rates (10–100,000 s^{-1} corresponding to 1–5 m/s cutting speed) and temperatures of up to 0.4 Tm (melting point) can be seen in Fig. 11, an example from orthogonal cutting of high purity copper (99.999%) [126]. Three different mechanisms have been revealed: (i) at low strain and strain rate the microstructure mainly consists of subgrains with lower misorientation and diffuse grain boundaries formed from the elongation of original grains due to the shear deformation of the grains, which also yields a work hardening effect; (ii) at low strain but large strain rate mechanical twinning occurs with similar work hardening effect to the deformed grains due to the larger number of crystal defects; (iii) at a high level of both strain and strain rate dynamic recrystallization occurs and leads to an equiaxed morphology accompanied by annealing twinning and larger misorientations. It is worth noting that in scenario (iii), as a high deformation temperature would be induced in the workpiece, the recrystallization is mainly driven by the intrinsic deformation-induced heating in conjunction with the added strain, and hence the white layer formed in this case is considered as a temperature induced white layer.

The mechanically induced white layer, M-WL, in general can be attributed to the increase of strain (corresponding to the machining shear deformation) and strain rate (corresponding to the cutting speed and feed rate). In this case, the microstructure is mainly characterised by a broken-down and elongated sub-structure [127], through the mechanism of dynamic recovery. This grain refinement phenomenon can be also described through the model proposed by Ding et al. [78] (Fig. 12), which summarises the microstructural evolution of the white layer in five steps: (a) the machining mechanical load induces some dislocations

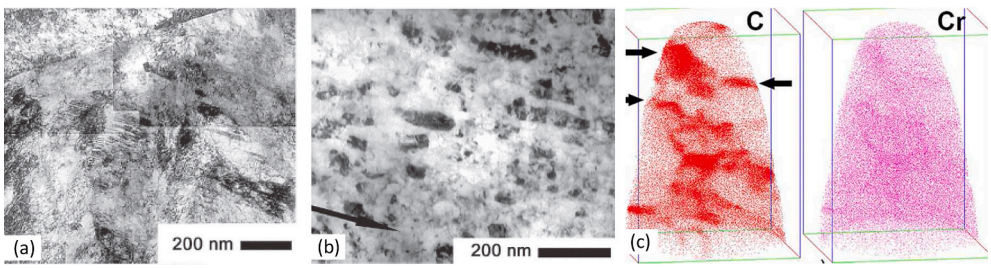

Fig. 10. (a) Crystal structure of bulk material, (b) elongated sub-grain structure and (c) 3D atom maps of C and Cr distribution in the M-WL of AISI 52100 steel by hard turning [114].

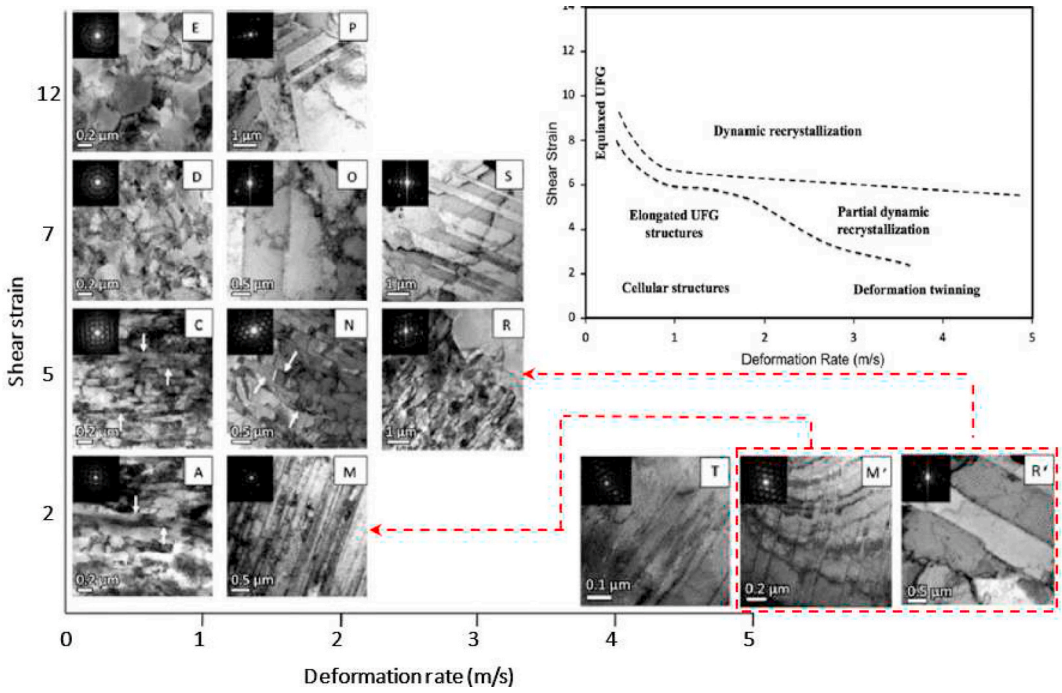

Fig. 11. TEM images of the microstructure of copper at select values of strain (0–12) and deformation rate (cutting speed: 0–5 m/s) from plane strain machining; R′ and M′ correspond to the same deformation conditions as R and M, respectively [126].

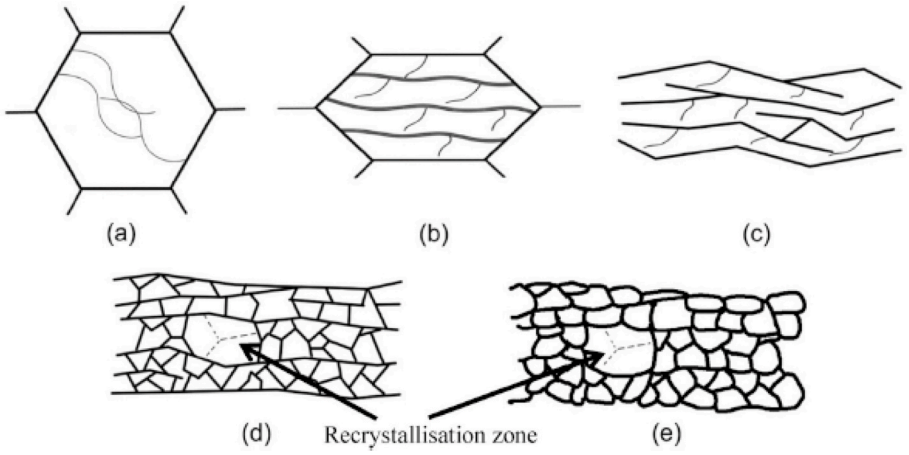

Fig. 12. Schematic illustration of microstructural evolution of the white layer induced by conventional machining [78].

into the original grains; (b) original grains are deformed or elongated along the shear direction through slip bands or dislocation and (c) cause re-orientation within the original grains; (d) the original grains are broken/partition into elongated cells and subgrains through the slip bands or dislocation walls and form the M-WL; (e) if the machining condition is aggressive enough to generate a high deformation temperature, a thermally assisted deformation mechanism may occur and cause dynamic recrystallization, i.e. a T-WL.

3.1.3. Work hardening

Due to the mechanical load induced upon the workpiece during machining, a work hardening effect can result, changing the hardness and residual stress within the superficial layer. This typically occurs when machining high strength materials, e.g. hardened steels and superalloys, with which high cutting forces are yielded. In general, a significant increase in hardness occurs in the superficial layer, which could be related to the plastic deformation of the grains therein allowing the accumulation of atomic dislocations. In sufficient density, these serve to drastically increase local hardness. On the other hand, grain refinement, where nanocrystalline structures appear on the surficial layer can also lead to a hardening effect due to the increase in grain boundaries, i.e. the Hall–Petch effect. Fig. 13 shows the increased hardness on the superficial layer of machined Inconel 718, which is mainly induced by grain refinement and substructures such as dislocations and mechanical twining [67].

As the cutting tool slides upon the workpiece during cutting, mechanically-induced subsurface plastic deformation also leads to compressive residual stress in the machined workpiece. Fig. 13 (b) shows a residual stress profile of milled Inconel 718, where increased compressive stresses are found on the superficial layer, reaching a peak value at around 20 μm depth and diminishing beyond 120 μm [128]. Moreover, the mechanical energy exerted on the surface during the cutting process is high enough to produce a great number of dislocations. The interaction due to the strain fields around the generated

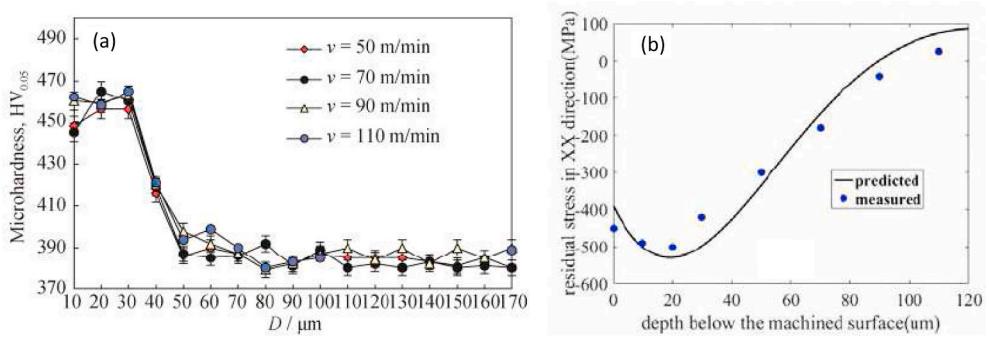

Fig. 13. Examples of work hardening on the conventional machining of Inconel 718 results in (a) surface hardening [67] and (b) compressive residual stress in the superficial layer [128].

dislocations leads to "strain hardening" in the material (i.e. proportional to $\sqrt{\rho}$, where ρ is the dislocation density) upon further deformation, which results in an increase in the material yield strength [129]. Plastic deformation also leads to changes in crystal lattice orientations within each grain. Hence, by calculating the orientation differences between the indexed pixels of the acquired EBSD map, e.g. kernel average misorientation (KAM) map (Fig. 14 (a)), and the average intragrain misorientation (AMIS, Fig. 14 (b)), the extent of plastic deformation/-strain can also be quantitatively evaluated [77]. These compressive residual stresses, along with the increase in hardness, can be beneficial to fatigue performance of the machined components. However, although the mechanical effect can induce compressive stress in the superficial layer, in many conditions it may also be compensated by the thermally induced tensile stress, hence exhibiting a varying residual stress distribution along the surface layer. This will be discussed in Section 6 (combined thermo-mechanical effect).

Nevertheless, although the severe plastic deformed layer is undesirable for most safety critical applications due to the deterioration of fatigue performance, it can also be beneficial when machining low to moderate strength metals and alloys, e.g. carburized bearing steel [130] and aluminium alloys [131] for specific applications such as bearings, gears and shafts. That is, those severe plastic deformed layer formed under the machining conditions that do not lead to phase transformation, tearing-cracking or tensile residual stresses would still be considered beneficial. This is because the ultrafine grain structure induced by high mechanical machining (e.g. hard turning) usually contains a high dislocation density (Fig. 15 (a)), which can lead to higher strength, hardness and wear-resistance than their coarse grained counterparts [132]. This machining-induced strengthening effect is also comparable to other multiple-stage deformation processing operations such as equal channel angular processing, high pressure torsion and cold rolling (Fig. 15 (b)), while it offers economic benefits as only one pass is needed to create significant strains [133].

3.1.4. Geometrical defects

In addition to the microstructural alterations, there are also other manifestations of surface defects induced by high mechanical loads from machining, which are mainly of geometrical nature, such as micro-cracking [134], plucking [84], surface tearing [77,135], material redeposition [136,137] and debris [138,139], summarised in Fig. 16. In general, these defects appear when unsuitable cutting conditions are applied, e.g. large chip thickness and tool wear. Specifically, surface tearing and grooves can be attributed to the dragging of particles that are generated during machining (e.g. hard precipitate from the workpiece material or chipping from the cutting edge/insert) [134,135]. Redeposition and debris are caused by the adhesion of the workpiece or tool material to the machined surface under high contact stress. Smearing is produced by severe plastic deformation of the surface caused by the flank face of the cutting tool, hence this may mostly happen in severe tool wear conditions [18]. Plucking occurs due to the removal/pull out of small and hard particles/grains from the surface [140]. Cracking occurs mainly in the machining of brittle and semi-brittle alloys, e.g. γTiAl, due to their low ductility and high crack growth rates. However, when machining ductile alloys in which hard phases are present, cracks can also occur, mainly in the vicinity of hard

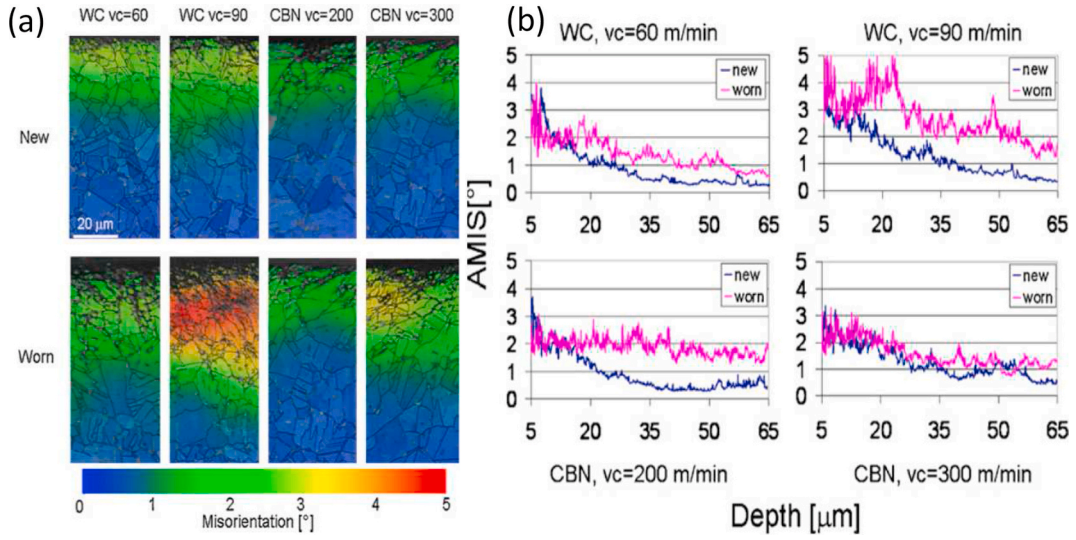

Fig. 14. (a) Strain contouring maps defined by crystal misorientation and (b) average misorientation profiles of finish turned Inconel 718 [77].

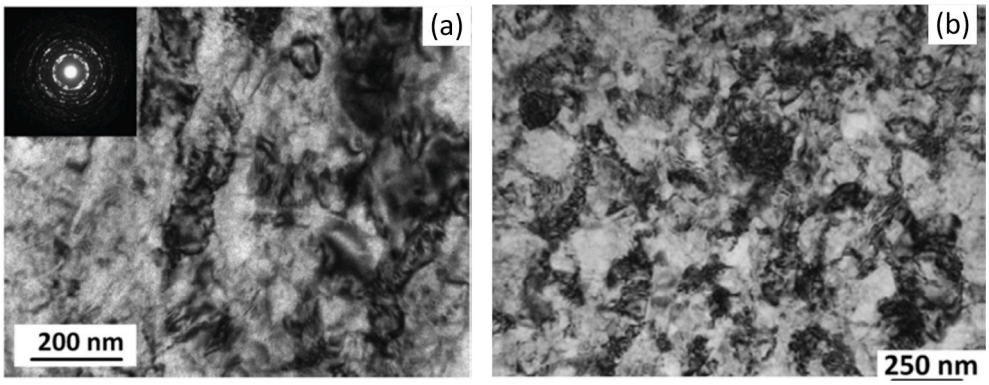

Fig. 15. TEM images of grain refinement of CP Ti produced by (a) orthogonal cutting [132] and (b) multi-pass cold rolling [133].

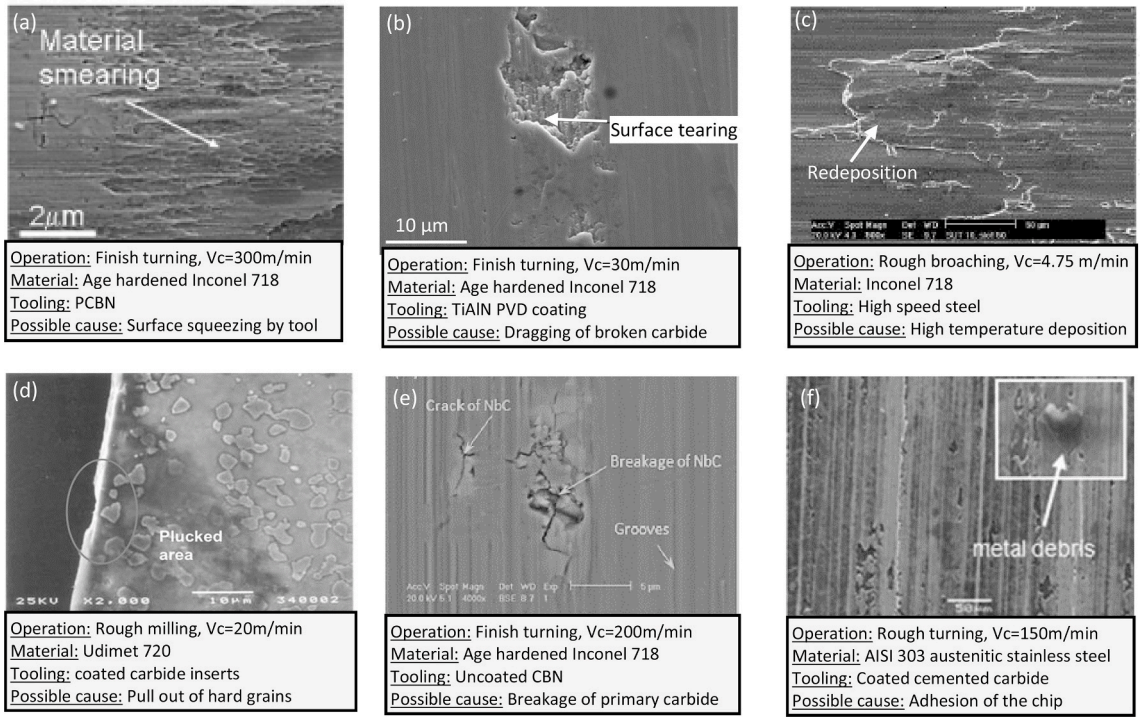

Fig. 16. Examples of geometrical anomalies in conventional machining of metals: (a) material smearing [77], (b) surface tearing [135], (c) redeposition [137], (d) pluck [141], (e) crack [134], (f) metal debris [138].

carbides present in the work material, due to the mismatch of the material properties between the matrix and carbides [77]. These surface defects are, in general, caused by the high mechanical and thermal loads that are induced by unsuitable cutting parameters. Since such defects can present a high risk in safety critical applications, it is therefore essential to optimise the cutting conditions to reduce the severity of these surface defects, although it may not be possible to completely avoid them.

3.2. Abrasive waterjet cutting

Abrasive waterjet machining (AWJ) is a mechanical material removal method whereby the workpiece material is eroded by a mixture of abrasives and a high velocity waterjet stream under high pressure (up to 700 MPa [142]). Due to the high hardness and sharpness of applied abrasive particles (e.g. garnet), which are entrained by a high energy density waterjet, small chips are removed from the substrate material and flushed away by the waterjet (Fig. 17 (a)) [143]. This process yields low average cutting forces and temperatures, and hence leads to reduced mechanical and negligible thermal damage on the workpiece material compared to conventional mechanical machining [144]. In general, two different material removal mechanisms, ductile or brittle removal, depending on workpiece material properties, can occur in AWJ machining, leading to different surface damage modes.

When machining ductile workpieces, the material removal mechanism is dominated by the plastic removal mode. Due to the high speed impact of the abrasive particles (up to 700 m/s [145]), the workpiece surface usually suffers mechanical damage such as scratching and chipping [146], embedment of fractured abrasives [60], striations [147], as well as high plastic deformations in very small areas (where the individual grains impacted the surface) which may even refine the grains [148]. This damage is distributed on the near surface layer, i.e. by scratching and abrasive embedment, as the particles slip on the surface while imparting their kinetic energy to the work and, sometime, embedding into the surface or subsurface layer, i.e. causing plastic deformation due to the high energy impinging of the abrasive particles. These scratches and abrasive embedding phenomena, in general, can act as stress concentrators on the surface and initiate cracks which can result

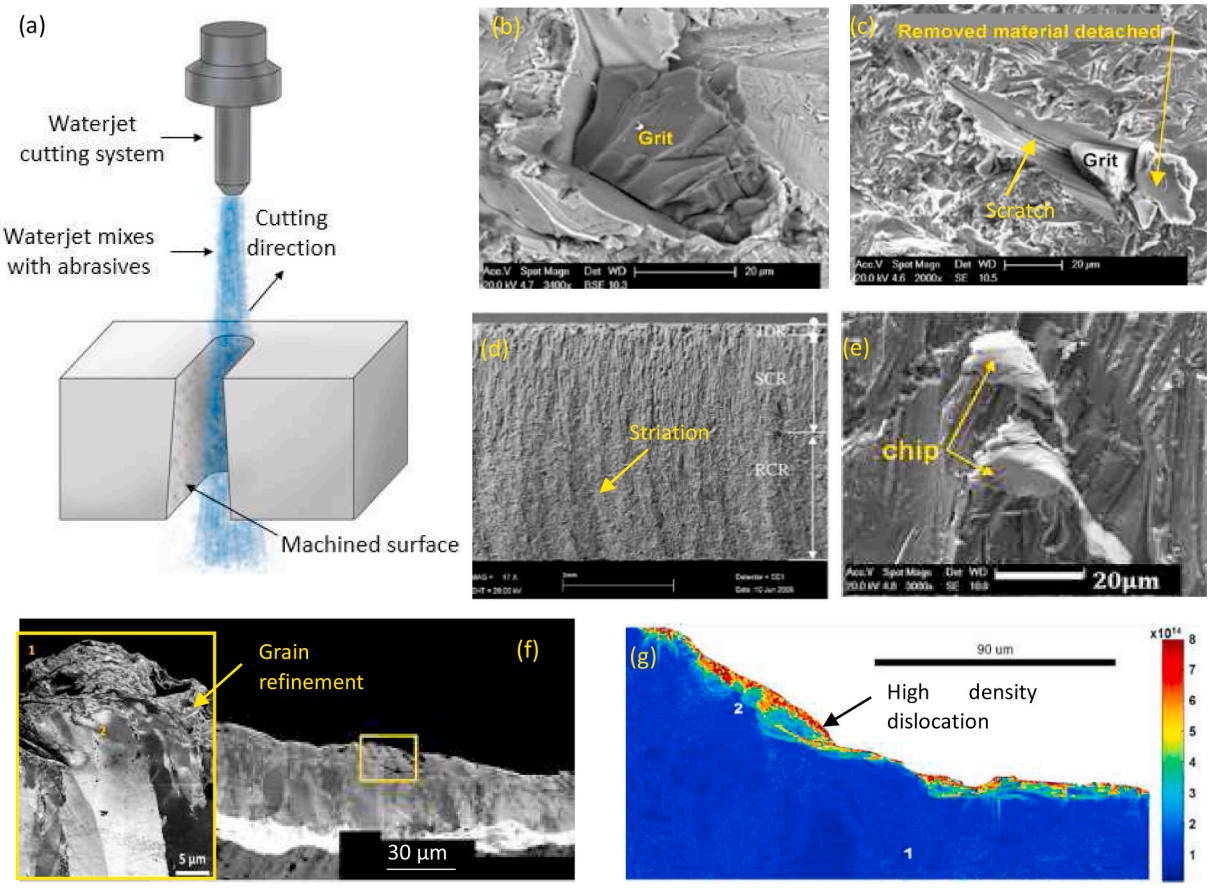

Fig. 17. (a) Schematic of AWJM process [150] and some examples of surface damages generated by the process: (b) abrasive embedment (NiTi) [60], (c) scratch (NiTi) [60], (d) striation marks (Ti64) [147], (e) chipping (NiTi) [146] (f) grain refinement and (g) zones with high density dislocations measured by an EBSD dislocation density map (microcrystalline nickel) [148].

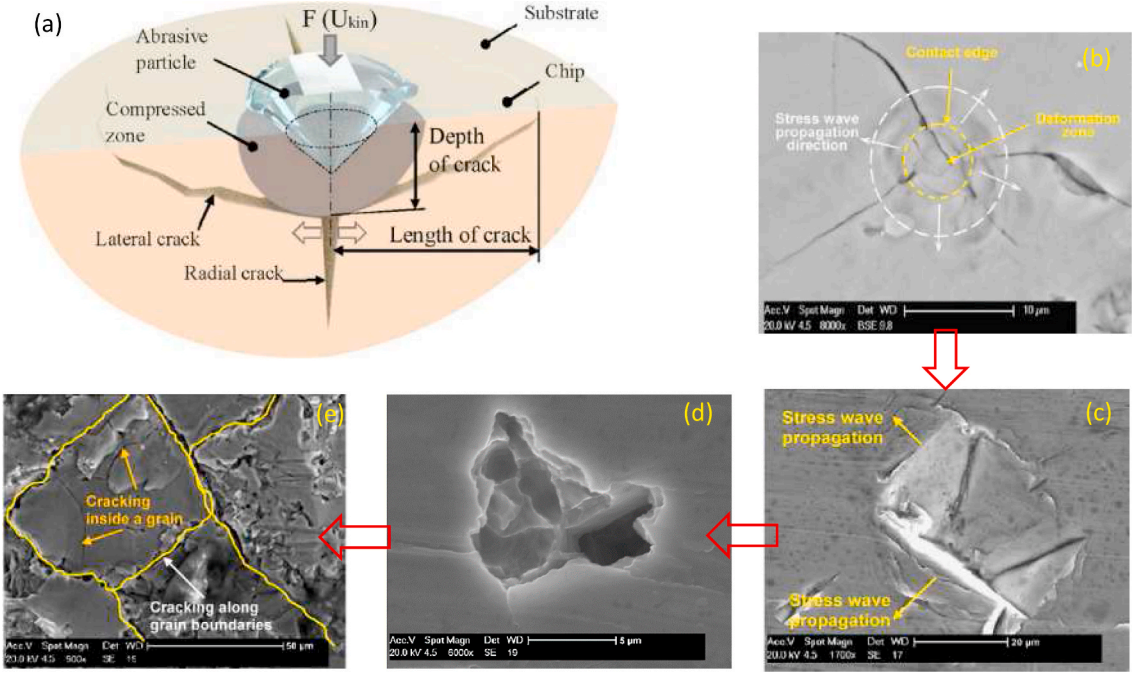

Fig. 18. (a) Brittle erosion mechanism [151] in waterjet machining, and surface damage generation: (b) crack initiation, (c) stress wave propagation, (d) micropits generation and (e) intergranular fracture in γ-TiAl [152].

in deterioration of fatigue life by as much as 30% [149]. Hence, a secondary process (e.g. surface modification or finishing procedure) is required to remove these defects [150]. Fig. 17 (f) and (g) show the high strain deformation layer inside the microstructure (microcrystalline nickel workpiece) near the machined surface, within which grain refinement can be observed on the top surface due to dislocation accommodation, resulting from the effect of abrasive grit impingement of the surface. This grain refinement induced by high compressive deformation, on the other hand, has a work hardening effect with large plastic strains on the superficial layer and can enhance surface properties, beneficially effecting hardness, wear resistance and even fatigue life as no tensile residual stress is produced.

When (abrasive) waterjet machining brittle metals (e.g. γ-TiAl), the workpiece is removed/eroded mainly by a repetitive fracturing mechanism instead of plastic deformation due to the hammer effect of the accelerated abrasives or water droplets on the workpiece, shown in Fig. 18. Specifically, the abrasive impact generates compressive stress which initiates a radial and lateral crack, propagating downwards and away from the base of the deformed area when exceeding the fracture threshold [151]. While the lateral crack determines chip formation (Fig. 18 (a)), the radial crack degrades the surface integrity, whereby severe cavity and crack damage would be left on the machined surface. This crack damage is usually developed at highly tensile stressed zones situated at grain boundaries of crystalline materials, interfaces between the matrix and inclusions of multiphase materials or pre-existing interfaces/cracks/pits [151]. An example can be explained from Kong's model of waterjet machining of γ-TiAl wherein four steps are proposed: (i) plastic deformation and crack initiation; (ii) stress wave propagation; (iii) micropits due to joining of crack lines; (iv) intergranular cracking/fracture, triple splitting and interlamellar/translamellar fracture [152].

4. Mechanisms governing the thermal effect upon surface integrity

Alongside mechanical machining (e.g. conventional machining), thermal machining processes are also widely used for manufacturing components for a wide range of industries. In this case, generally, the material is removed by melting or vaporisation by applying a heat source, with negligible/limited mechanical force applied in the solid state. Different heat sources are applied, such as plasma (electrical discharge machining (EDM) and plasma beam machining (PBM)), photons (laser beam machining, LBM) and electrons (electron beam machining, EBM). However, due to high thermal loads, many secondary phenomena can result from machining. These can include the formation of heat-affected zones, recast layers, and micro-cracking as well as thermal softening effects, which can lead to a reduction in fatigue life of the machined component.

4.1. Laser beam machining

4.1.1. Physical process of continuous wave and pulsed laser machining

Laser processing of solids is a direct, local, and material-selective process, which has been employed for machining of difficult-to-machine, hard and brittle materials. With the aid of lasers, it is possible to remove material without mechanical damage, while having no tool wear and excellent dimensional accuracy. In metals, photon energy is absorbed by free electrons in a thin superficial layer, typically ≈10 nm, and leads to melting, vaporisation, and ionisation of the absorbing media [153,154]. Depending on the ratio between pulse width and characteristic lattice heating time, the lattice will experience different levels of heat-related effects, exemplified in Fig. 19 (a)–(b). For most metals, lattice heating time is on the order of 1–100 ps [155], representing a border between thermal and non-thermal removal

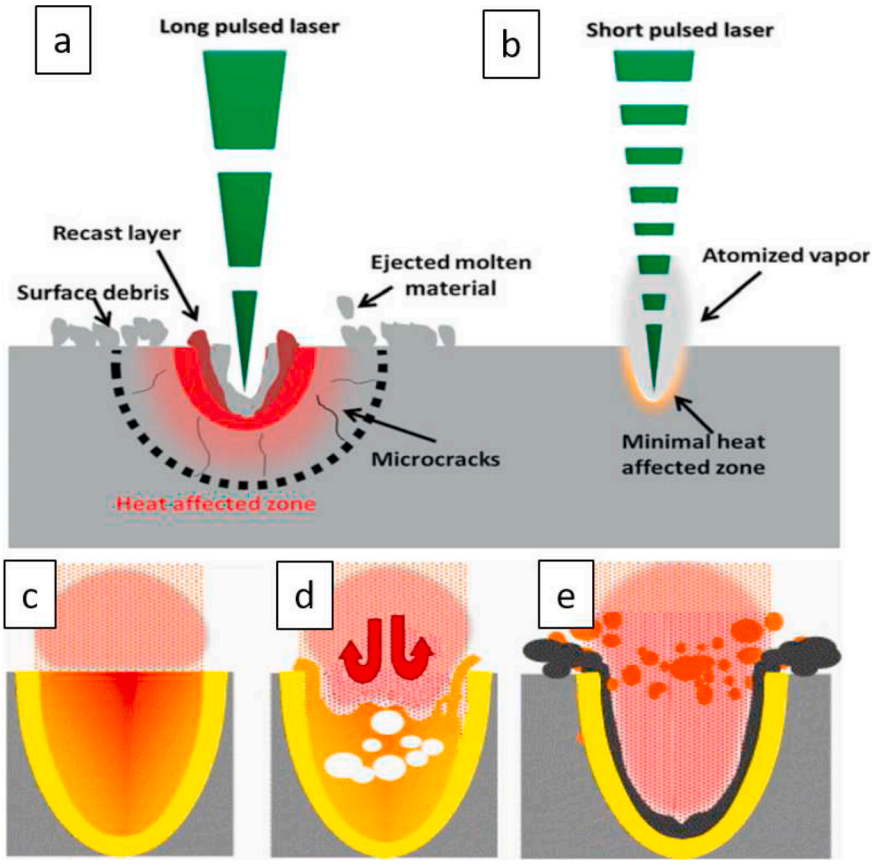

Fig. 19. (a) Long (nanosecond, microsecond and longer pulses) and (b) ultrashort (picosecond, femtosecond and shorter) pulse laser ablation. Nanosecond and longer pulses do not prevent heat propagation and thermal effects, leading to heat affected zone and collateral workpiece material damage [156]. Typical removal mechanisms via long pulse ablation (adapted from Ref. [157]): (c) melting and vaporisation, (d) melt displacement, caused by recoil pressure, and (e) melt ejection in pulsed laser machining.

mechanisms.

In long pulse ablation (nanosecond and longer) and continuous wave cutting, heat is absorbed by electrons and followed by fast energy transfer to the lattice by collisions, diffusion, or electron-phonon coupling. Laser irradiation first heats localised volumes to the melting point and then to vaporisation. During long pulses, absorbed energy propagates into the workpiece by heat conduction. Presence of heat-affected zones, melted zones, recast layers are typical for long pulse ablation and continuous wave cutting. The depth of heat propagation into the workpiece is determined by the thermal diffusion length $l_{th} = 2\sqrt{D\tau_p}$, where D is thermal diffusivity and τ_p is the lattice heating time [158]. Heat affected zones depend not only on thermal diffusion lengths, but also on the ability of such irradiation to ablate material, i.e. laser fluence, ablation thresholds, heat accumulation effects, and pulse repetition rates. Regarding high power density irradiation, melt pool formation is followed by material vaporisation. Sufficiently long and intensive pulses can be absorbed by vapour, often leading to its ionisation. The vapour/plasma plume creates large recoil pressures, which produces a shock wave that propagates through the material. This often leads to collateral damage and generates compressive residual stresses when pulse energy is sufficient. Recoil pressure induces melt pool flow that extrudes melt from the irradiated area. This forms pits on the crater sides and dictates recast layer shapes. In continuous wave cutting, the recoil pressure repulses the melt and forms a cavity filled with high pressure vapour, called a keyhole. Laser absorptivity within the cavity increases due to increased vapour absorptivity, and multiple reflection of the beam, often referred to Fresnel absorption [159]. Consequently, the cavity deepens, and the vapour pressure blows out the molten wall. Typically, material ejection from the molten area is enhanced by a co-axial gas get.

When it comes to high-quality machining in conductive materials by pulsed laser ablation, ultrashort pulses (ps-fs scale) must be considered. At femtosecond scales, photon energy is absorbed by free electrons and is primarily exchanged among them. Electron-lattice interaction is governed by relatively slow electron-phonon interactions [158]. Heat transfer becomes non-equilibrium with high electron temperatures and the cold lattice, described by two-temperature model [160]. Non-equilibrium temperature distribution leads to significant surface evaporation, preventing heat propagation into the workpiece. Therefore, the process progresses directly from solid to vapour/plasma, allowing precise material processing with the absence of molten material formation at the work and hence recast layers, and heat-affected zone.

The main removal mechanisms for long and short pulse ablations are:

- *Melt expulsion*, or liquid displacement to the crater sides resulting from recoil pressure (Fig. 19 (d)). This is the typical removal mechanism in continuous wave to nanosecond long pulse ablation [157, 158].
- *Spallation*, or material disintegration due to high tensile stresses associated with rapid expansion. Can occur in all thermal ablation regimes. However, its relative contribution to material removal is higher in nanosecond pulse ablation [161].
- *Explosive boiling*, sometimes referred to "*phase explosion*" or "*melt ejection*", is the disintegration of overheated liquid, leading to sub-surface nucleation of vapour bubbles and ejection of the liquid material from the melt pool. This is the typical removal mechanism in short ablation, i.e. nanosecond to picosecond (Fig. 19 (e)) [162].
- *Fragmentation,* or dissociation of the *surface* of supercritical liquid metal into fine droplets due to rapid thermal expansion. Fragmentation suppresses phase explosion mechanism and tends to dominate removal mechanisms with shorter, pico- and femtosecond laser pulses [162].
- *Direct vaporisation,* often with absence of thermal effects. This is the distinguishing mechanism in ultrashort femtosecond pulse ablation (Fig. 19 (b)) [157,158].

Fishburn et al. [157] studied nanosecond ablation with a molecular dynamics simulation and found material removal at low fluences is solely caused by melt displacement. With increased laser fluence, the melt displacement is accompanied by vaporisation, and after a critical laser fluence, explosive boiling dominates the removal mechanism. Nevertheless, the characteristic removal mechanism is a complex interplay between material properties (absorption, characteristic lattice heating time and thermal properties), and incident beam conditions (pulse duration, fluence, and wavelength). The contribution of each is a field for rich and often controversial scientific discussion [161, 163–167].

4.1.2. Typical defects in continuous wave machining, long, and short pulse ablation

Surface integrity of laser machined workpieces, summarised in Fig. 20, is dependent on the dominant material removal mechanism and heat transfer within the material which, in turn, depends on the laser irradiation parameters, and especially on pulse duration (including continuous lasers). *Melt expulsion* results in the recast layer on the sides of workpiece surface and newly generated surface, which leads to an elevation on the sides such as in laser drilling (Fig. 20 (a), (d), (e), (i)). *Explosive boiling (*Fig. 20 (f)) and *fragmentation (*Fig. 20 (g)) eject liquid droplets, which can then solidify and form spatter on the sides of machined features and be ejected from the melt pool in the case of explosive boiling, or its surface in the case of fragmentation. *Vaporisation* is responsible for material *recondensation* [168] and generation of recoil pressure that can induce mechanical damage. Upon solidification, the surface can be covered with a layer of reacted melt with processing gas, typically an *oxide layer* [169]. This becomes especially pronounced when the material includes more reactive ingredients, such as chromium, nickel and niobium in Inconel 718 (Fig. 20 (b)). Solidification of the generated melt pool, recast layer or debris generate high stresses due to thermal shrinkage, often resulting in the formation of micro-cracks (Fig. 20 (d)) [170]. Propagated heat can result in heat-affected zones (Fig. 20 (c), (h)) and phase transformations [171], which is, in general, an unfavourable result of laser machining.

4.1.3. Recast layer and spattering

The microstructure of the ejected material, forming the recast layer and spatter, is typically columnar and perpendicular to the crater curvature due to high solidification rates, however different grain morphologies are also found within recast layers determined by process thermodynamics [175–177]. Mechanical properties of recast layers and spatter can be different from the bulk material, being brittle in nature due to oxidation (formation of other intermetallic regions due to reaction with processing gases), microcracked, and having hardness different from the base material.

Various attempts have been made to reduce recast layers. Low et al. [178] investigated the influence of assistant gas on spatter generated during laser percussion drilling. The authors found that spatter depends on the reactiveness of the assisting gas. Spatter bonding in N_2 and Ar atmospheres is higher than in O_2, and therefore material removal is more difficult. Ejected spatter is thinner when oxygen assisted the drilling, shown in Fig. 21 (a)–(b), and had lower bonding strength, compared to Ar assistance. Zhao and Yu [179] revealed recast layer self-cleaning during picosecond percussion drilling when the energy of the tail of the Gaussian laser beam was sufficient to remove the generated melt from the sides of the crater.

One technique utilized for heat, and therefore recast layer management during ablation is wet ablation. Nisar et al. [180] investigated dry and wet environments (deionised water and propanol), finding that recast layers could not be observed in wet environments. Due to active

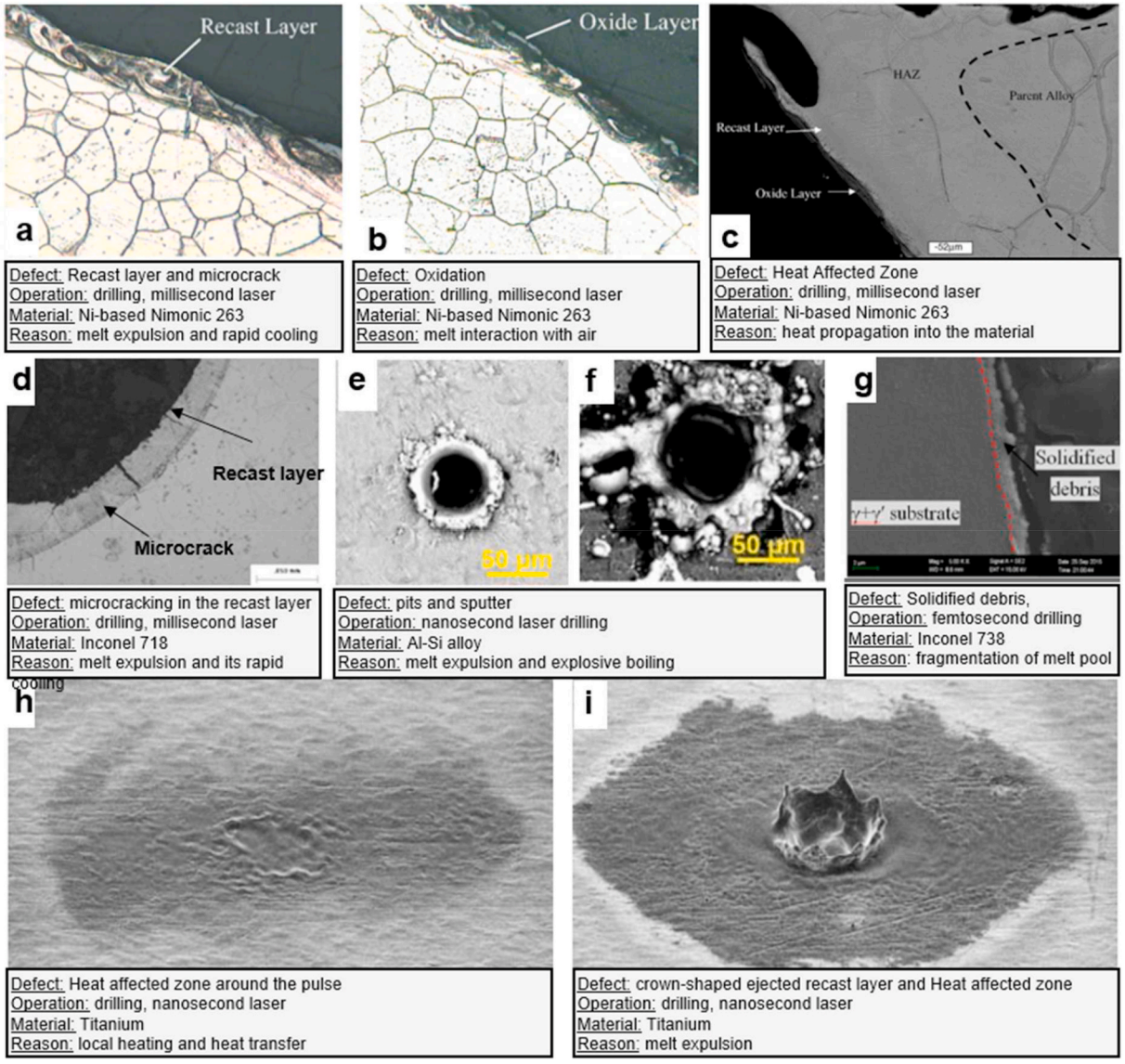

Fig. 20. Surface imperfections in percussion drilling of metals. (a)–(c) recast layer, oxidation and HAZ of nickel superalloy (Nimonic 263) [169]; (d) cracking of the recast layer [170]; (e), (f) recast layer and surface debris on Al–Si alloy after 5(e) and 100 (f) pulses [172]; (g) solidified microdroplets and vapour on the sides of the hole due to fragmentation and recondensation [173]; (h) and (i) HAZ and recast layer after 5 and 50 ns pulses on titanium surface [174].

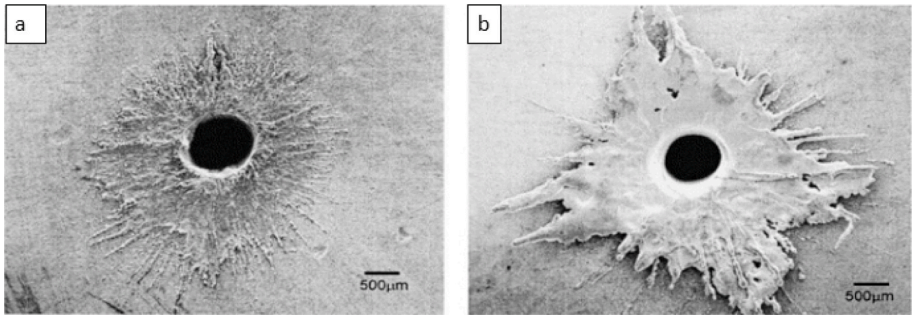

Fig. 21. SEM micrographs showing the typical spatter formation (plan view) of holes drilled with (a) oxygen assist gas and (b) argon assist gas [178].

cooling being more pronounced in wet environments, higher thermal gradients developed in water and propanol lead to fine subsurface microstructures or their complete absence. Kudryashov and co-workers studied pressures developed in underwater ablation, where recoil pressure was 5-times higher, due to dynamic water confinement [181]. High recoil pressure collapse explains high removal rates and spatter-free surfaces in wet ablation. Kang et al. compared removal rates in air and water, finding that ablation performance increased by 700% in water [182]. Kang attributed this increase to thermal desorption of the target (induced by thermal stresses), resulting in material fracture and

crack formation, and spallation dominated the process.

The microstructures of recast layers vary significantly from one case to another. While laser cutting can generate cooling rates of 10^3 K/s, thin recast layers can develop at cooling rates as high as 10^{11} K/s [183]. This wide range of cooling rates, possible during laser drilling, are responsible for the varied grain morphologies, shown in Fig. 22. Variation in cooling rates depends on material properties, ablation regime, most importantly pulse duration, pulse energy and repetition rate. Rapid solidification leads to fine grains (*see* Fig. 22 (b) and (c)) [184]. Shorter pulses increase solidification rates leading to fine columnar cellular, columnar dendritic and equiaxed recast microstructures (*see* Fig. 22 (a) and (b), (d)) [175]. Compositional changes can be also found in recast layers. Garofano et al. revealed the formation of nanoscale Ti-rich carbide precipitates between dendrite arms in Ni-based superalloys [176], which was attributed as a strengthening obstacle. Compared to the base material, the recast layer was softer due to the domination of microstructural influence on the mechanical properties.

4.1.4. Microcracks

At high cooling rates, high tensile stresses can be generated in the metal. Yielding of these stresses to the tensile strength of a given material causes solidified layer cracking. This often combines with the formation of brittle intermetallic layers (in most cases oxides), affecting development of cracks, as shown in Fig. 23. Microcracks are developed in the oxidized layer and propagate further into the recast layer or parent material [185,186].

Thermal management, for instance with assisting gases, can influence cracking behaviour of the recast and oxide layers. Transverse microcracks, perpendicular to the processed surface, are formed within the recast layer due to in-plane thermal gradients upon solidification, while longitudinal cracks are formed at the interface between the recast and oxide layers. These cracks accumulate Griffith energy during propagation and are easier to propagate within recast layers and parent materials, and can cause component failures as indicated by Morar et al. [187]. The authors studied crack formation in laser trepanning drilling of a Nickel-based superalloy and found that pulse energy and pulse duration are the main parameters dictating microcrack and recast layer formation. Their findings revealed formation of both transverse and longitudinal cracks, shown in Fig. 23 (c). Transverse cracks, caused by in-plane thermal gradients during machining, were considered a critical defect since they can penetrate through the recast layer into the workpiece. However, it is important to acknowledge the importance of longitudinal cracks, caused by out-of-plane thermal gradients; these cracks propagate parallel to the surface, and potentially cause delamination of oxide and/or recast layer.

4.1.5. Hardness

Recast layer hardness is usually different from the base material. Recast layer hardness can be higher than the base material, for example Inconel 718 alloy cut with a continuous-wave CO_2 laser, which results in carbide and carbonitride formation on the surface after laser cutting operations, and high cooling rates during solidification of the recast [57]. Surprisingly, recast layer hardness can be also lower than that of the base material, as it was found in the work of Ahmed et al. on microsecond laser drilling of the same alloy [188]. Authors attributed this to low density of γ' and γ'' precipitates at the surface and grain sliding. A possible reason for such a divergence in findings can be ascribed to the difference in formation of the recast: continuous wave melting creates a continuous, dense surficial layer, while pulsed lasers eject material in series. This can lead to higher porosity of the recast and loose solidification of the lamellar layers, eventually decreasing hardness. Overall, the relative change in surface hardness is a complex

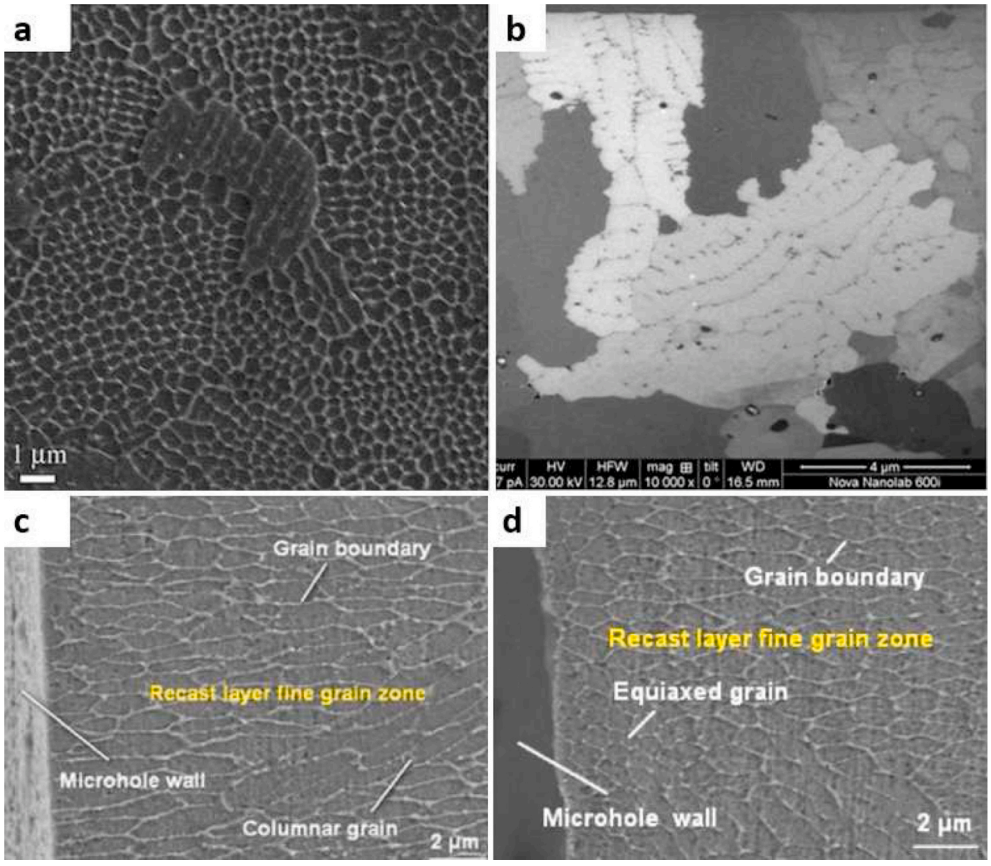

Fig. 22. Different grain morphologies found in the recast layer of laser-drilled Ni-superalloy. (a), cellular morphology of the recast [176]; (b) dendritic microstructure [175]; (c) and (d) fine columnar and equiaxed grains [177].

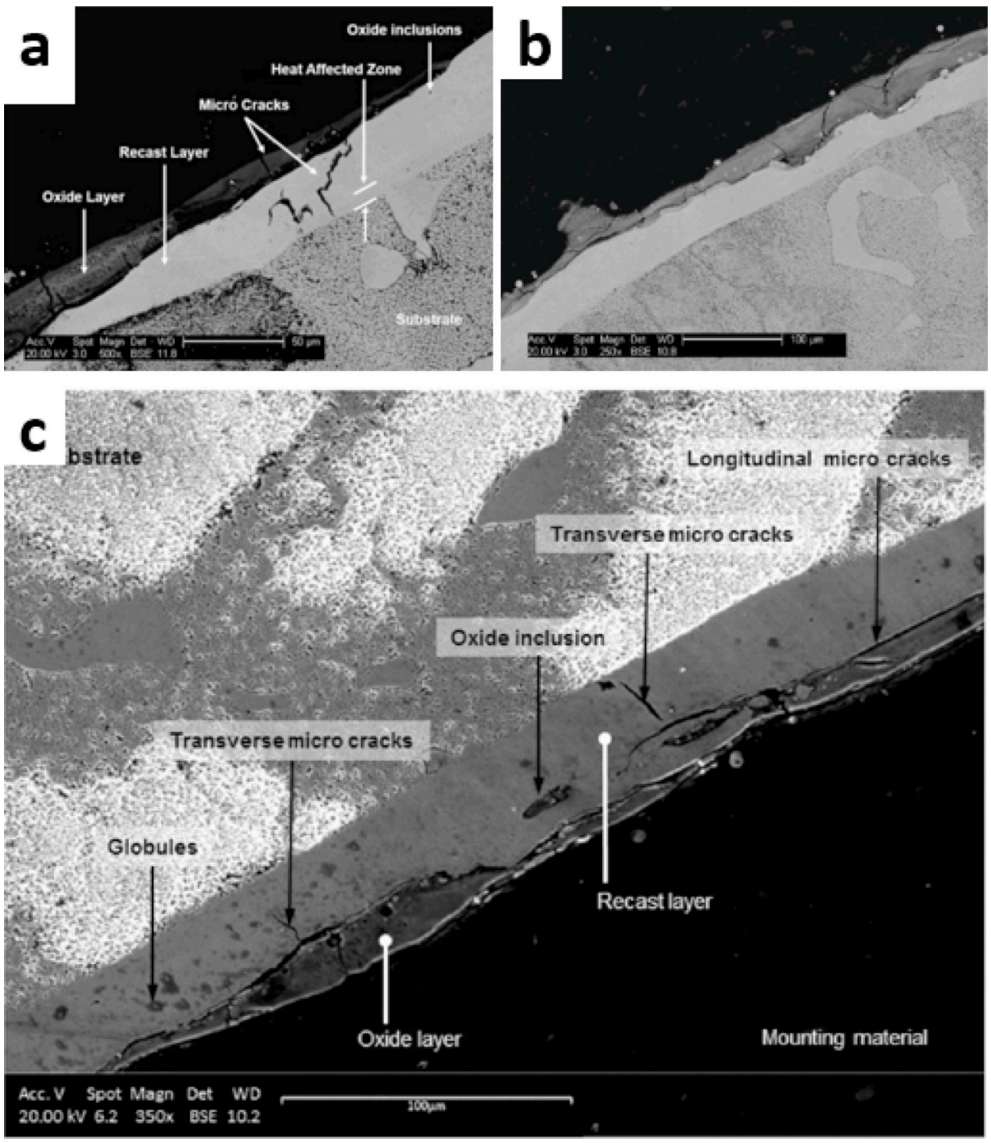

Fig. 23. Surface integrity defects formed during millisecond laser drilling of Ni superalloys. (a) Cracks in the recast layer [185]; (b) transverse cracks in the oxide layer [187]; (c) longitudinal cracks in the oxide layer [187].

interplay among various phenomena, including recast microstructures, ambient environments during laser processing and laser output characteristics, and material parameters.

4.1.6. Residual stress

Several mechanisms can lead to residual stresses upon laser machining. Solidification, accompanied by material cooling and shrinkage, promote tensile stresses in surface and sub-surface layers. Formation of expanding vapour and plasma induces shock waves, which can lead to plastic deformation of the material if pulse energies are sufficient for such deformation [189]. Thermal gradients and material plasticity, metallurgical transformations, and chemical reactions can

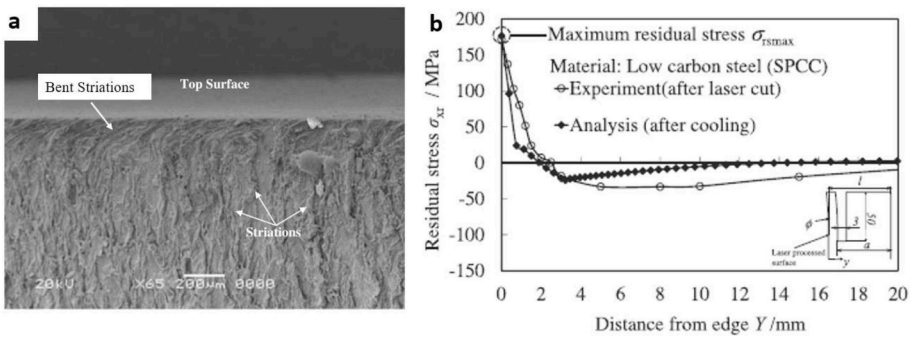

Fig. 24. (a) Kerf surface micrograph of laser trepan drilled Ti–6Al–4V with a CO_2 laser [191]; (b) residual stress distribution [193].

also be responsible for residual stress generation in subsurface areas.

Yilbas et al. studied laser trepan drilling with a high power CO_2 laser [190–192], developing several numerical models combining heat transfer with a viscoplastic model, validating stress fields with XRD measurements. Tensile stresses of 330 MPa were measured at the vicinity of the cut surface in Ti–6Al–4V, more than a third of the material yield strength. Melting and subsequent cooling of the material created striations, shown in Fig. 24, which were bent at the surface due to gas flow. This was attributed to the presence of assisting gas, leading to melt accumulation and solidification in a periodic manner, and should not be confused with mechanically induced strain. This also helped recast layer removal, which was estimated to be 5 μm. Considering XRD penetration depth is *ca.* 10–20 μm from the free surface, developed residual stresses propagate deeper than the recast layer, supported by numerical results. Maeda et al. [193] also found tensile residual stresses (>150 MPa) after laser cutting, resulting from material cooling.

The work of Cha et al. [194] investigated residual stresses formed upon laser ablation of compressor blades with a nanosecond pulsed laser. On the contrary, residual stresses were not different from the bulk material, evaluated through a local misorientation map. This could signify the absence of residual stresses, or rather the inability of the technique to evaluate stress in small regions.

Plasma-induced pressure waves can lead to plastic deformation and generate residual stresses. This phenomenon becomes noticeable only when the pulse energy is sufficient for rapid ionisation, typically in the Joule range in nanosecond scale pulses [189]. These pulses are used to generate favourable compressive residual stresses on workpiece surfaces, which can be enhanced by adding a confining media like water or glass. Laser shock peening is now exploited industrially and is the subject of widespread investigation.

Typically used pulse energies (mJ range) for laser microfabrication do not induce surface damage. This is why little attention is paid to investigation of residual stresses in laser machined workpieces. Nevertheless, generation of compressive residual stresses in-situ during laser machining is an attractive field for research and industrial application.

4.1.7. Ultrashort pulse laser ablation and typical defects

Compared to continuous wave irradiation and long pulse ablation, the physical process changes significantly in the case of ultrashort, femtosecond laser ablation. Ultrashort pulses have negligible thermal diffusion and direct vaporisation is often the prevailing material removal mechanism [164,195]. However, fragmentation and explosive boiling are also reported [162,196,197]. Rapidly removed material has a thin heat-affected zone, causing less material damage. Ablation of steel with different pulse durations, shown in Fig. 25 indicates a transition between pronounced thermal ablation regimes (ns and ps ablation), and clean, defect-free ablation using ultrashort femtosecond laser ablation, due to evaporation, negligible heat conduction, and absence of liquid phase [198]. However, in some cases, heat accumulation in the workpiece exists and affects resultant surface integrity. Hong-qiang Dou et al. [145] studied femtosecond ablation of Al–Mg alloy with relatively low repetition rate (100 Hz), which led to heat accumulation, formation of melt on the surface, and eventually microcracking upon cooling (Fig. 26 (a)).

The choice of appropriate pulse duration is often a trade-off between process efficiency, acceptable level of damage, and equipment cost. Although femtosecond ablation is an attractive technique for clean, defect-free machining, wider application of femtosecond lasers is limited due to the complexity of the equipment able to produce ultrashort pulses with pulse energy sufficient for ablation [199]. While the ablation threshold fluence is independent of pulse duration in the sub-picosecond regime [200], laser intensity is still inversely proportional to pulse duration. This is the limiting factor for machining with shorter pulses in mode-locked lasers. This limitation has been overcome via chirped pulse amplification (CPA), where initial seeding pulse was first stretched by separating the wavelength components of the seeding pulse (typically by diffraction gratings). Different wavelengths are delayed due to different path lengths, amplified separately at safe power densities, and then compressed back. The idea was proposed in 1985 [201], receiving the 2018 Nobel Prize in Physics, which is still the current state-of-the-art technique for short pulse, high power density lasers already available for machining.

Even in femtosecond regimes, melt pool formation due to heat accumulation is possible in low melting point materials, which can result in recast layer cracking, shown in Fig. 26. Some studies on mode-locked femtosecond lasers without further chirped amplification utilize sub-threshold fluence for machining; in this case, ablation relies on incubation effect, i.e. when ablation threshold drops for multi-shot ablation [202] (especially pronounced with high repetition rates [203]). Heat accumulation enables material removal with lower fluences, but leads to noticeable melt pools [204], effectively changing the removal regime to thermal ablation. Interestingly, ultra-high repetition rate lasers can have behaviour different from typical ablation: recently, Kerse et al. [205] used ultra-high repetition rate ablation to exploit ablation cooling phenomena. To increase ablation efficiency and reduce material damage, the authors used ultrafast laser bursts (GHz pulse repetition rate). When the first pulse arrives, it heats up the laser spot vicinity and reduces ablation threshold and the energy necessary for ablation by the succeeding pulse. The work showed that by selecting a suitable pulse frequency, it is possible to utilize thermal energy of previous pulses, thereby suppressing heat propagation into the bulk.

Due to the nature of non-thermal ablation with rapid material evaporation and absence of workpiece thermal damage, femtosecond lasers have an increased interest for microfabrication. For defect-free laser micromachining, femtosecond lasers have become a state-of-the-art technology, and are maturing into a widely available production tool.

4.2. Electrical discharge machining

4.2.1. Principle of material removal and formation of a recast layer

Electrical discharge machining (EDM) is an important process able to machine regardless of workpiece mechanical properties, and hence it is particularly useful for machining hard and tough, electrically conductive materials. EDM comes in the form of sinking EDM, in which an opposite shape of the tool electrode is formed in the workpiece, or less

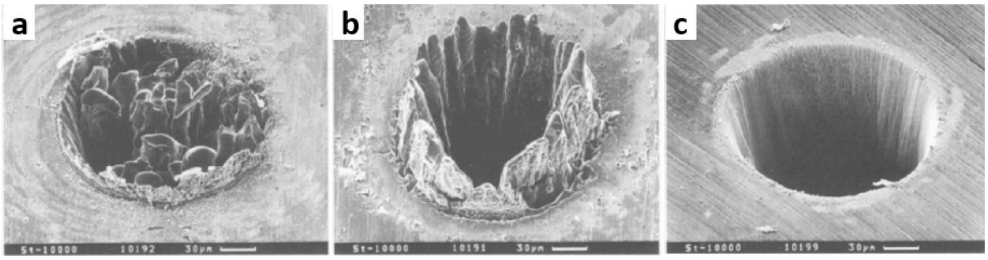

Fig. 25. Micrographs of the laser-drilled holes on steel with long, short and ultrashort pulses. The pulse widths are (a) 3.3 ns, (b) 80 ps, and (c) 200 fs [198].

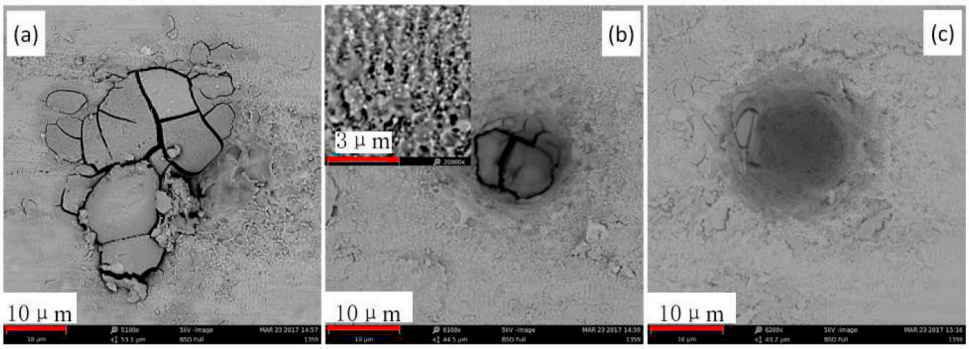

(a) F= 1.5 J/cm^2, N= 20 pulses (b) F= 1.5 J/cm^2, N= 50 pulses (c) F= 2.9 J/cm^2, N= 50 pulses

Fig. 26. Percussion-drilled hole in Al–Mg alloy in air with a femtosecond laser, revealing melt formation and hot cracking [206].

commonly by the 3D movement of a simple electrode as in milling, and wire-EDM, in which a continuously spooling electrically conductive wire slices through the workpiece. In both versions, the material removal process is the same. A schematic of the material removal process, which incurs a recast layer, is shown in Fig. 27.

The exact mechanism of material removal in EDM is complex and still not agreed on. However, in basic terms EDM occurs as a result of a pulsed potential difference between an electrode and a conductive workpiece, which initiates an electrical discharge as a result of dielectric breakdown. In doing so, a plasma is formed with high temperatures and pressures, causing melting and evaporation of material from both electrode surfaces, one being the tool and the other the workpiece. In the case of ceramic materials (which are sufficiently electrically conductive), a porous surface may be produced from which the binder phase is preferentially removed, or in the case of thermal shock sensitive materials, material may be removed by spalling [213]. In addition, decomposition and oxidation have been identified as general removal mechanisms during EDM of ceramics [214]. In the case of metal-ceramic composites there, these mechanisms should also be considered to play a role. During discharge on-time, melt pools are generated on both electrode surfaces. Some researchers [207–209] believe that most material removal takes place at the end of discharge, as boiling of the superheated material is prevented by downward bubble pressure during discharge. However observation of the gap using X-rays has showed that 85% of material removal takes place during discharge duration [210], and direct imaging of EDM debris has showed significant material removal occurs during discharge duration [211]. Pressure build-up in the melt pool during discharge, and overcoming of the binding force is now thought to be one of the mechanisms of material removal in EDM [212]. Not all the material melted by a single discharge is removed by EDM. Yang et al. [215] theorised using a molecular dynamics model that the ratio of ejected to melted material per discharge is in the range of 0.02–0.05. Net material removal in EDM occurs due to large numbers of discrete sparks. Re-solidified material not ejected comprises the recast layer, which tends to have different properties to the parent material, along with a heat affected zone (HAZ) beneath this. The recast layer has characteristics which can negatively impact mechanical properties. Reduced material removal and recast layer on the tool electrode comes about by use of high melting point and high thermal conductivity materials, as well as correct choice of polarity. Such materials include copper, graphite, tungsten and brass.

4.2.2. *Microstructure of the recast layer*

The recast layer on EDM surfaces is made of material melted and solidified at a rate typically faster and in a different compositional environment than when the bulk workpiece was formed with new grain

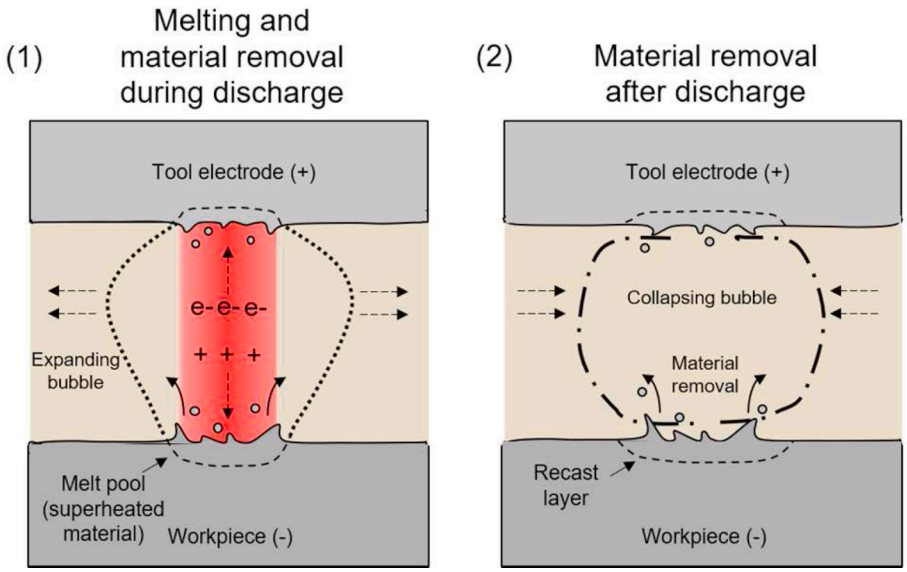

Fig. 27. Schematic of the EDM process showing (1) melting of both workpiece and tool electrode via bombardment by electrons and ions respectively and material removal via boiling, and (2) removal mechanism based on explosion of molten material into discharge gap after rapid drop in pressure. A recast layer forms where molten material is not removed. Several sources have been combined to create this summary of the mechanism ([207–212]).

structures expected as a result. Recast layer microstructures affect mechanical properties, and therefore the properties of the whole part. In metals, the recast layer is known to be typically fine-grained, brittle and hard due to rapid cooling rates [216], with good adherence to the bulk material [217]. The small scale of expected phases and structures in the EDM recast layer has limited its characterisation to high magnification SEM, TEM, or X-ray diffraction. For example, pores of several to tens of microns diameter and observable under SEM and optical microscopy are often expected in EDM recast layers [218,219], examples of which are shown in Fig. 28 (a). Pores can vary in dimensions, depending of processing conditions and workpiece materials, leading to nanoscale pores as reported in silicon [103] In addition, contamination within the recast layer, as well as dislocation dense regions are observable beneath the recast layer, giving evidence of localised stress upon cooling of the recast layer just beneath the interface between it and the bulk.

Wear performance of materials is known to suffer as a result of porosity. The presence of porosity can decrease delamination wear performance of materials, via stress concentrations and collection sites for wear debris, as exemplified in iron [220] as well as bulk SiC/Cu composites [221].

Significant material transformations are expected in EDM recast layers. To date, steels have been the subject of the most significant and detailed research into typical microstructures – nevertheless, generic information which applies to metal can be drawn from these studies. Owing to the uptake of carbon from hydrocarbon dielectric oils, formation of retained austenite is often expected [222], and this structural formation tends to be independent of tool electrode material, since carbon absorption is predominantly from the dielectric (in the case of hydrocarbon dielectrics) which envelopes the EDM process. In the case of de-ionised water, carbon uptake and subsequently retained austenite formation is dependent entirely on using carbon-based electrodes, e.g. graphite. Carbon uptake is also known to be responsible for cementite formation after EDM [217], and the amount of carbon present in the recast layer can be as high as 14 wt% as measured in cross-section via Auger spectroscopy. To demonstrate the complex nature of phase transformations in EDM layers, a simple ferritic steel produced a mixture of cementite, residual austenite, with martensitic needles and an austenitic layer at the interface between the recast and the heat-affected zone [217], demonstrating the impact of cooling from the top surface and into the bulk as well the presence of carbon. Columnar structures are produced at both the top of the recast layer and the bulk gives evidence for two solidification fronts. It has also been noted that the EDM surface can consist of two or three single layer-type recast layers that overlap on one another, formed from the expulsion of molten metal onto an existing recast surface [222]. This is shown in the cross-sectioned sample in Fig. 29 (a). In the non-melted heat-affected zone, modification of the microstructure is typical, and may manifest as tempered martensite in

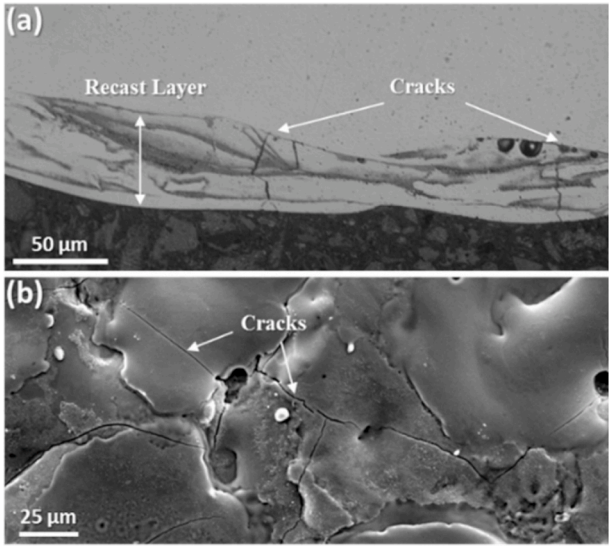

Fig. 29. EDM processed austenitic stainless steels (a) in cross-section showing a large recast layer with cracks penetrating perpendicularly and terminating at the bulk interface and (b) showing surface cracks. Images are unpublished from the authors, and were created using EDM under roughing machining conditions.

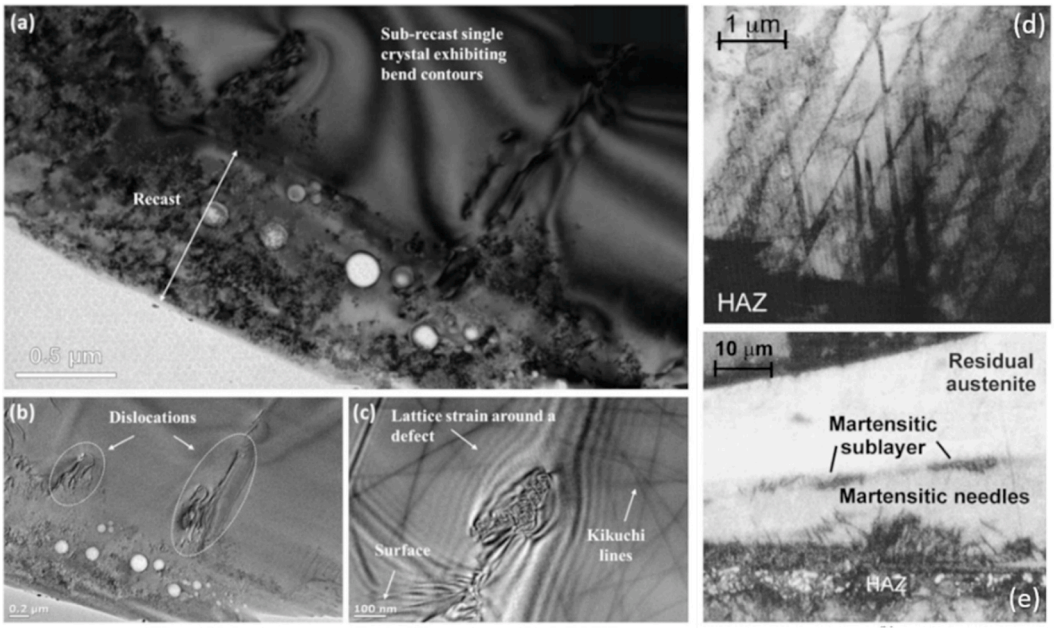

Fig. 28. (a)–(c) Exemplar images of the impact of EDM on a material surface as demonstrated through TEM of EDM machined single crystal silicon, revealing recast layer with porosity of size down to 10s of nm. Dislocations and lattice strain beneath the recast layer show these were regions of maximum stress upon cooling of the recast layer [103]. (d) and (e) show typical structures formed after EDM of an of a ferritic steel, including martensitic needles and retained austenite due to carbon uptake [217].

the case of steel, however this HAZ does not typically display porosity or cracking. In the case of single crystal silicon used to demonstrate the impact of EDM on microstructure, the mechanical stress effect can be clearly seen in the HAZ in the form of dislocations [103] (Fig. 28). Transformations specific to different compositions however should be the subject of further work.

4.2.3. Cracks

Cracks typically extend from the surface to the recast-bulk interface [223], examples of which are shown in Fig. 29 (a). Cracking is a key problem for EDM surfaces since it reduces fatigue life [223–225]. The presence of cracks combined with tensile residual stresses at the surface shortens the two stage process of fatigue failure – crack formation followed by crack propagation [225,226], with a fatigue strength reduction of 15–30% observed in Ti–6Al–4V under aggressive EDM parameters [171]. This is because crack tips themselves can also act as stress concentrators. Degradation was also correlated with the thickness and roughness of the recast layers created by EDM. Therefore, elimination of EDM surface cracks is desirable for improving the service lives of stamping dies and other EDM processed components subject to cyclical loads.

Crack formation can be attributed to the application of tensile stresses in the EDM component. Tensile stresses are generated when the melted material contracts more than the unaffected parent material during cooling. Lee et al. [223] investigated the relationship between EDM parameters and crack formation and made several conclusions. Thicker recast layers and higher induced stresses promote cracking, although crack density remains similar for thick and thin recast layers. The tendency for crack formation is greater for materials with lower thermal conductivities and increases with both pulse on-time and discharge current, although on-time has been observed as the most significant contributor [223,227]. Patel et al.'s study [227] confirmed low fracture toughness and low thermal shock resistance contribute to cracking.

4.2.4. Surface morphology

Typical surface textures of EDM components are characterised by random arrays of craters associated with individual discharge events. These overlapping craters result in a significant level of surface roughness on EDM surfaces, dependent on machining parameters. Excessive surface roughness of EDM processed materials often causes problems, particularly for moulds and dies, where surface defects are replicated to the subsequently manufactured parts [228]. For these reasons, surface finishing, as well as complete recast removal of such components is often desirable.

Recast layer thickness depends on the dielectric type, with some evidence that kerosene yields thinner recast layers than deionised water, water-in-oil emulsion and a water solution, with Ni-superalloy as an example [229]. It was hypothesised that the suppression of the discharge channels was greater, leading to a thinner recast layer, however this requires further clarification, and consideration of liquid viscosity and bubble expansion created by machining. It has also been determined that a water-in-oil emulsion dielectric can generate a thicker, rougher but harder recast layer than kerosene and deionised water [230]. There is evidence that water in oil emulsion can cause an increased level of porosity and cracking in the recast layer (*see* Fig. 30) [230]. Increased porosity can be explained by an increased gas volume generated compared to kerosene, and smaller droplets of water which are more easily vaporised compared to deionised water. These gas bubbles generated become supersaturated gas in the molten pool, which leads to void generation.

4.2.5. Residual stress

Rapid cooling of recast layers on the surface of a solid bulk results in contraction and residual stress formation. These stresses, as expected, are mostly tensile in nature. This is typical of coatings cooling from the melt on substrates which are at much lower temperatures, since upon cooling, the layer is effectively constrained from contraction and pulled when it maintains a bond with the underlying bulk. The magnitude of these stresses increases with discharge energy [231]. In steels, retained austenite formation and distorted martensite have a strong correlation with residual stress [222]. Tensile residual stresses in EDM recast layers are a source of poor surface integrity, stimulating crack propagation and ultimate failure of the material [232]. To evaluate residual stresses of layers such as those produced by EDM, electro-chemical polishing techniques can be used to incrementally and accurately remove

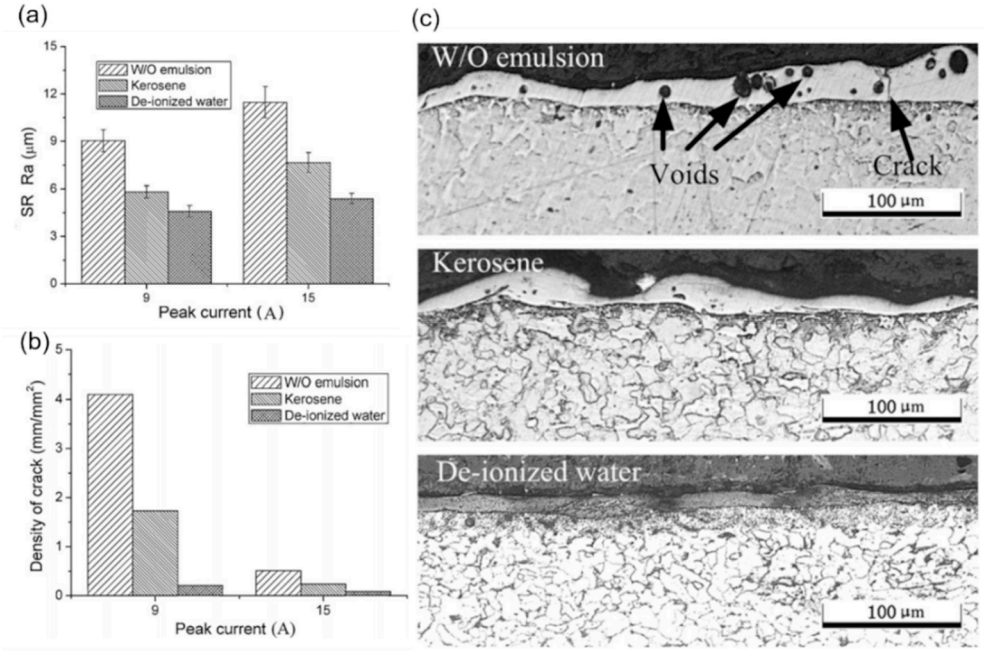

Fig. 30. (a) Roughness and (b) crack density of the workpiece for three dielectric types, with de-ionised water yielding superior recast layer properties in all cases [230]. Cross-sectional micrographs sowing increased thickness and void density in EDM recast layers machined using water-in-oil emulsion [230].

material, and combined with X-ray diffraction, allows measurement of residual stress levels with depth. This has been performed on various steels by Ekmekci et al. [222,231], with Fig. 31 (a) showing the correlation of the distribution of the residual stresses with depth from the surface. Klink et al. [233] also showed the influence of depth, dielectric type and roughing condition on the magnitude of residual stress in EDM layers revealing an extremely strong dependence of depth over which residual stress is present, on machining condition.

Residual stresses increase rapidly to a maximum tensile stress, close to the material's ultimate tensile strength near to the surface, then decrease to a relatively small compressive stress beneath the white layer [222], after which stress converges back to a zero value. The earlier work of Das et al. [232] supports the trend seen by Ekmekci with their residual stress model and experimental data, suggesting that just beneath the top surface, even from one single spark the residual stress level can reach close to the tensile strength of the material hence cracking commonly observed in EDM. At the end of a single discharge, the remaining melt pool quenches rapidly from the top due to the surrounding dielectric liquid, and from the base due to conduction, thereby yielding two solid-liquid interfaces with molten material between. It is thought that the temperature gradient at the surface is higher, and melted material rushes to fill cavities after end of discharge, and it is proposed that the final constriction of a region of cooling liquid between two, now solid regions of the recast layer, causes maximum tensile residual stress, near to but just beneath the top surface [222]. However, it should be noted this mechanism has only been theorised.

4.2.6. Surface enhancement via powder-mixed EDM

Luo [234] determined that the presence of gap debris actually stabilises the machining process, enhancing the distribution of discharges between electrodes in EDM, despite the ejection of debris from the machining gap being a fundamental practice of EDM to avoid catastrophic unintended sparking. Powder-mixed EDM (PMEDM) is a strategy while utilises debris in the gap to improve the surface finish of components machined by EDM.

It is known that powder added to the dielectric can manipulate discharge behaviour, and therefore change resulting recast layer properties [235,236]. Powders in the discharge gap generally modify its size resulting in enhanced flushing and debris removal, and a modified plasma energy density reaching the workpiece. In PMEDM, the stabilising effect of conductive powder added to the dielectric is exploited, enabling machining conditions that can yield better surface finishes upon machining. It is thought that the presence of electrically conductive powder effectively lowers the dielectric breakdown voltage, enabling discharges to occur across wider gaps. This facilitates flushing and reduces servo hunting, promoting more stable machining [235–237]. It has been shown that graphite, silicon and aluminium powder are the most effective at distributing discharges and creating glossy surfaces, using steels as example workpieces [235]. Several factors may explain why these materials are most successful. Firstly, they have good levels of electrical conductivity which is essential for providing an electrical pathway for dielectric breakdown. It has also been proposed that high thermal conductivity, i.e. in the case of

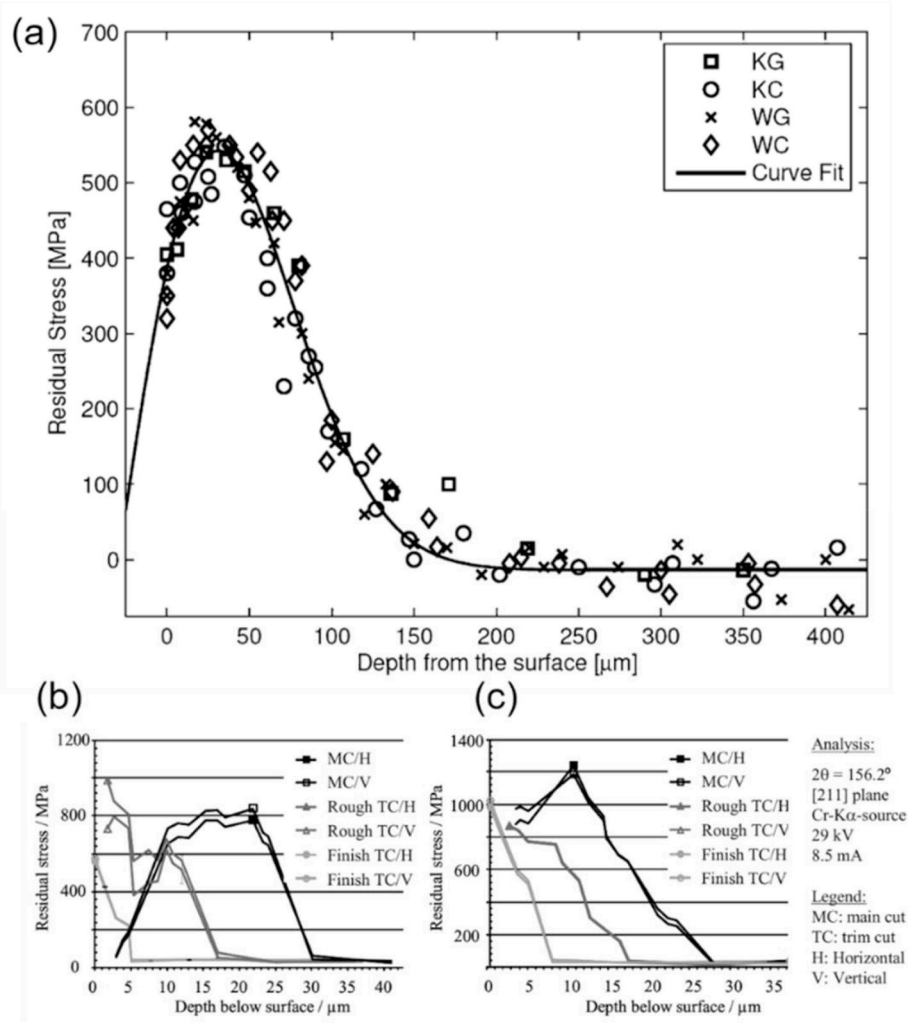

Fig. 31. Residual stress of (a) EDM processed steel surfaces, measured by Ekmekci using XRD [222]. Experiments were with kerosene and deionised water as dielectrics, and electrodes were graphite and copper. The abbreviations denote the combination – KG (kerosene/graphite), KC (kerosene/copper), WG (de-ionised water/graphite), WC (de-ionised water/-copper). EDM parameters used were not mentioned by the author, although parameters were kept constant. (b) and (c) residual stress with depth of EDM powder metallurgical tool steel after roughing and finishing cuts using (b) an oil-based and (c) a water-based dielectric [233].

graphite, may play a role in dissipating heat if the particle is directly in contact with the workpiece surface, thereby dissipating heat, reducing effect of the discharge [235]. Wong et al. also proposed that graphite's excellent lubricity may play a role in wetting/distribution of particles on the workpiece surface however, this is currently conjecture and not verified. It is clear however that buoyancy of the particles plays an essential role in their effectiveness in distributing spark location and increasing the gap width [238]. A SiC/Al metal-matrix composite has also been machined with PMEDM and roughness was decreased by 31.5%, compared to conventional EDM [239]. Some examples of surface and machining enhancements, based on the above mechanisms include the following, with images shown in Fig. 32. Silicon and graphite powders of 45 and 38 μm respectively have shown to generate a much smoother surface finish on steel compared to pure dielectrics [235], accompanied by more stable machining and shorter machining times, given the avoidance of "servo hunting", whereby excessive seeking and discharge delay time are reduced. A reduction in *Ra* roughness from ~0.8 to ~0.4 μm has also been seen in Inconel 718 machined by EDM using a 22 nm size graphite powder addition [240].

The use of surfactants in combination with an added powder also improves the surface integrity of EDM processed steel [241], based on the principle of separation of particles which tend to agglomerate together, thereby enhancing the actual distribution of powder particles. Although aluminium powder improved surface finish and reduced recast layer thickness, surfactant addition further improved these metrics. For example with Al plus surfactant, the recast layer thickness was 1–2 μm, compared to 5–8 μm for the kerosene dielectric. It is proposed that the surfactant maintained a more uniform aluminium distribution, thereby better maintaining the increased gap width due to the aluminium particles.

Through the analysis of individual discharge events and recast layers, further enhancements to the surface integrity of EDM processed materials through powder addition are revealed. It has been shown that aluminium powder can lead to the thinnest recast layer and the most expanded plasma channel in comparison to silicon powder [242], possibly explained by its greater impact on discharge distribution owing to its lower electrical resistivity. Chen et al. also noted that titanium powder of 35–45 μm size has the effect of reducing crack formation in pure titanium [243], however an explanation for this was not provided. The reasoning may be consistent with that given by Murray et al. [238], where the increased gap size resulting from the presence of conductive particles results in a less restricted expansion of the bubble formed after discharge, resulting in reduced impact force in the melt pool region – an indicative schematic of which is shown in Fig. 33. This mechanism is likely responsible for the general improvement in surface finish for powder mixed machined parts.

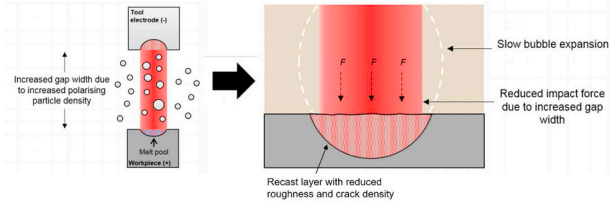

Fig. 33. Mechanism of reduced recast layer defects and roughness via expansion of the discharge gap through powder. Adapted from the authors' prior work [238].

4.2.7. *Mitigation of surface defects and electrical discharge coating (EDC)*

In conventional EDM, avoidance of wear of the tool electrode is critical to maintaining machining process accuracy. Tool wear can also be exploited to create coatings on workpieces. EDC can also produce coatings using powder suspended in the dielectric fluid resulting in direct deposition onto a target workpiece surface. In EDC, sparking is effectively conducted as normal, albeit with some specific parameter sets. Typically negative tool polarity, high gap voltages, short pulse on-times and long pulse-off times are used to increase material removal and adhesion. The high temperatures associated with discharges allows a range of materials to be deposited, including electrically conductive ceramics [213,244]. A unique advantage of EDCs is that they can be combined into a unified process chain whereby normal machining of a complex shape by EDM is performed, followed by coating of the machined surface by a hard layer.

EDCs have a thickness that matches that of the recast layer expected, if machined under normal conditions. Effectively, coating deposition rates match the removal rates of substrate materials via the sparking mechanism. This means that material from the sacrificial tool electrode, or material suspended in the dielectric, is absorbed into the molten zone formed via sparks. The most commonly deposited material via EDC is TiC [245,246]. TiC has been deposited as a thin coating via both suspended TiC powder, a Ti electrode reacting in-situ with carbon in the dielectric, and directly via a sacrificial sintered tool electrode.

To more widely use ED coatings in real load bearing applications, an understanding of the microstructure of such coatings is essential. To demonstrate a typical scenario under which EDCs may be applied, microstructures of TiC-based coatings on steel substrates have been studied using TEM of both single deposits and continuum coatings [247]. Coatings contain a majority (approximately 70% by weight) of TiC, with the remainder comprising substrate material. The TiC comprises equiaxed grains of down to ~50 nm size near the top surface, beneath which is a columnar zone of TiC, followed by a region of more equiaxed TiC grains between this region and the substrate-coating interface. Substrate

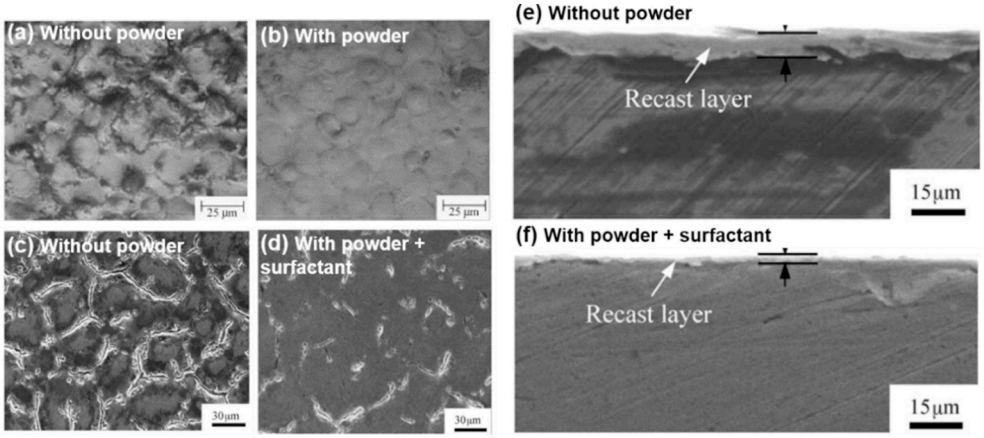

Fig. 32. EDM (a) without and (b) with powder-mixed in dielectric [235], (c)–(f) show the effect of aluminium powder + surfactant in the dielectric on surface morphology and recast layer thickness in tool steel [241].

material, (mainly Fe in the case of the referenced study) is present between most grains in the coating, drawn up into the coating through capillary action during melt lifetime, and the coating is a composite - Fig. 34 shows cross-sectional images of an EDC-fabricated TiC based coating. The understanding of such coatings as composites is important for their final application, given a combination of properties of coating and substrate materials may be introduced and define the overall coating properties.

Depending on the coating or substrate material, and deposition parameters, cracking and porosity may be introduced into EDCs. Hard ceramics, like TiC, exhibit lower thermal expansion coefficients than most metals. As a result, such ED coatings are sometimes characterised by high crack densities. Cracking and porosity have been observed in TiC coatings produced from titanium/graphite sandwiched electrodes [248], and coatings of TiC produced from Ti particles suspended in oil [249]. Porosity associated with EDM and EDC can be attributed to either boiling of the material or trapping of gas. The proliferation of cracks is thought to occur through aggressive sparking conditions, or by the development of multiple phases with differing thermal expansion coefficients [250]. Using a silicon sacrificial electrode combined with a TiC coating can yield a crack free layer [238], shown in Fig. 35. In this way, with correct experimental conditions and choice of electrode type, the negative effects of cracks and pores can be mitigated.

Future applications of EDCs such combination of materials should be considered for manipulation of the morphological properties, while mostly maintaining the mechanical properties of the intended coating material. It has been shown that the discharge itself can be manipulated via the presence of silicon debris in the discharge gap [238]. The silicon increases the gap width via its increased buoyancy relative to TiC, resulting in less violent material expulsion and re-solidification mechanisms. This is thought to be caused by reduced impact forces during discharge, however multiple complex mechanisms occur, and short discharge time-scale does not allow direct imaging of the phenomena. This mechanism is also supported by Sumi et al. [251], who observed a similar improvement in crater characteristics when using silicon. Therefore, the overall buoyancy of the coating material, and of the second material used in the case of a combined coating, should be carefully considered when aiming to achieve crack-free EDCs. It should be noted that without EDC, methods of mitigating surface defects are possible via new generator technologies. For example the “enlarged generator” settings can allow flattened EDM craters, thereby mitigating some potential negative effects such as increased friction or stress concentration. The mechanism of the enhanced crater diameter is that a greater channel diameter is reached more quickly, with a reduced current density, stopping some of the removal process and thereby causing only melting/recasting in certain regions [252]. Adjusting dynamically between spark generation technologies is likely to play a key role in mitigation of the deleterious recast layer.

The complex, thermal nature of the EDM process means that as well as producing a range of undesirable features on machined metals, there are various modifications to it to mitigate some of these defects (Fig. 38), which ultimately provide favourable morphological, microstructural and mechanical properties.

In Fig. 36 (a) and (b), different EDM recast layer types are contrasted. It is shown that typical EDM surfaces contain porosity, cracking and high levels of roughness. However, the addition of certain powders, modifies discharge behaviour to produce a less severe recast layer, with reduced cracking, porosity and roughness. Furthermore, additions of certain electrically conductive powders can also enhance material removal rate.

Coatings can also be used to mitigate negative recast layer properties, or enhance certain properties, typically hardness and wear resistance. Schematics of these methods are shown in Fig. 36 (c)–(e). Addition of powder directly to the dielectric (see (c), which is agitated or suspended, is deposited directly into the workpiece surface via discharges, resulting in coatings which are composites of the powder (in this case TiC) and the substrate. Alternatively, as shown in (d) addition of carbon-based powder to the dielectric in combination with titanium, which can react with carbon, can result in in-situ formation of TiC in the recast layer. This approach may have some advantages given graphite powders may be more available than TiC powders. This is different to the method shown in (e), where powder-sintered electrodes are used, and discharges eject material from the electrode into the discharge gap and subsequently into the workpiece surface, again forming a composite coating.

5. Mechanisms governing the chemical/electrochemical effects upon surface integrity

Of the chemical/electrochemical machining processes, electrochemical machining (ECM) techniques are among the most industrially relevant for processing metal workpieces for load-bearing applications. Although widely regarded as imparting excellent surface integrity directly from the process, ECM can result in an array of surface effects, depending on the material and part complexity. Variations in surface integrity arise from poor control over the dissolution regime and electrolyte flow conditions over a part resulting from material-electrolyte

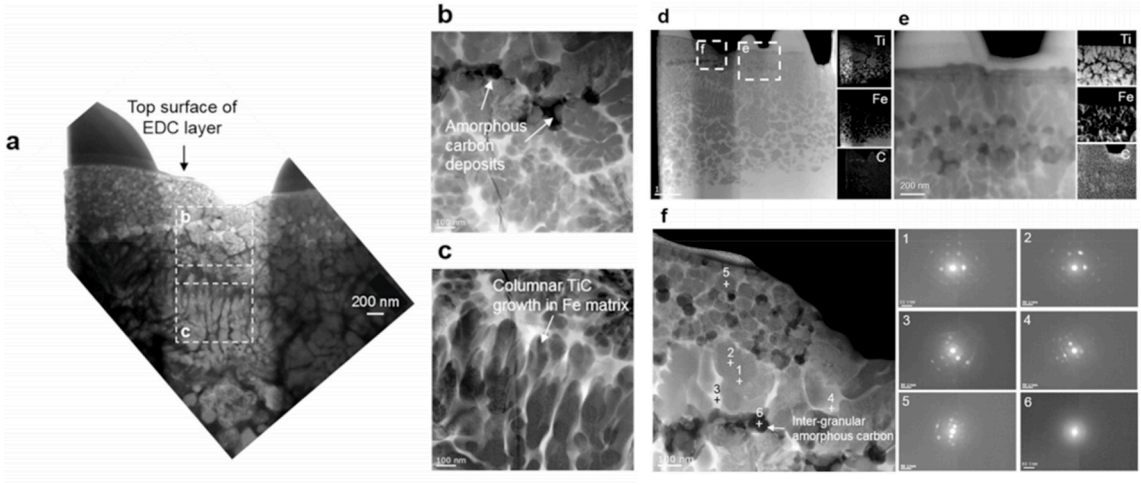

Fig. 34. (a) TEM micrographs of microstructure of TiC-based thin EDCs deposited on stainless steel substrates [247]. (b)–(f) Scanning transmission electron images of microstructure. A fine equiaxed near-surface structure of TiC in a Fe matrix is present, below which are columnar grains of TiC followed by larger more randomly oriented grain beneath this.

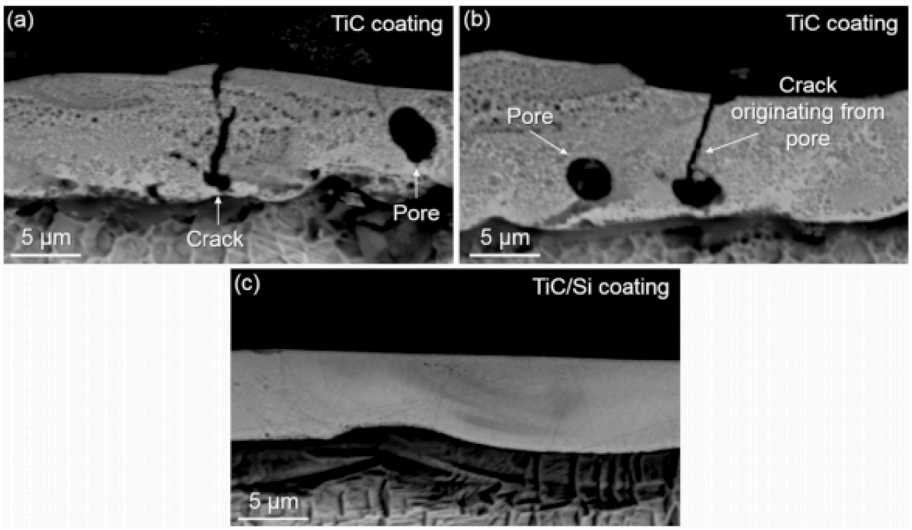

Fig. 35. (a) and (b) TiC based coatings containing some defects and (c) TiC/Si composite coating with defects eliminated [238].

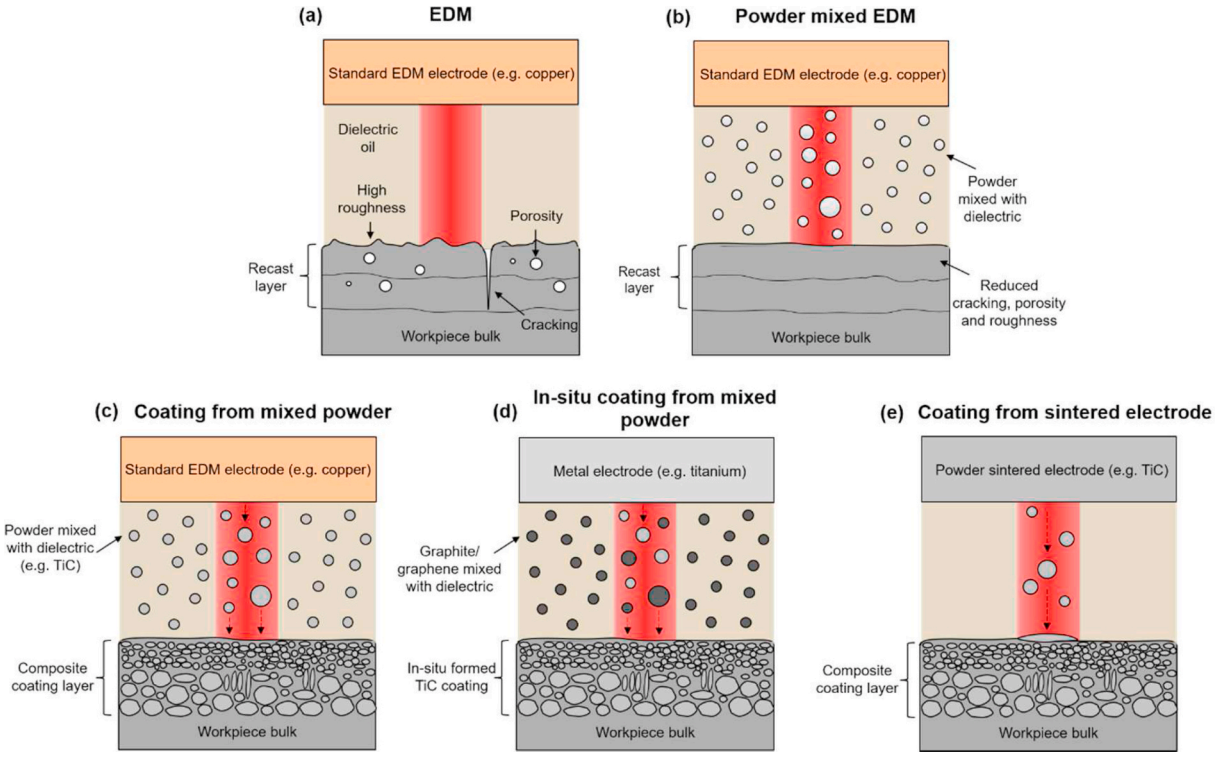

Fig. 36. Schematics of the various different forms of ED machining and coatings.

interactions, and complex geometries [253]. Material removal can be sensitive to workpiece condition (metallurgy, composition, and reactivity) in addition to machining parameters, control over the resulting surface integrity is challenging to realise in many alloy systems [254]. In ECM, as with anodic dissolution methods such as electropolishing, material removal occurs on an atom-by-atom basis. A potential is applied between the tool electrode (cathode) and the workpiece (anode), and a conductive electrolyte, usually aqueous $NaNO_3$ or NaCl, flows at relatively high velocities (10–60 m/s) in the inter-electrode gap (IEG) [255]. The removal process requires a continuous flow of electric charge between the electrodes through the electrolyte, where the supply of anions to the workpiece surface is controlled by convection, diffusion, and electrostatic migration [5,256]. As such, ECM processes are sensitive to changes to applied energy, electrolyte flow rates and viscosities. As a fluid electrolyte is required in ECM, operating temperatures must not exceed the boiling point of the electrolyte, where Joule (resistance) heating can raise the IEG electrolyte temperature significantly, especially where there is excessive hydrogen evolution at the cathode [257]. However, relatively low operational temperature ranges in aqueous electrolytes negate thermal surface effects in most relevant engineering materials. Furthermore, as a consequence of the atom-by-atom dissolution, material lattice parameters are generally retained from the near-surface into the bulk and the subsequent effects on mechanical properties such as residual stress and hardness are negligible [255,258,259]. Despite this, electrochemical processing methods can impart deleterious effects on surface integrity by other mechanisms [260],

where inappropriate processing conditions are applied.

Adaptions of ECM techniques include die-sinking (Fig. 37 (a)) in which a cathode tool is sunk into the workpiece, and selective removal methods that are suitable for micromachining (depending on tool size and geometry), where high precision removal is required [261]. Micromachining examples include electrolyte jet machining (EJM) [262], wire-ECM [263], and electrochemical micromachining (ECMM) that applies ns-pulse power to exploit the linear relationship between the charging constant of the electrical double layer and the distance from the tool electrode. As such, ECMM can realise sub-micron precision [264].

In order to consider the surface integrity arising from ECM methods, one must understand the different dissolution regimes that can drastically affect the resulting surface. Generally, reactions in the IEG follow Fig. 37 (b), in which a surface metal atom is oxidized by the charge and usually hydrolyses in the electrolyte. At the cathode, charge is generally transferred by the reduction of water to evolve hydrogen. However, material removal can occur in ECM with varying dependence on the underlying material, determined by the processing conditions. For single-phase materials, this is the difference between isotropic removal (polishing) [265], and anisotropic removal (etching) [266]. Most engineering materials are however more complex, being composed of multiple phases or precipitates, and therefore the resulting surfaces arising from ECM are affected by different formation mechanisms.

5.1. Anisotropy and grain boundary etching

Ultimately, the anodic dissolution mechanisms in ECM are essentially the same as those for electropolishing [5], and it is broadly understood that to maintain a smooth workpiece finish (isotropic to the underlying material), it is necessary to develop a polishing film at the anode. This can be understood through the principle of a diffusion layer and can be intuitively expressed generally by either product- or acceptor-limited mass transport control [267]. Fundamentally, an electrochemical reaction consuming a reactant and generating a product at an electrode will create concentration gradients as the reactant is consumed and the product is generated (Fig. 37 (c)). Clearly, the gradient magnitude is proportional to the reaction rate, and as this factor increases, the concentration of the reactant will tend towards zero and the product will tend towards its saturation concentration, at the electrode. The current density at which either the surface concentration of the reactant species reaches zero, or the product reaches saturation, is the diffusion limiting current density (Fig. 37 (d)).

In many cases, dissolution in ECM is governed by the product-limited mechanism [267]. Below the limiting current density, where the metal cation concentration is below saturation, the location on the surface at which a metal atom is liberated is determined mainly by the surface free energy. This is dependent on the crystallographic direction of the lattice, and any perturbations and discontinuities, such as grain boundaries and defect sites [268]. The surface finish is defined by the slow etch directions of the material and therefore becomes anisotropic (Fig. 37 (e)).

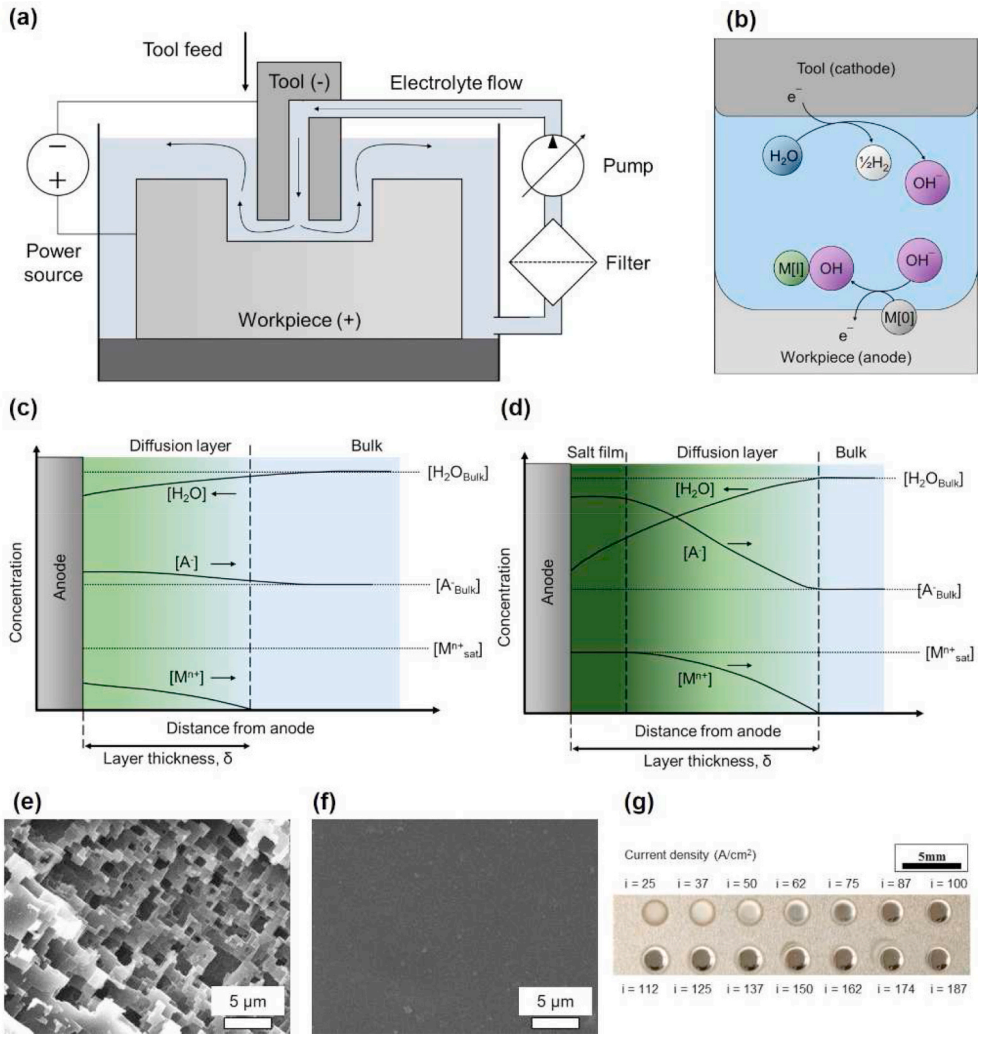

Fig. 37. (a) Typical die-sink ECM setup, with electrolyte supply through the tool and recirculation. (b) Schematic of the inter-electrode gap, showing metal oxidation at the anode and hydrogen evolution at the cathode. (c) Diagrams showing concentration gradients in the anode-electrode interface below and (d) above the limiting current condition for the product-limited dissolution model (adapted from Ref. [271]). Arrows indicate diffusion fluxes of the species. (e) Anisotropic etching of (100)-oriented Al alloy in EJM below limiting current density (30 A/cm^2) and (f) smooth polished surface above limiting current density (300 A/cm^2) [266]. (g) A broad range of finishes produced using EJM on stainless steel [269].

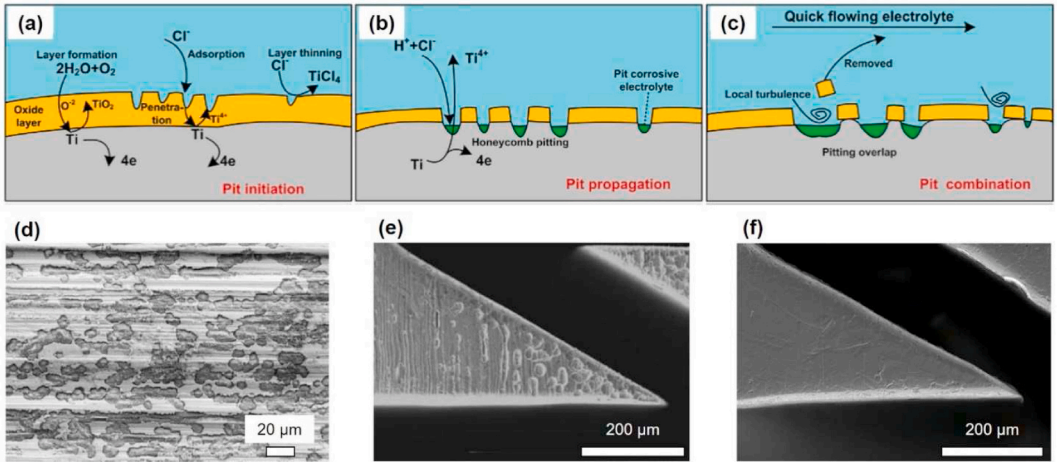

Fig. 38. Pitting and stray current attack affect surface integrity in ECM. Stages of pit growth in Ti-alloys: (a) initiation, (b) propagation, and (c) combination and oxide removal [276]. (d) Pitting can occur in Ni-superalloys at low current densities, aligning with pre-existing grind marks [283]. (e) Travelling wire-ECM without, and (f) with insulating shield to reduce stray current attack [284].

Beyond the limiting current condition, the metal ion concentration at the anode reaches saturation and a viscous salt film forms over the anode, inhibiting dissolution defined by surface energy alone. Instead, the dissolution location is determined by the location of vacancies within the viscous or compact salt film into which a metal cation product must migrate. These vacancies are stochastic in nature, and as such material removal is disconnected from the underlying crystallographic lattice and a smooth, isotropic texture is revealed (*see* Fig. 37 (f)) [266].

Practically, this means that grain boundary effects and surfaces defined by perturbations in the material can be overcome by: i) increasing the process current density, ii) lowering flow velocities (suppressing the evacuation of salt films), and iii) increasing electrolyte viscosity. The latter however, can result in flow marks on the surface depending on the supply conditions. This explains the trend towards higher current densities and this effect is shown in the context of EJM (Fig. 37 (g)), where both anisotropic and isotropic surface finishes can be generated [269]. Application of low current densities in ECM has been reported to affect the fatigue strength due to the associated discontinuous surfaces [270]. EJM is an interesting case in this regard, as the high relative velocity of the impinging jet decreases mass transport layer thickness, thus anisotropic surface textures can be observed at higher current densities than with conventional ECM.

5.2. Surface films and corrosion pits

The formation of high aspect ratio corrosion pits on ECM surfaces is closely related to the nature of the surface oxide films that can either be native on the metal, or resulting from anodic reactions, as well as the precise local electrochemical environment on the anode. A lack of parametric control in ECM can lead to poor surface integrity, characterised by high aspect ratio holes on the workpiece surface within or beyond the desired machining zone. Surface pits are understood to act as stress concentrators and can have significant implications for the fatigue life and corrosion resistance of parts [272].

For common engineering metals such as steels, Ni-superalloys, and Al-alloys, appropriate parameter selection can enable the breakdown of native surface oxide films, allowing controlled anodic dissolution of the underlying material. Residual oxide films can be retained at the surface after machining such materials, for example Borchers et al. [36] reported a thin (50 nm) surface oxidation zone on steel (AISI 4140) after ECM. When electrochemically processing passivating materials like Ti-alloys, surface films can be particularly problematic. Such materials feature widely in applications where corrosion-resistance and high specific strength are required. In the context of Ti-alloy ECM, oxide film growth occurs at the surface resulting from the reaction with water from the electrolyte (see Fig. 38 (a)), which inhibits anodic dissolution of the metal. Practically, this is generally overcome through the application of electrolytes containing halides, particularly chloride and bromide [273]. These anions promote the breakdown of the oxide layer, especially in areas of the film with greater electrical conductivity [274], and lead to pitting. The superposition of these pits enables the formation of a stable material removal process. The generation mechanism is related to the material and the processing conditions, but the majority of pitting events progress through discrete sequential steps. Firstly, initiation – the electrochemical breakdown of the passive film (*see* Fig. 38 (a)), secondly, propagation – the development of a local aggressive (low pH) chemical environment in the pits [275], enabling growth (see Fig. 38 (b)), and iii) finally, combination – where enlarged cells overlap to form larger crevices (see Fig. 38 (c)) [276]. Subsequent combination steps allow increasingly larger active dissolution cells to cover more of the workpiece leading to stable machining with the polishing condition regulated by the salt film condition [265].

When processing Ti-alloys with ECM, It has been shown that electrolyte selection can radically alter pitting characteristics [277], and surface morphologies throughout electrochemical processing [278, 279]. In addition, the integrity of the workpiece oxide layer has been shown to affect the local propensity of initiation [280]. The development of non-aqueous electrolyte systems such as those based on ethylene glycol mixtures can reduce the formation of anodic oxides by reducing water concentrations [281]. In addition, glycol-based electrolytes particularly favour the development of the polishing film condition, resulting from higher electrolyte viscosity. This enables the acquisition of bright, pit-free finishes [282]. While non-aqueous electrolyte systems are emerging as a route through to improving the electrochemical processing of highly passivating materials (for example Ti-alloys), further research is required to understand the effect of the higher viscosities on the surface generation mechanism. This is particularly important considering the high susceptibility to debris effects and poorer control over the hydrodynamic flow conditions, under ECM conditions (Section 5.4).

In some cases, pitting can occur outside the machining zone in ECM, away from the tool electrode but within the electrolyte. This is often termed ‘stray current attack’, and is indicative of the presence of an undesirable non-zero current density in this region. This phenomenon is particularly associated with selective electrochemical processing techniques, such as wire-ECM, EJM, and ECMM, where there is a well-defined machining region. Furthermore, stray current attack can lead to pitting in non-passivating materials such as steels and Ni-superalloys

(see Fig. 38 (d)) [283]. Routes to reduce stray current attack and pitting include appropriate insulating shielding of the tool electrode (see Fig. 38 (e)–(f)) [284], changing the flow condition between the electrodes [285], and appropriate parameter and electrolyte selection [264]. Material removal can also be further localised to the machining zone by applying additional energy sources, such as laser power, to increase the local electrolytic conductivity and mass transport conditions [52,286]. Selective and hybrid methods combining electrochemical processing with alternate energy sources such as lasers and electrical discharges have been reported, however further work is required to examine precisely the effect of these combined thermal processing steps of the surface integrity of the finished surface.

5.3. Preferential phase dissolution

Materials containing secondary phases like precipitation-hardened alloys feature widespread application where the design intent is mechanically robust, high-temperature resistant, or hard-facing parts. However, secondary phases can often be semiconductors or insulators, or dissolve slower in ECM than the matrix material, and therefore protrude from the surface. The dissolution rate is defined by the electrochemical equivalent, according to Faraday's laws of electrolysis [287]. This dictates the mass of a substance removed in an ECM process is proportional to the charge, atomic mass, and the change in oxidation state. For multiple phase materials [58], or even single crystal [288], and single-phase materials possessing inhomogeneous compositions, this will result in inhomogeneous topography [289]. Phases or locations with greater volume-corrected electrochemical equivalent (the material mass removed per unit charge) will remove at a faster rate, assuming equivalent current density distribution [290]. Therefore, the final surface morphology of complex materials processed by ECM is difficult to predict. In most cases however, increasing the anodic dissolution rate (i.e. by increasing the machining current density and applied potential) will decrease topographic undulations resulting from inhomogeneous compositions.

An example of post-ECM surface finish in a complex material system (pearlitic steel hardened by inert lamellar Fe_3C), shown in Fig. 39 (a), where Fe_3C lamellae protrude from the surface after processing, in experimentation carried out by Haisch et al. [291]. Fe_3C is more brittle than the α-ferrite matrix material and this decreases surface integrity. The authors acknowledged that while the Fe_3C phase is electrically conductive, the oxygen evolution reaction (OER) readily occurs instead of the anodic dissolution of Fe_3C. This means that upon high rate anodic dissolution (*see* Fig. 39 (b)), the anode surface is likely to become covered by a film of protruding Fe_3C, which may collapse to cover the active metal sites as the removal depth approaches the scale of the lamellae. The localised current density and electrical field lines at the surface of an ideal two-phase pearlitic material were simulated by Klocke et al. [292] (see Fig. 39 (c)–(d)). Upon initiation of ECM, the local current density is focussed at the interface between the steel and the Fe_3C, while rounding of Fe_3C particles occurs after a time step. The focusing of local current density at the interface between phases of differing resistance to ECM was experimentally verified in other materials, such as brass shown in Fig. 39 (e), where more inert brass α-phase grains are undermined and often washed out [58]. Similar particle wash-out events have been observed in the ECM of Ni-superalloy Inconel 718 [293]. Particle wash-out phenomena will lead to surface cracks and crevices of sharpness partially determined by any angular features in the precipitate particle.

As novel high-temperature materials are developed, like advanced metal-matrix composites that hold multiple and often electrochemically inert phases, the dissolution mechanisms and the resulting profiles will change significantly, which could affect pit formation and enable significant undermining and passivation layer formation. In such cases, a substantial effort will be required to retain the level of process control necessary to impart the required level of surface integrity in a consistent manner over a finished component.

5.4. Flow and gas affected surfaces

Flow marks are periodic topographic undulations that can occur on the surfaces of workpieces processed by ECM. These are the result of interplay between both hydrodynamic and electrochemical phenomena [290]. Fundamentally, electrolyte flowing across a workpiece surface will experience an associated drag force forming a boundary layer, which alters the velocity profile. This can lead to local turbulence,

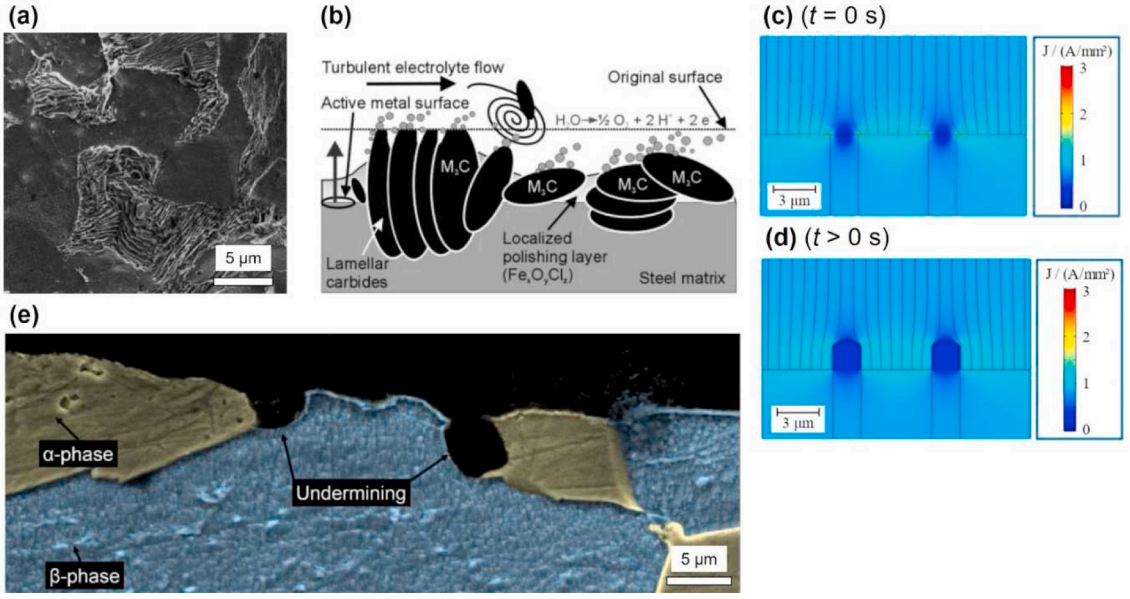

Fig. 39. (a) SEM micrograph of a post-ECM surface processed in pearlitic steel. (b) Upon dissolution, surfaces are likely to become covered by films of carbide materials, limiting active metal sites and promoting oxygen evolution [291]. (c) The local current densities upon ECM in a similar material can be simulated to show the evolution of topography, [292]. (e) Colourised SEM of sectioned ECM surface in dual-phase brass showing undermining of the electrochemically resistant phase [58].

vortices and bursting phenomena near to the anode surface. Firstly, diffusion layer characteristics at the anode are sensitive to changes in electrolyte velocity, modifying the electrochemical regime, for example between active dissolution and passivation. Furthermore, higher mass flow rates are more efficient at electrolysis product evacuation from the interface. This will increase the local electrolytic conductivity and result in higher current densities, where the electrical field strength and electrolyte temperature are constant. In such cases, the dissolution topography will tend towards periodic undulations, such as flow grooves (Fig. 40 (a)). These can be exacerbated when the material has discrete phases, such as precipitates that protrude from the surface after machining; these interact with the electrolyte flow disrupting dissolution, shown in the case of steel (42CrMo4) with protruding carbide precipitates (Fig. 40 (b)), although the authors noted that the appearance of grooves was not systematically triggered [260]. This makes it challenging to predict the post-ECM surface for precipitation-strengthened materials over complex geometries, where the hydrodynamic conditions are difficult to control. As such, the precondition of the material affects the formation of flow marks, for example in Fig. 40 (c)–(d) (Inconel 718), which shows both the precipitation-strengthened and solid solution alloy, after ECM [294].

In addition to flow effects, ECM surface integrity can be affected by the generation of relatively large volumes of oxygen gas at the anode, and this must be considered when selecting electrolyte-workpiece combinations. Gas bubbles will interfere with the local current density distribution (Ohmic effect), disrupting material removal. Oxygen evolution can be observed when processing materials such as Fe and Ni-alloys with passivating electrolyte systems, such as $NaNO_3$ [295,296]. Additionally, increasing volumes of oxygen gas will increase the Joule heating effect in this region, and can lead to vaporisation and uncontrolled spark discharges across the IEG. Again, enhancing the flushing condition will enable greater evacuation of oxygen gas and other dissolution products from the anode.

6. Combined effects occurring during machining upon surface integrity

While singular material removal mechanisms govern some processes (e.g. mechanical effects in AWJ machining and thermal effects in laser machining), in most circumstances a combination of these occur. This can be manifested in single processes (e.g. conventional machining under aggressive cutting conditions), and also in hybrid machining processes, e.g. laser assisted machining (LAM), and electrochemical discharge machining (ECDM).

6.1. Combined effects in conventional machining

6.1.1. Thermo-mechanically induced grain refinement

In conventional machining (Section 3), apart from mechanically-induced load defects, the surface may also be affected by high cutting temperatures. This is due to the nature of energy transformation from workpiece plastic deformation (primary deformation zone), and friction (secondary and tertiary deformation zone) phenomena, that accompanied with mechanical loads, can strongly affect tool performance and surface integrity [297,298]. This normally occurs when aggressive cutting conditions are applied, e.g. roughing processes, severe tool wear, lack of coolant, or when cutting low thermal conductivity workpieces (e.g. superalloys). In these circumstances, when high cutting temperatures are induced in combination with mechanical effects, significant surface damage can be generated leading to oxidation, corrosion, phase transformation and recrystallization.

The most common thermal influence is to soften the material, which combined with the mechanical effects may significantly deform materials and lead to severe sub-surface plastic deformation. If temperatures are high enough to reach the recrystallization temperature, new grains may nucleate by accommodating dislocations from highly deformed (broken-down and elongated) grains, leading to equiaxed grains with well-defined boundaries. This is termed dynamic recrystallization, or thermally-induced white layer (T-WL). This is different from the

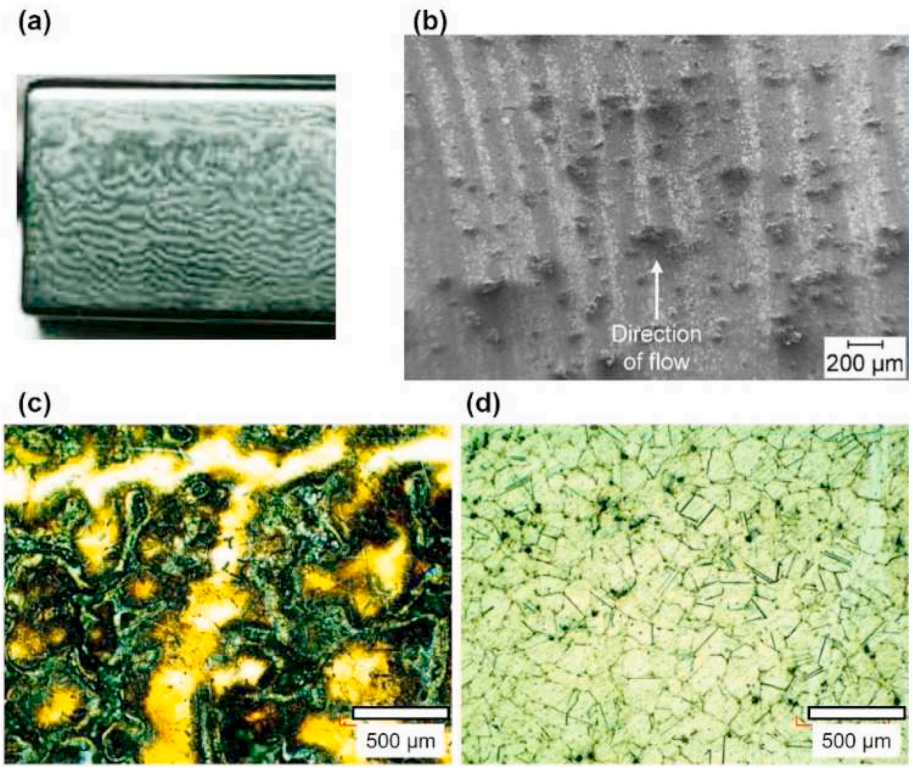

Fig. 40. Flow-affected ECM surfaces. a) Periodic undulations on die steel after ECM [290]. b) Precipitate-induced flow grooves in 42CrMo4 steel (flow direction marked) [260]. Optical micrographs after ECM of c) precipitation-strengthened (aged) Inconel 718, showing mottled polished and rough areas around precipitates, indicative of complex hydrodynamic conditions. d) The ECM process, but with the solution-treated Inconel 718 alloy as the workpiece, showing a polished, undulation-free surface [294].

mechanically induced white layer, where only subgrains are formed from the breakage and elongation of original grains by mechanical loads. However, as the cutting heat is caused by the material deformation (Zone I in Fig. 6) and friction between tool and workpiece in the cutting area (Zone II and III in Fig. 6), the thermal effects do not occur in isolation, but accompanied by mechanical effects. Hence, in this case, the machined white layer could contain two layers: T-WL (dynamic recrystallization layer) on the top and M-WL beneath (dynamic recovery layer). TEM observation of machined white layers from carbon steel (Fig. 41 (b)) show the equiaxed microstructure of the T-WL (average grain size ≈10 nm), while beneath the T-WL, a submicron (≈200 nm size) grain structured M-WL with a mixture of subgrains and twinned grains exists.

Nevertheless, as high temperatures are reached, the T-WL is always accompanied by phase transitions in the near surface region. Due to rapid cooling (10^5–10^6 K/s) [65,114], these phase transitions are frozen and no recovery of the original phases occurs. Fig. 41 (b) shows diffraction rings from ferrite (bcc structure), formed in dynamic recrystallization layer (T-WL). In the dynamic recovery layer (M-WL), only the original phases (e.g. austenite, twinning martensite, and ferrite) are found. Similarly, Fig. 42 shows dissolution of γ′ precipitates in the T-WL of a machined nickel based superalloy due to high temperature damage, while M-WL, γ' precipitates are deformed rather than dissolved. Furthermore, high oxidation rates are also found in the white layer, from the high temperature effects.

Nevertheless, when white layers are formed under combined thermo-mechanical effects, their thickness strongly depends on cutting parameters and the material properties that influence the resultant mechanical loads and cutting temperatures. Li et al. [123] reported that white layer thickness in carbon steel increases with feed rate, cutting speed and drill diameter (Fig. 43), resulting from the increase in the deformation energy imposed on the machined surface. Moreover, this thickness is also influenced by workpiece material properties (e.g. hardness) for given cutting conditions. For example in Fig. 44, only grain deformation occurs when workpiece hardness is relatively low (2.9 GPa with matrix structure of pearlite), while a much thicker (8 μm) white layer is generated when machining tempered martensite, which has a higher hardness (7.8 GPa). This is due to the higher deformation energies and cutting temperatures yielded from harder workpieces, as well as decreased thermal stability when heat treatments were employed to increase the material hardness, which might decrease the phase transformation temperature.

6.1.2. Work hardening and thermal softening

As mentioned in section 3.2, in conventional machining, mechanical loading usually generates a hardening effect on the machined surface caused by induced plastic deformations. However, when high cutting temperatures occur, a softening effect on the machined surface is observed, mainly caused by over-aging from the cutting heat energy, which eventually reduces machined surface hardness. This usually occurs when machining high strength and/or heat resistant materials (e.g. low thermal conductivity) under high material removal rates and/or with insufficient coolant applied. When one of these effects is much milder and can be neglected, a single effect then can be observed such as hardening (Fig. 45 (a)), or softening (Fig. 45 (b)). On the contrary, when these two effects yield a similar magnitude, then a combined influence is observed, shown in Fig. 45 (c) and (d), where a fluctuating change in hardness is induced along the superficial layer, where both hardening and softening effects are shown.

Furthermore, while mechanical effects can generate compressive residual stresses in machined workpieces due to plastic deformation, thermal effects on the contrary cause localised material expansion and lead to tensile residual stresses. Like hardness, when a combination of these two effects occurs in machining, i.e. both the compressive and tensile stresses are present, and a "hook" profile is usually yielded, due to the mutual compensation of these two effects. This is because the thermal (tensile) effects usually appear over shallow layers, while mechanical effects penetrate much deeper. Specifically, when maximum residual stresses from thermal mechanisms are greater than those from mechanical mechanisms, resultant residual stresses will be tensile immediately beneath the machined surface (near-surface), turning compressive with increasing depth beneath the machined surface (Fig. 46 (a)). This is disadvantageous as the tensile stresses facilitate the initiation and propagation of fatigue cracks and surface rupture. On the contrary, when the magnitude of the maximum compressive residual stress is greater, only compressive residual stresses would be compiled (Fig. 46 (b)), which is beneficial for extending fatigue life of machined workpieces.

This thermo-mechanical mechanism can also impact the superficial layer strength, which can be revealed by micromechanical testing [65].

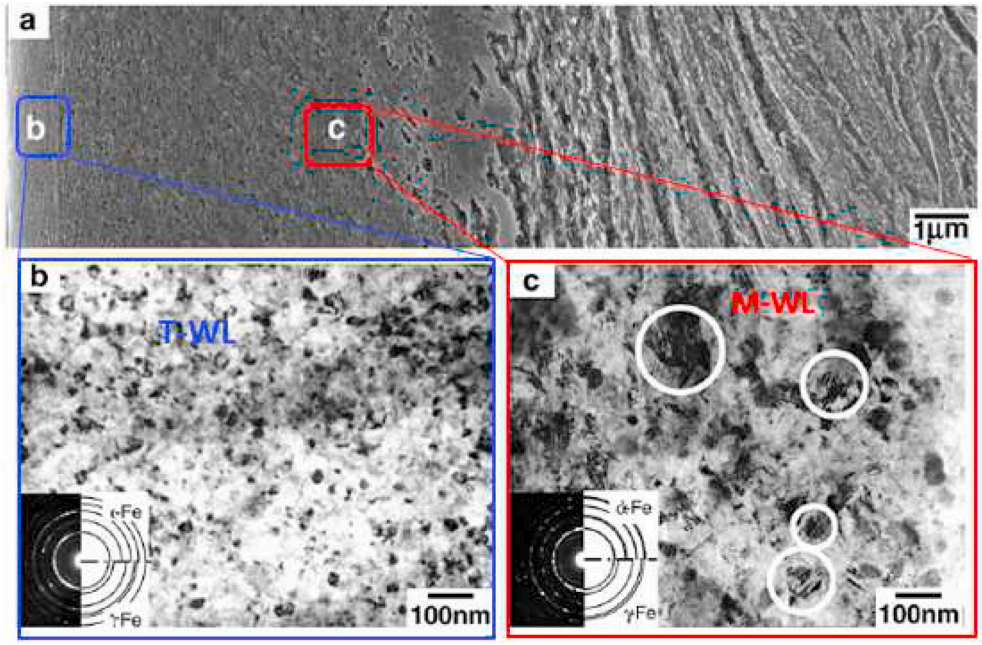

Fig. 41. White layer of drilled carbon steel: (a) SEM image from global view, (b) TEM bright field images of T-WL and (c) M-WL [123].

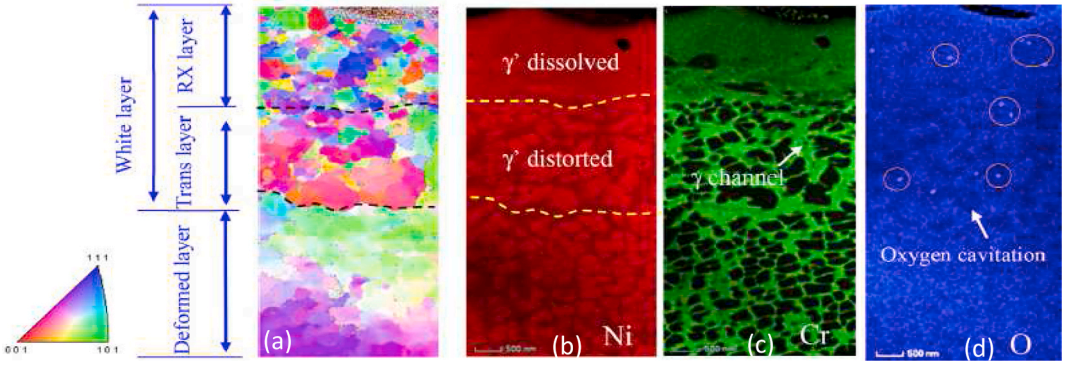

Fig. 42. (a) TKD observation and (b)–(d) elemental distribution in superficial layer revealing the evolution of gamma prime in the machining process of a nickel-based superalloy [65].

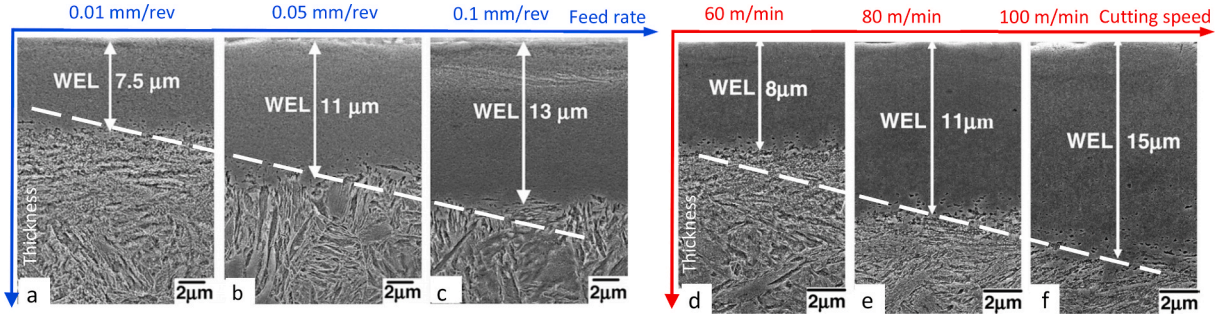

Fig. 43. Thickness of white layer of machined Fe–0.56% C steel with an as-quenched martensite structure: (a–c) at different feed rates (cutting rate: 80 m/min, drill diameter: 5.0 mm) and (e–g) at different cutting speeds (feed rate: 0.05 mm/rev, drill diameter: 5.0 mm) [123].

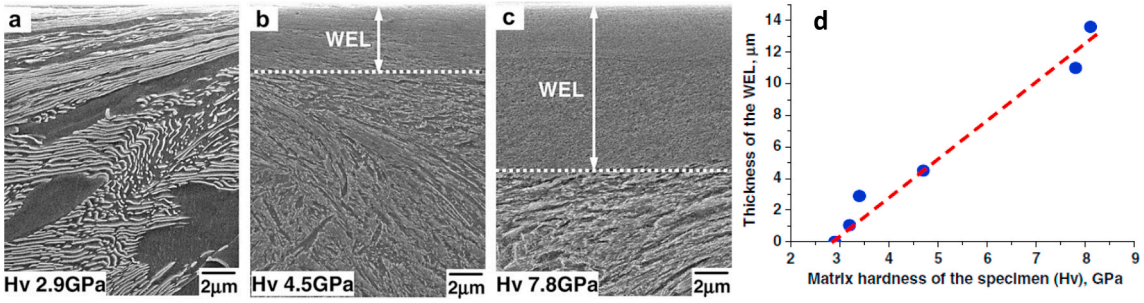

Fig. 44. Thickness of white layer of machined Fe–0.56% C steels with different matrix microstructures: (a) pearlite, (b) tempered martensite and (c) martensite, (d) the relationship between the thickness of white layer and matrix hardness of the material [123].

Fig. 47 shows a micropillar compression test on the bulk layer, and white layer of a machined Ni-based alloy. The resulting plastic strain energy (energy dissipated in plastic deformation) and stress-strain curve of the micropillars for the bulk material start to increase after the stress reaches a critical value (i.e. yield stress-1000 MPa), while in the machined white layer, there is almost no elastic recovery even, at low stresses (e.g. 300 MPa). This 'direct to plastic' behaviour explains the deterioration of mechanical performance from the high cutting temperatures.

6.2. *Combined effects from hybrid machining*

Hybrid machining processes employ two different energy sources/processes, normally conventional machining (predominantly mechanical loads) and nonconventional machining (predominantly thermal/chemical loads) to improve the machinability of workpiece materials. This is achieved either through an assisted effect, where one process (normally shear based machining) dominates, e.g. laser-assisted machining, or a combined effect, where different processes interact simultaneously in the same zone, e.g. simultaneous EDM and ECM. In this section only some representative processes are presented to reveal the typical governing mechanisms of the surface integrity generation in hybrid machining.

6.2.1. *Thermal assisted machining: combining mechanical and thermal effects*

Thermal assisted machining (TAM) is usually applied to process difficult-to-cut materials like superalloys, where the added heat source (e.g. laser, plasma and induction) provides a softening effect to the material, thus increasing the machinability [32]. However, due to the thermal nature, the machined workpiece is subjected to combined effects of thermal and mechanical loading. Although the preheating effect may soften or even melt the material, significantly altering the material (Fig. 48 (a)), in most investigations better surface finishes were generated from TAM (Fig. 48 (c)), compared with conventional processing (Fig. 48 (b)) [125]. This is because the thermal softening effect makes the material more prone to deformation and easier to be removed, hence

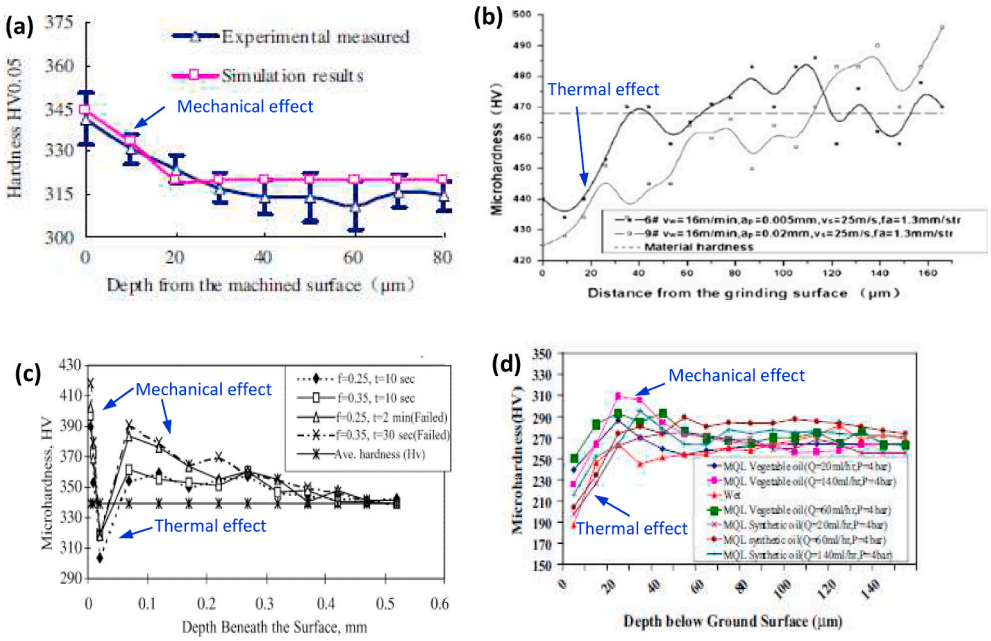

Fig. 45. Micro-hardness as a function of depth showing (a) hardening effect (mechanical loading) [90], (b) softening effect (thermal loading) [299], (c) mechanical predominated [300] and (d) thermal predominated combined (thermal & mechanical) effect [301] in machining of high strength alloy under different cutting conditions.

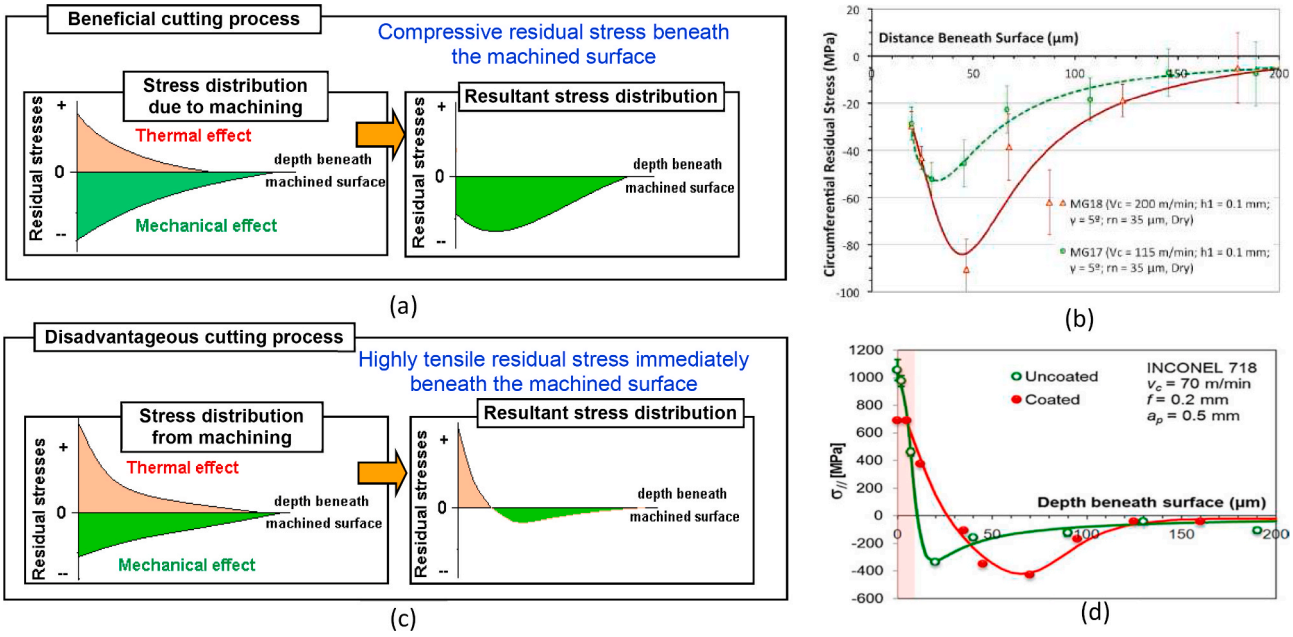

Fig. 46. Combined effect of residual stress from thermal and mechanical effects: (a) and (b) mechanical effect dominated [302], (c) and (d) thermal effect dominated [303], (a and c are modified from Ref. [304]).

a smoother surface can be achieved. Nevertheless, although TAM has shown in some instances better metallurgical structures, it also generates higher tensile residual stresses (Fig. 48 (f)) than conventional machining (Fig. 48 (e)), due to the high thermal influence (Fig. 48 (d)). This deteriorates fatigue performance, hence post processing is necessary to introduce compressive residual stresses to facilitate the increase in the fatigue life of the laser assisted machined components.

6.2.2. Waterjet-assisted laser machining: combining thermal and mechanical effects

Heat-related metallurgical defects induced in the workpiece are often caused by long pulse lasers, i.e. nanosecond, microsecond, millisecond or continuous-wave lasers (Section 4.1). One way to address this is by reducing heat transfer to the substrate by employing wet ablation [305], and waterjet-assisted laser machining. Here, water is used to cool and remove material, which can improve surface integrity by removing recast and spatter from machined regions. Y.Z. Liu showed significant improvements in surface quality associated with waterjet-assisted laser drilling [306]. The authors reported the absence of oxide layers, recast layer, HAZ, and phase transformations around the cooling hole. These defects are typical for nanosecond laser drilling. Studies by Zhu et al. [307] demonstrated material removal of Ge in solid state when high

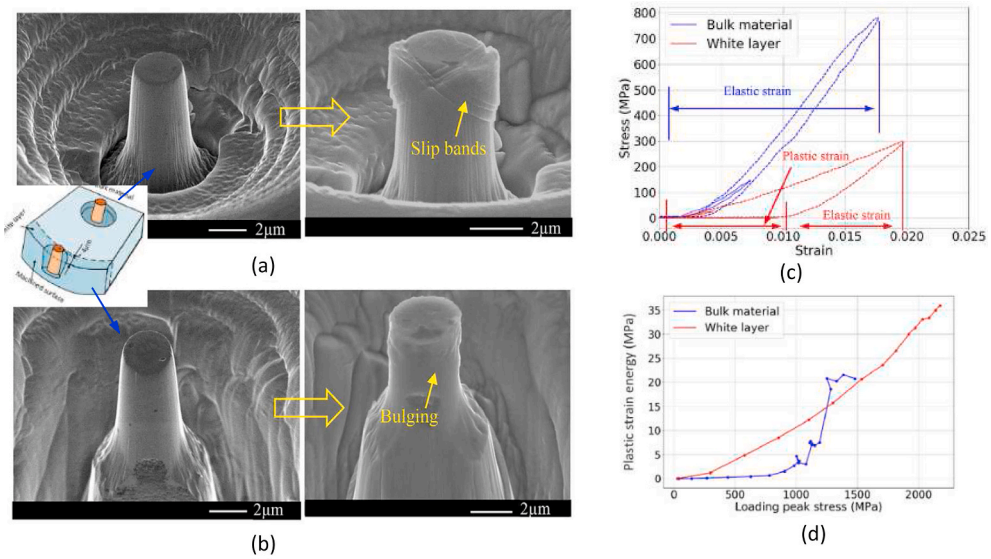

Fig. 47. Micromechanics of thermo-mechanical induced white layer: micropillar in (a) bulk material and (b) white layer, (c) stress-strain curve and (d) plastic strain energy [65].

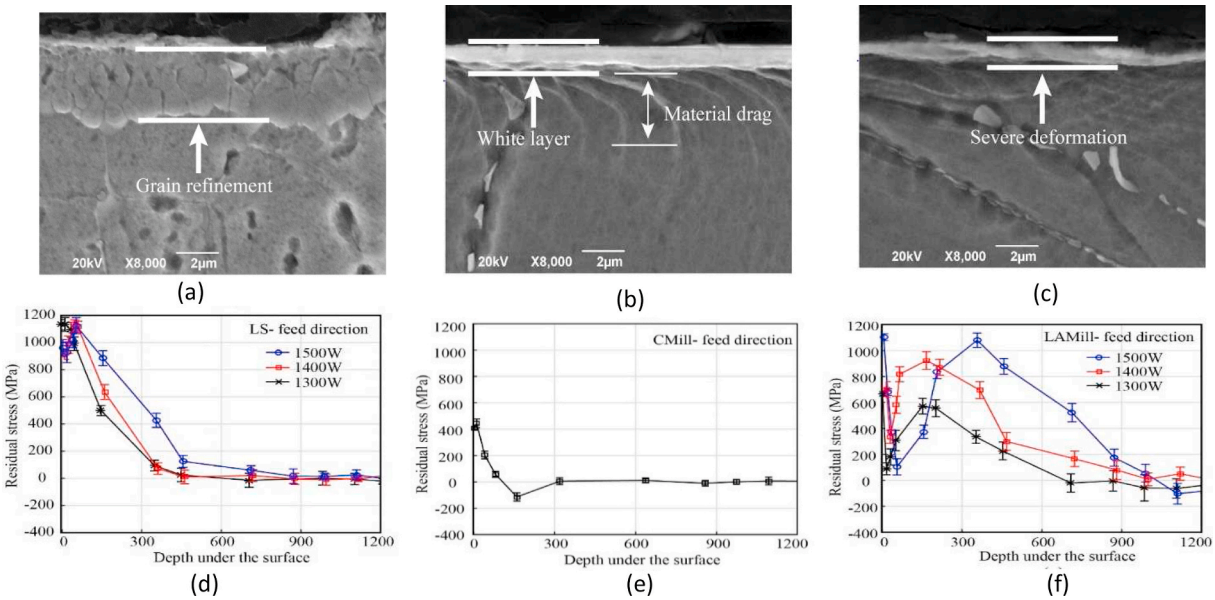

Fig. 48. Surface damage and residual stress of (a) and (d) laser heating only, (b) and (e) conventional machining, (c) and (f) laser assisted machining of Inconel 718 [125].

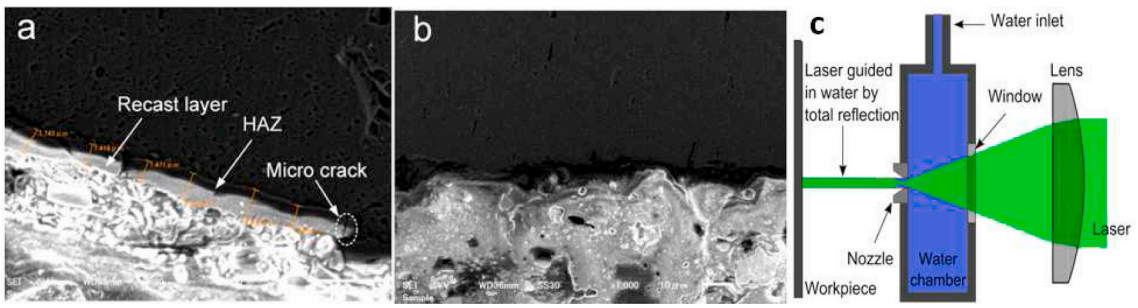

Fig. 49. A comparison of the machined area on aluminium alloy workpiece by (a) laser micromachining in the air; (b)processed by waterjet-assisted laser micro-machining [310]. (c) Typical setup for hybrid laser-waterjet machining [306].

water pressures (6 MPa) were used. Total internal reflection of lasers in water jets was used by Adelmann et al. [306] and Wang et al. [308], where a water jet guided laser beam (Fig. 49) does not deflect and is capable of cutting metals with lower taper angles and higher aspect ratios, while increasing process efficiency [309,310].

6.2.3. Electrochemical discharge machining (ECDM): combining chemical and thermal effects

In ECDM, material removal takes place due to the combined effects of an electrochemical reaction and electrical discharges. In this system, there are two electrodes, creating an electrochemical cell, as well as the workpiece. The electrochemical action generates hydrogen at the cathode. The action of the electrical discharge occurs between the tool and workpiece due to the breakdown of the insulating layer of gas bubbles. The process can be used for machining metals like steel [311] and non-conductive materials including glasses [312]. A schematic of the ECDM setup and mechanism is shown in Fig. 50, adapted from Ref. [313].

Because the ECDM mechanism involves discharges, recast layers on ECDM-processed materials are produced. Images of an ECDM discharge compared to a normal EDM discharge, along with an ECDM surface, are shown in Fig. 50 for a Ni-based superalloy. In the crater in (Fig. 50 (b)) and on the surface in Fig. 50 (d), spalling, as well as melting/vaporisation occur as key material removal mechanisms [59]. Based on this, it is believed that the overall removal mechanisms between EDM and ECDM are similar. The dominance of the discharge mechanism results in cracking in the recast layer. However, evidence for reduced energy of the ECDM spark was seen, compared to EDM, indicating that the recast layer thickness is lower for ECDM. Evidence of an almost eliminated recast layer in the case of ECDM has been shown compared with EDM [314], shown in Fig. 50 (e). It is proposed that the recast layer and its associated defects are removed by electrolysis during the hybrid process. However, this must be sequential as it is not possible for EDM and ECM to occur concurrently at a local level.

6.2.4. Electrochemical grinding (ECG): combining chemical and mechanical effects

Electrochemical grinding (ECG) is a hybrid of ECM and mechanical grinding. In this process, ECM dissolves the anode workpiece at high speed, using a high current density. Electrolysis products adhering to the machined surface are removed by grinding [315]. This hybrid approach can yield better surface finishes, higher material removal rates, and better accuracy than grinding processes [316]. In addition, most of the oxide/passivation layer is removed by grinding, and this is thought to be 5–10% of material removal [317]. This avoids the need for aggressive electrolytes to dissolve this layer. Slight practical variations of the ECG process exist (Fig. 51), including inner-jet electrochemical mill-grinding and electrochemical deep grinding.

The ability of ECG to produce high integrity surfaces has been demonstrated [23], with electrochemical deep grinding. The enhanced surface finished on a Ni-based superalloy compared to both conventional grinding and ECM is shown in Fig. 51. When ECM is added to a conventional “deep grinding” process, the removal mechanism of the workpiece (anode) changes significantly [23] with the generation of ECM precipitates and adhered electrolytic products (Fig. 52). When the gap between electrode and workpiece is larger than the height of the abrasive particles protruding from the tool, material removal is primarily from ECM. When the gap is reduced to less than the height of the abrasives, surface quality deteriorates due to the dominance of mechanical removal. Adjusting this parameter can yield good surface finishes with the ECM process dominating the final material removal process.

7. Post-machining processing to improve surface integrity after machining

In high-value manufacturing, it is widely recognised that surface integrity has to be controlled by adopting conservative machining parameters that inherently yield reduced material removal rates. Hence, high surface integrity and low manufacturing cost is usually a contradiction.

As surface defects usually occur at high material removal rate cutting conditions, post/secondary processes are normally applied to remove/modify surface damage layers. This can be achieved through fine machining (finishing and polishing) or etching, to remove damaged layers, or through post-processing methods such as (shot, laser shock) peening, blasting and burnishing to enhance the quality of the machined superficial layers [319]. This enables manufacturers to exploit productivity benefits of high material removal rate machining, while achieving good surface integrity.

7.1. Mechanical post processing

Generally, finishing processes are cost effective routes to remove surface defects [320]. This is because, based on controlling the optimal material removal value [321], some finishing processes not only remove damaged surface layers, but also introduce surface strengthening effects (e.g. introducing compressive residual stresses) [322]. In this case, there is a need to understand the relationship and interaction between the primary and secondary processes. Herbert et al. [121] reported that while a layer of surface damage up to 20 μm was introduced by the roughing process, a 25 μm depth finishing cut can remove the white layer effectively (Fig. 53 (a)) and maintain a compressive stress (Fig. 53 (b)).

Grinding followed by polishing is also commonly used to remove surface damage, especially after thermal machining (e.g. LBM, EDM),

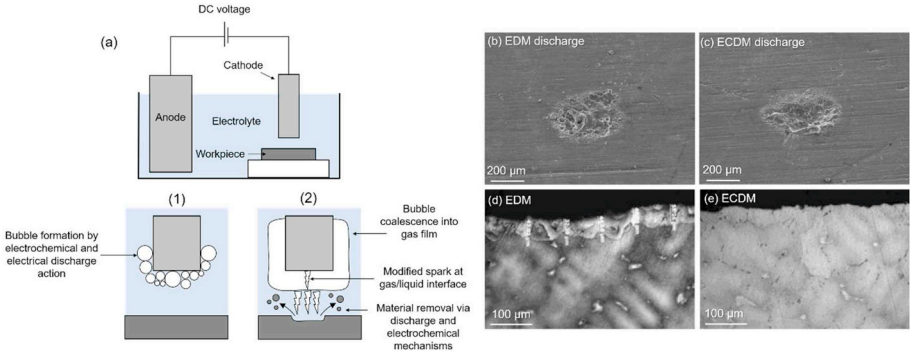

Fig. 50. (a) Schematic of ECDM setup and removal mechanism and discharge produced using (b) ECDM with an electrolyte and (c) using EDM with an emulsion, under identical parameters [59]. (d) and (e) compare a recast layer produced by EDM of a nickel-base superalloy to that machined by a tube based electrochemical discharge method.

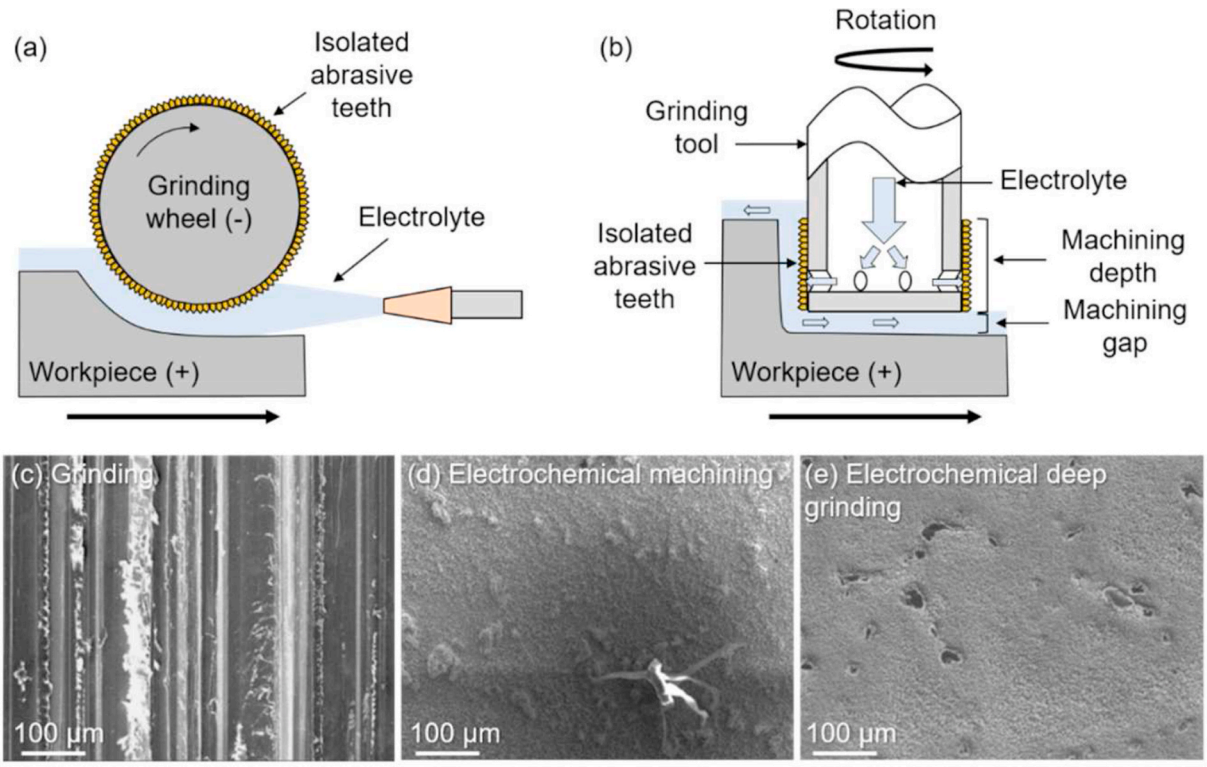

Fig. 51. Schematics of (a) electrochemical grinding and (b) inner-jet electrochemical mill-grinding (adapted from Ref. [318]), and (c)–(e) A comparison of surface morphologies produced by electrochemical deep grinding compared to conventional mechanical grinding and electrochemical machining [23].

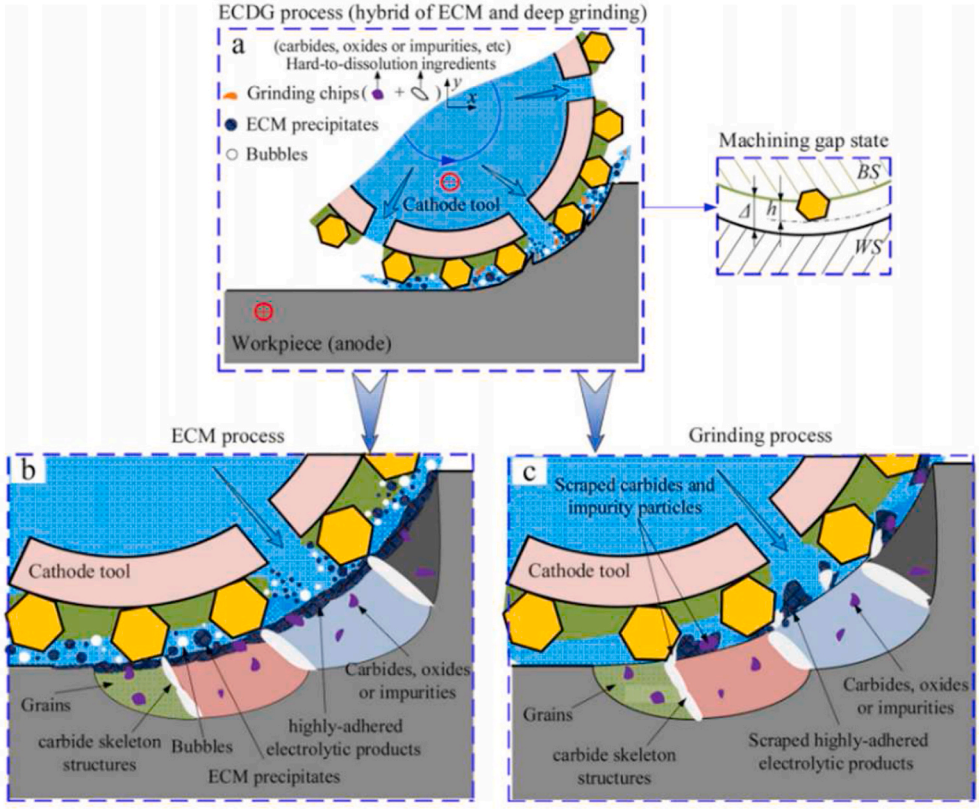

Fig. 52. Schematic of removal mechanism in electrochemical deep grinding [23].

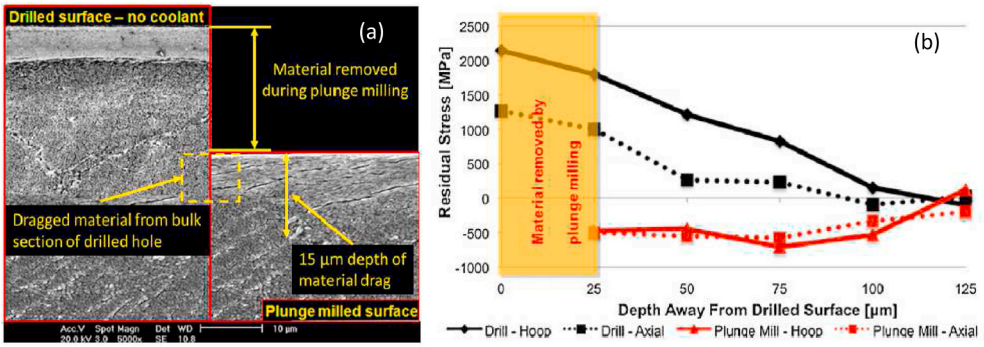

Fig. 53. (a) SEM micrographs (hoop direction) of nickel based alloy after abusive drilling (left) and plunge milling (right) to illustrate sections removed by subsequent finishing operation, (b) the corresponding residual stresses [121].

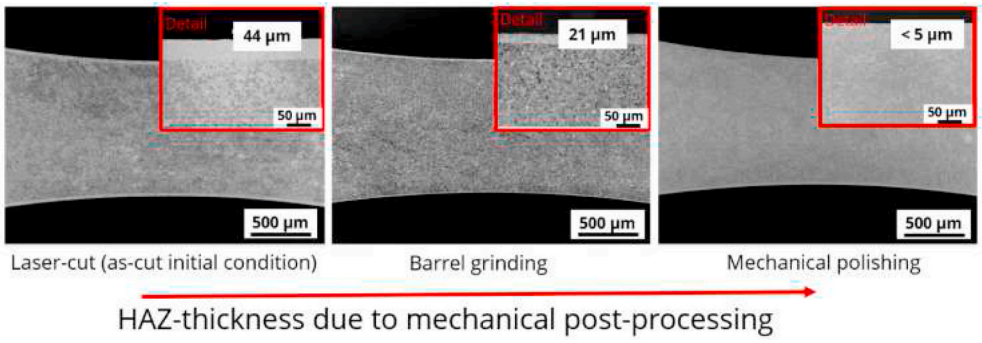

Fig. 54. Thickness of the HAZ dependent on the mechanical post-processing showing a significant decrease in measured HAZ-thickness at the upper cutting edge [171].

where damaged layers are much thinner compared to mechanical machining. As shown in Fig. 54 (laser cut Ti–6Al–4V), post barrel grinding and mechanical polishing can effectively remove heat affected zones resulting from laser heating [171].

When unwanted high tensile residual stresses are present on the machined surface, post processing through mechanical surface

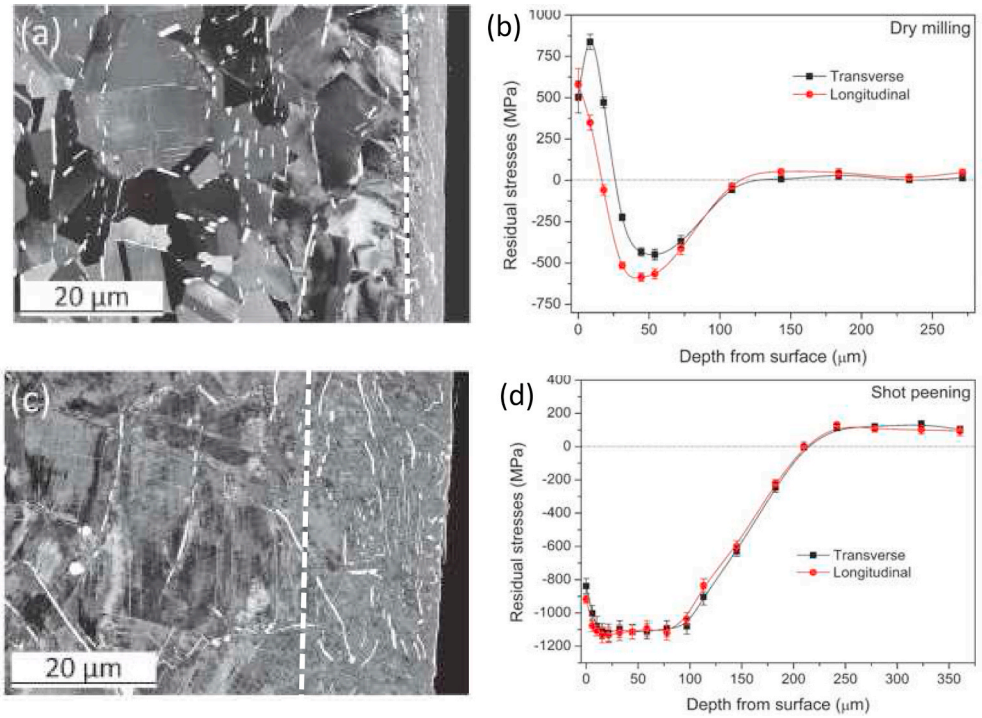

Fig. 55. (a) Electron channelling contrast imaging (ECCI) micrographs and (b) residual stress of the dry-milled surface on Inconel 718, (c) and (d) corresponded shot peening process [323].

modification can enhance surface integrity, i.e. introducing compressive residual stress. This can be achieved through peening methods, including shot peening, laser shock peening, water jet peening, and blasting processes. By introducing a high plastic deformation layer, these processes can generate high compressive residual stresses on the machined surface, retarding surface cracking. It is important to note that while these processes can also generate white layers [323], shown in Fig. 55, these are induced solely by mechanical mechanisms through deformation of the original grains. This is similar to the grain refinement mechanism in Fig. 12 of M-WL, introducing work hardening without significant thermal influence, generating compressive stresses.

This hardening mechanism has been explained through micro-pillar compression tests over the residual cross-section, shown in Fig. 56. A gradient change in grain morphology including the fine grain zone, transition zone and bulk material is shown, similar to white layers in conventional machining. An increase of three times the yield stress has been achieved in the near-surface layer (fine grain zone) compared with bulk regions. In this case, Hall-Petch (grain refinement) effects appear to be the predominant strengthening mechanism in the fine grain zone, while dislocation hardening is the main strengthening mechanism in the transition layer.

7.2. Energy beam irradiation post processing

Energy beam irradiation and polishing techniques have generated research interest as they offer non-contact, selective/non-selective and automated surface modification approaches [324]. In addition, mechanical properties of the near-surface are often improved. Energy beam processes have an advantage over traditional mechanical finishing processes to work effectively, given their ability to operate is unaffected by the mechanical properties of the part to be finished, in particular: hardness, brittleness, and wear resistance. There are several beam irradiation processes, which are useful for modifying a variety of machined surfaces which are discussed in this section, including: laser beams, electron beams, ion beams and plasma beams.

7.2.1. Laser beam

Laser beam polishing is a commonly used beam process for component finishing. The laser beam irradiates the workpiece surface, yielding a shallow melt pool, and melting surfaces at macro (20–200 μm), or micro (0.5–5 μm) depths [325]. The generated melt pool melts surface asperities, which flow into adjacent troughs on the surface. The process mechanism, and an example of the polishing effect are shown in Fig. 57 (a) and (b) [326].

Multidirectional surface tensile effects tend to redistribute material around discrete surface asperities [326]. This results in the reduction of surface peak-to-valley heights. As the range of depths that can be melted by laser beam irradiation matches typical depths of machining-induced damage, laser polishing has found wide application in post-processing machined surfaces. An example of the effect of laser polishing on both EDM processed, and mechanically milled surfaces, is shown in Fig. 57 (c)–(e). This study focused on surface finish [326], and it was shown that >90% reduction in *Ra* surface roughness is achievable by laser polishing of both EDM and milled surfaces, with the correct laser fluence. To avoid melting material volumes larger than the surface defects, pulsed laser micro-polishing can be used. In this setup, the sample surface is irradiated with pulses (100s of ns), resulting in a melting depth on the order of 10–100 nm [328]. On milled Ti–6Al–4V, *Ra* roughness could be reduced from 0.206 to 0.070 μm [328]. On many metals, laser polishing can increase the near-surface hardness. For example, in laser polishing of end-milled Ti-6al-4V, a 25% increase in micro-hardness was measured after polishing, caused by martensite formation [329]. In addition, the roughness was reduced by over 90% (from 7.3 μm to 0.6 μm *Ra)* in the same study. Some evidence of an improvement in corrosion resistance was also seen, which may be explained by a combination of improved surface finish and the change in phase structure.

7.2.2. Electron beam

High current pulsed electron beam (HCPEB) irradiation is a more niche technique than laser beam polishing, and a relatively new addition to the array of available surface modification techniques. The process uses short (μs) pulses, or shots, of high current electrons over large areas (e.g. 60 mm diameter) to rapidly melt surfaces, improving finish and some mechanical and chemical properties. A schematic showing the irradiation process mechanism given in Fig. 58.

HCPEB is particularly useful for improving machined surface integrity, especially that produced by thermal machining. This is because the process can mitigate many of the negative features produced by laser and EDM machining, such as porosity, excessive roughness and poor morphology, and in some case cracking. The near surface is typically fully melted by the irradiation process; the extent of this depends on the melting point of the material. Typically, melt depths are approximately

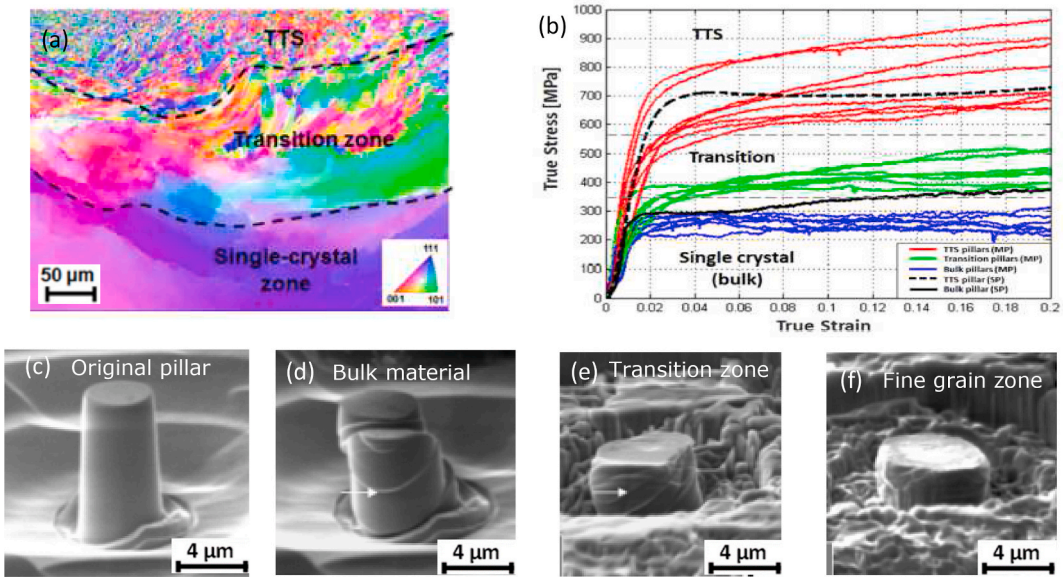

Fig. 56. Micromechanical testing reveals the strengthening effect of shot peeing: (a) Crystallography, (b) stress-strain curve, and micropillars (c) before and (d)–(f) after compression [56].

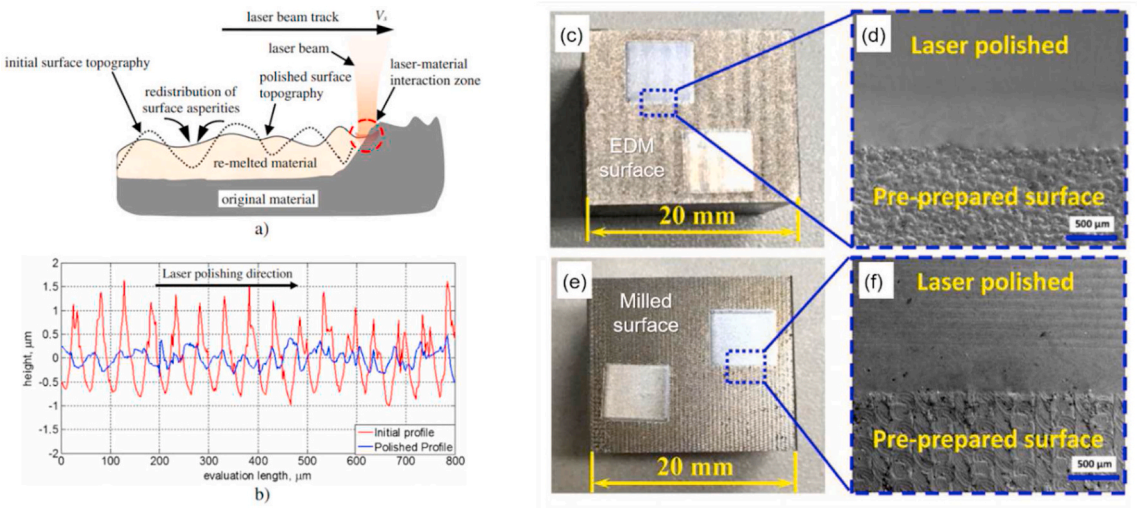

Fig. 57. (a) A schematic showing the melting and smoothing process caused by laser polishing/melting, and (b) surface profiles showing the effect of the process on asperity reduction [326], and examples of the effect of laser polishing on (c) and (d) EDM surfaces and (e) and (f) mechanically milled surfaces, from Dai et al. [327].

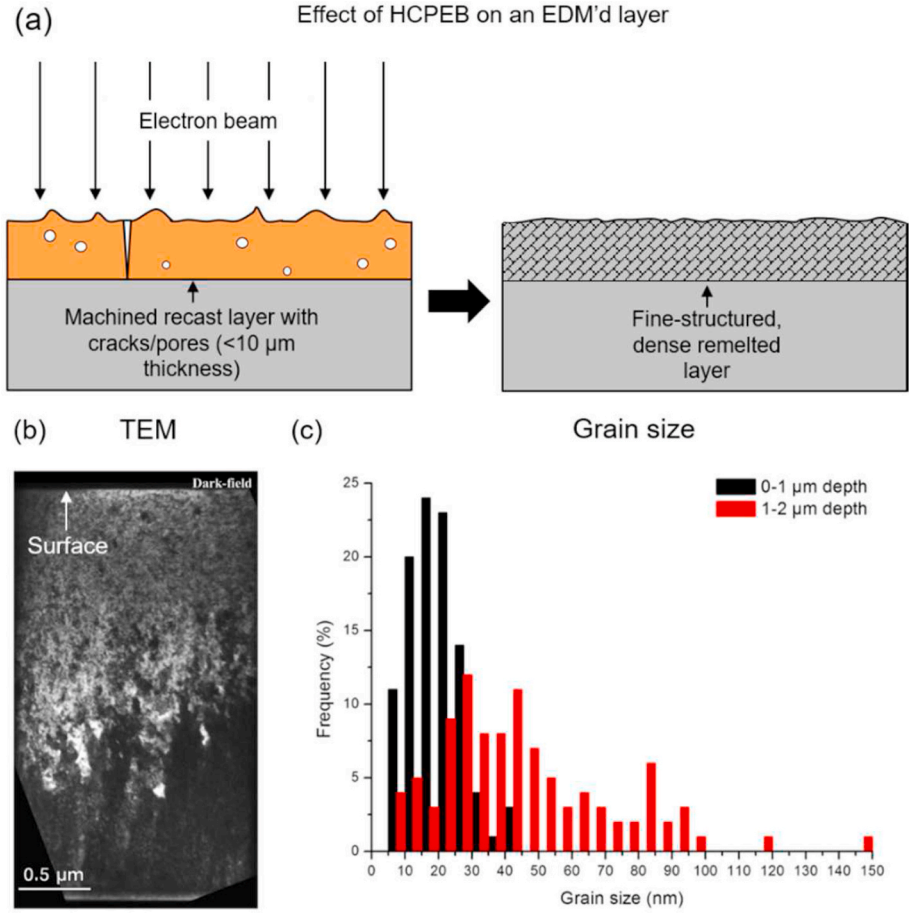

Fig. 58. (a) Schematic showing the effect of large-area electron beam irradiation on a machined surface such as that cut by EDM. (b) cross-sectional TEM image of a steel subject to HCPEB and (c) resultant nano-sized grain sizes from this area [105].

5 μm but can be as high as 10 μm. Fig. 58 shows the effect of irradiation on an EDM processed surface, demonstrating smoothing as well as porosity and crack elimination. The key advantage of this surface modification process over laser techniques is the uniformity of the energy density of the beam over areas approximately 60 mm diameter [330]. This is combined with the process ability to modify surfaces with equal effect at angles highly acute to the primary beam direction [330], therefore allowing treatment of conformal surfaces. Since melting of the surface with uniform energy density across the irradiation area occurs during pulsed electron beam treatment, the process is attractive for its potential to improve surface morphology of EDM surfaces, in particular elimination of surface cracking. HCPEB has been used to modify surface

properties of several engineering alloys, such as Ti-alloys and steels. For example, mild steel subjected to EDM was treated by Uno et al. [330, 331], where surface roughness was reduced and evidence of improved corrosion behaviour was shown. Okada et al. [332] also demonstrated that surface defects created by the EDM process could be reduced by 75% approximately (60 μm–15 μm height) by applying HCPEB, eliminating many smaller asperities. Murray et al. [333] investigated the effect of HCPEB on the surface crack density of stainless steel machined by EDM. At appropriate parameters, surface melting eliminated cracks. In cross-section, it was observed that a homogenous 4 μm layer of melted, crack free material was produced. A unique surface-tension based mechanism was found to be responsible for this reparation effect. Considering there is no direct mechanical force exerted on the workpiece, the process can be used to treat intricate components, where most surface finishing methods are impossible.

7.2.3. Ion beam

Ion beam polishing methods applied on metallic surfaces include both low-energy (~2 keV [334]) and high-energy (~200 keV [335]) beam types. Ion beam polishing is also referred to as ion beam etching or ion beam milling. Low-energy ion beam polishing does not generate heat, and therefore is different in principle to laser and electron-based methods [336]. Low-energy ion beam polishing exploits elastic collisions between incident ions and the atomic nuclei of the surface layer, transferring kinetic energy and resulting in sputtering of atoms from the workpiece surface [337]. The mechanism of removal in ion beam polishing depends on increasing the internal energy of individual atoms. For an atom to be removed from the lattice, its internal energy must be increased beyond the Helmholtz free energy at the material surface, and this is achieved by supply kinetic energy through ion bombardment [338]. The energy required for removal must exceed the sum of the lattice bonding energy and the surface barrier energy. Ion beam polishing has been demonstrated at an accuracy at sub-nm scale [339]. However, given the low efficiency of the ion beam polishing process, such low-energy high accuracy polishing may not be practical. Mechanically finished Ti–6Al–4V at a roughness of an average of ~0.2 μm was finished with high current ion beam polishing [340]. Despite the already polished surface prior, a roughness of 53 nm *Ra* average was produced after ion beam polishing (60 min) (Fig. 59).

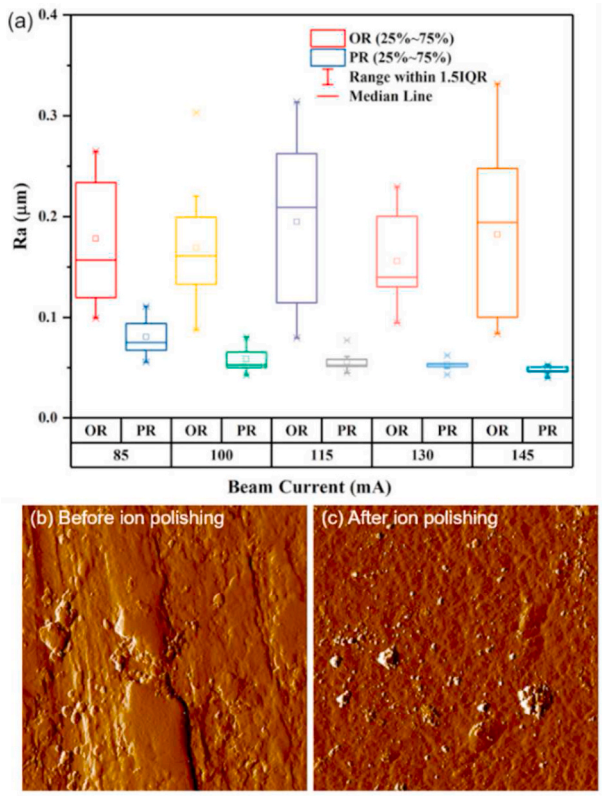

Fig. 59. (a) *Ra* roughness of mechanically finished Ti–6Al–4V before and after ion finishing at various beam currents. (b) and (c) show before and after AFM images of the surface topography [340].

7.2.4. Plasma beam

Atmospheric pressure plasma beam is a relatively new (from 2015 [341]), simple method for finishing of machined surfaces, and an innovation from gas shielded arc welding. The process utilises a high voltage and small current to generate a discharge plasma at atmospheric pressure, between the positive electrode and the negative workpiece surface. In this process, the plasma preferentially melts peaks on the workpiece surface, ultimately smoothing the surface [336]. Dai et al. used a small scale atmospheric plasma irradiation setup to substantially improve the surface morphology of cast iron [341], images shown in Fig. 60. This process is promising for the non location specific treatment of metal surfaces for surface peak and contamination removal, and therefore should be the subject of future research and application for the field of surface modification in machining.

7.3. Chemical and electrochemical post processing

Chemical and electrochemical finishing, such as electropolishing (EP) and chemopolishing (CP), are widely applied to metals to remove machining surface defects, by smoothing topographies, removing oxide scale and other surface impurities, and removing microstructurally affected layers. Such finishing can reduce the surface occurrence of fatigue point initiators, improve corrosion resistance, and eliminate residual stresses arising from prior processing.

EP shares the same fundamental process physics and chemistry as ECM, discussed in Section 5, involving the anodic dissolution of the workpiece material (oxidation reaction), which is proportional to the charge passed. The difference is mainly one of parameter and electrolyte selection, the goal being surface-defect removal rather than bulk material removal, for example improving topographical aspects of recast layers after EDM [342]. In most cases, EP is performed in a viscous acidic electrolytic media, such as solutions of H_2SO_4 and H_3PO_4 [5,271]. High viscosities and low flow rates promote the generation of a mass transport-limited polishing film (Fig. 37 (d)), while the acidity retains the solubility of metal cations by preventing hydroxide-type sludge formation. Due to reduced flow rate conditions, which cannot sufficiently evacuate generated oxygen from the anode surface, EP is performed at lower potentials than ECM, avoiding the transpassive dissolution regime that results in greater material removal and concurrent oxygen evolution. The generation of a mass transport-limited polishing film is essential for anodic brightening and is signalled by the current-limiting plateau (Fig. 61 (a)). The process is dependent on the applied potential, the workpiece material, electrolyte composition and temperature, and flow conditions. As such, EP has a high degree of adaptability and can successfully finish most relevant load-bearing engineering materials, such as steels, Ni-superalloys, Ti-alloys, and Al-alloys. The process is limited by the ability to position the cathode relative to the workpiece, so EP is challenging for large complex parts with interior geometries.

Unlike EP, CP methods are not limited by cathode positioning, as the polishing reaction does not always require applied current, electrochemical pickling methods being the exception. CP and other chemical pickling methods are applied to materials that are machined at high temperature, or in parts where oxide scale, surface defects, and impurities can become embedded and certain elements are depleted during manufacturing [343]. These can present significant problems when affected materials are applied to pressurised and chemically aggressive environments. In CP and pickling, the finishing mechanism can occur

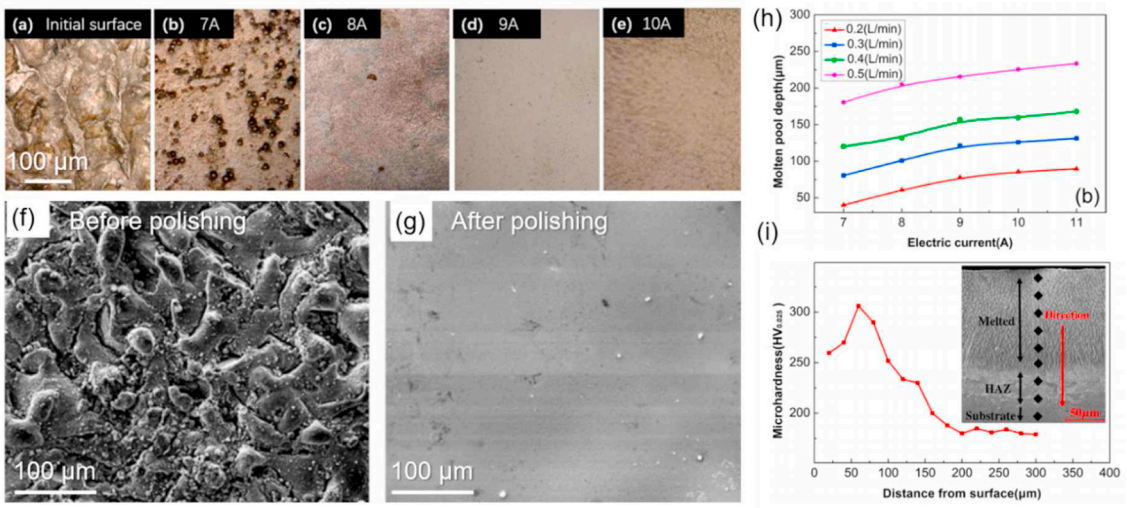

Fig. 60. Surface finishing of (a–e) ground steel, and (f–g) cast iron by micro atmospheric plasma beam, (h) effect of current on melt pool depth and (i) changed in cross-sectional hardness from (a–e).

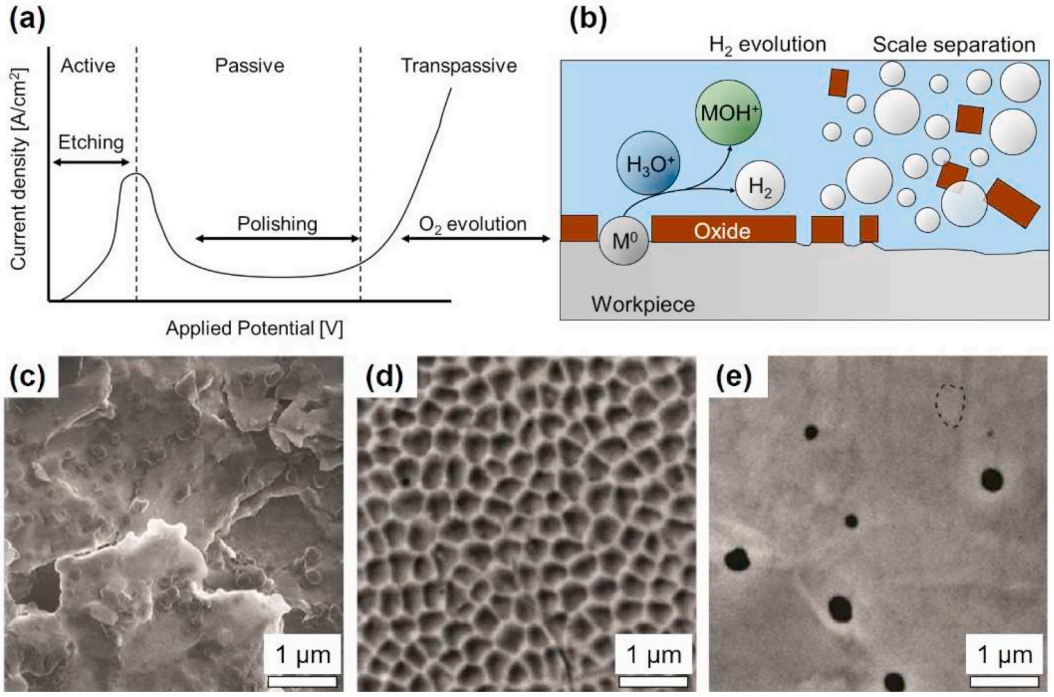

Fig. 61. Typical anodic potential sweep for a metal in EP electrolyte, redrawn from Han et al. [5]. EP is performed at the limiting current plateau, operation in the transpassive region leads to O_2 evolution and surface deterioration. (b) Acid-bath CP and pickling often relies base metal dissolution to remove oxide scale. (c) Unfinished sample of steel 316, (d) after CP and (e) after EP. Taken from Tyagi et al. [346].

either through a reduction or oxidation reaction [344]. In most cases, the part is dipped in an acid bath, to provide an aggressive chemical environment. This can reduce or oxidise impurities, depending on the acid used, with the aim of increasing the solubility of the impurity species, while hydrogen gas is evolved at the workpiece, stirring the solution and flaking scale by separation (Fig. 61 (b)). Where the near-surface metallurgy and local compositions are altered, for example in high-temperature machining processes, failure modes like corrosion and fatigue can be enabled [345]. For example Cr, which is incorporated into many load-bearing alloys to improve corrosion resistance often forms carbide precipitates at high temperatures, locally depleting surface layers of solid-solution Cr. CP can remove these element-depleted layers, as the solution will preferentially attack the base material, for example Fe in steel. However, CP methods evolving hydrogen gas at the workpiece require high levels of control as they can lead to hydrogen embrittlement. In anodic pickling, the surface is passivated and oxygen gas is evolved from the part, which can flake scales resulting from machining, but the process is slower. Combinations of CP and EP processes can also be applied concurrently to finish parts with interior surfaces (Fig. 61 (c)–(e)) [346].

8. Conclusions and research opportunities

This review provides an assessment of fundamental aspects of surface integrity in the context of metal machining with special focus on recent advances in experimental characterisation methods and their

application to investigate the characteristics of machined surfaces and related subsurface defects. Thanks to the rapid development of analytical methods for material characterisation (e.g. FIB-SEM, HR-TEM, EBSD, X-ray spectroscopy etc.) and their broader application in recent years in the machining research community, significant progress has been made in understanding the impact of machining process effects on microstructure alteration and related surface generation mechanisms. The main conclusions of this review are as follows:

- As the understanding of machining-induced material modifications progresses, a pivotal role is played by the possibility of in-depth analysis of the workpiece subsurface condition, continuously introducing evolving surface integrity metrics on ever smaller scales. Hence, further growth is expected within the development of cutting-edge surface integrity characterisation approaches, both from a microstructural and micromechanical perspective, thus revealing unique insights into the fundamental mechanisms (e.g. mechanical, thermal, chemical effects and their combination) governing surface generation in metal machining.
- The mechanical effects from conventional machining can lead to severe plastic deformation of the metal workpieces yielding highly deformed grain structure, severe work hardening and even result in ultrafine grain refinement under aggressive cutting conditions. The presence of machining-induced subsurface defects such as microcracks, plucking, surface tearing, material re-deposition and debris are also concerns which can deteriorate workpiece functional performance. Waterjet machining can lead to scratching and chipping, abrasive embedment, striations when machining ductile materials while the main surface defect is crack damage when machining brittle materials.
- In thermal machining (e.g. laser machining and EDM) many heat affected phenomena can occur due to the nature of the material removal mechanism. Over the last few decades, the thermal effect on the workpiece has been steadily decreasing by virtue of the development of short and ultrashort pulse lasers, thus allowing the achievement of high-quality surfaces. Such lasers, when finely tuned for a given material, present a unique tool for fine material processing and finishing. Finding a way to increase process efficiency while keeping a high degree of surface integrity will be advantageous for future research of LBM. In EDM, porosity, cracking, high surface roughness, carbon uptake and phase transformation all can have a major impact on the functional properties of EDM parts, including fatigue, wear and corrosion resistance. However the substantial research base has allowed several technologies to help mitigate these factors – these include powder-mixed EDM in which spark energy density and distribution is altered to reduce the severity of the material changes associated with the formation of recast layers.
- In chemical/electrochemical machining, while a high degree of surface integrity can be established in most materials with appropriate parameter selection, control over surface integrity is challenging when machining highly passivating alloys and complex materials systems with multiple discrete phases, such as next-generation metal matrix composites. Future ECM research will benefit from applying non-aqueous electrolytes to overcome passivation effects and the application of additional energy sources in hybrid machining methods to enable the machining of electrochemically inert phases.
- The combination of different mechanisms can be manifested in single processes (e.g. conventional machining under aggressive cutting conditions), and also in hybrid machining processes, e.g. laser assisted machining (LAM), and electrochemical discharge machining (ECDM). The former scenario normally combines the mechanical and thermal effect in which case both thermally and mechanically induced white layers can be generated. In the latter scenario although a combination of different material removal mechanisms is introduced, normally improved surface integrity can be achieved due to the improvement in machinability.
- A range of methods exist for mitigating the negative effects of machining processes on surface integrity. These include mechanical, beam based, and chemical methods. Indeed, opportunities exist with machining processes themselves to tailor surface properties to be favourable. These processes have different limitations, including part/surface geometry and depth of affected zone, however each of these offers different benefits to morphology and functional properties. This means that with the correct process chain selection, machined components are not sentenced to have application-limiting poor surface integrity, but can in fact be enhanced for application specific purposes.

It is expected that the fundamental knowledge obtained from the in-depth analysis of machining-induced subsurface layers (down to the nm scale) should open new possibilities for the research community to develop better physical models to predict surface integrity and its impact on the functional performance of a machined component. One of the major challenges that remains however, is the translation of this knowledge from a laboratory/research environment to industrial settings. In the latter, it is anticipated that research efforts will also be needed to develop robust methods for non-destructive testing and surface integrity inspection that could be deployed directly on a machined component e.g. in the same way as it has been developed for on-machine probing in the context of in-process metrology of complex machined surfaces. Hence, the possibility of introducing surface-integrity-oriented approaches at all levels of the production chain (i.e. from the product design stage to shop floor operations)is a key direction for future research and development of this field, with likely impact on the sustainability and cost-efficiency of future machining operations, as well as optimisation of the functional performance of next-generation machined parts.

CRediT author statement

Zhirong Liao: Conceptualization; Methodology; Writing – original draft, Review & Editing, **Andrea la Monaca:** Methodology; Writing – original draft, Review & Editing, **James Murray:** Methodology; Writing – original draft, Review & Editing, **Alistair Speidel:** Methodology; Writing – original draft, Review & Editing, **Dmitrii Ushmaev:** Methodology; Writing – original draft, **Adam Clare:** Methodology; Writing – original draft, Review & Editing, **Dragos Axinte:** Conceptualization; Supervision; Reviewing and Editing, **Rachid M'Saoubi:** Writing – original draft, Review & Editing

Declaration of competing interest

The authors declare that they have no known competing financial interests or personal relationships that could have appeared to influence the work reported in this paper.

Acknowledgement

This study was supported by EPSRC through the DTP 2018–19 University of Nottingham (No: EP/R513283/1), NanoPrime (No: EP/R025282/1) and Rolls-Royce CASE award scheme (No: 19000151). The authors would like to thank the support from and Nottingham research fellowship programme as well.

References

[1] Q. Liu, Z. Liao, D. Axinte, Temperature effect on the material removal mechanism of soft-brittle crystals at nano/micron scale, Int. J. Mach. Tool Manufact. (2020) 103620.

[2] O.G. Diaz, G.G. Luna, Z. Liao, D. Axinte, The new challenges of machining Ceramic Matrix Composites (CMCs): review of surface integrity, Int. J. Mach. Tool Manufact. (2019).

[3] Z. Liao, A. Abdelhafeez, H. Li, Y. Yang, O.G. Diaz, D. Axinte, State-of-the-art of surface integrity in machining of metal matrix composites, Int. J. Mach. Tool Manufact. 143 (2019) 63–91.

[4] S. Zhan, Y. Zhao, Plasma-assisted electrochemical machining of microtools and microstructures, Int. J. Mach. Tool Manufact. (2020), https://doi.org/10.1016/j.ijmachtools.2020.103596.

[5] W. Han, F. Fang, Fundamental aspects and recent developments in electropolishing, Int. J. Mach. Tool Manufact. (2019).

[6] Y.Z. Liu, Coaxial waterjet-assisted laser drilling of film cooling holes in turbine blades, Int. J. Mach. Tool Manufact. (2019) 103510.

[7] X. Han, D. Xu, D. Axinte, Z. Liao, H.N. Li, On understanding the specific cutting mechanisms governing the workpiece surface integrity in metal matrix composites machining, J. Mater. Process. Technol. 288 (2020) 116875.

[8] C. Li, X. Li, Y. Wu, F. Zhang, H. Huang, Deformation mechanism and force modelling of the grinding of YAG single crystals, Int. J. Mach. Tool Manufact. 143 (2019) 23–37.

[9] G. Chen, C. Ren, Y. Zou, X. Qin, L. Lu, S. Li, Mechanism for material removal in ultrasonic vibration helical milling of Ti–6Al–4V alloy, Int. J. Mach. Tool Manufact. (2019), https://doi.org/10.1016/j.ijmachtools.2018.11.001.

[10] H. Yang, W. Ding, Y. Chen, S. Laporte, J. Xu, Y. Fu, Drilling force model for forced low frequency vibration assisted drilling of Ti-6Al-4V titanium alloy, Int. J. Mach. Tool Manufact. (2019), https://doi.org/10.1016/j.ijmachtools.2019.103438.

[11] R. Aigner, S. Pusterhofer, S. Pomberger, M. Leitner, M. Stoschka, A probabilistic Kitagawa-Takahashi diagram for fatigue strength assessment of cast aluminium alloys, Mater. Sci. Eng., A (2019), https://doi.org/10.1016/j.msea.2018.12.108.

[12] A. Cox, S. Herbert, J.P. Villain-Chastre, S. Turner, M. Jackson, The effect of machining and induced surface deformation on the fatigue performance of a high strength metastable β titanium alloy, Int. J. Fatig. 124 (2019) 26–33, https://doi.org/10.1016/j.ijfatigue.2019.02.033.

[13] C. Herbert, D.A. Axinte, M. Hardy, P. Withers, Influence of surface anomalies following hole making operations on the fatigue performance for a nickel-based superalloy, J. Manuf. Sci. Eng. 136 (2014) 51016.

[14] P. Jia, Y. Rong, Y. Huang, Condition monitoring of the feed drive system of a machine tool based on long-term operational modal analysis, Int. J. Mach. Tool Manufact. (2019), 103454, https://doi.org/10.1016/j.ijmachtools.2019.103454.

[15] D. Gao, Z. Liao, Z. Lv, Y. Lu, Multi-scale statistical signal processing of cutting force in cutting tool condition monitoring, Int. J. Adv. Manuf. Technol. 80 (2015) 1843–1853.

[16] Q. Liu, Z. Liao, J. Cheng, D. Xu, M. Chen, Mechanism of chip formation and surface-defects in orthogonal cutting of soft-brittle potassium dihydrogen phosphate crystals, Mater. Des. (2020) 109327.

[17] J.A. Robles-Linares, D. Axinte, Z. Liao, A. Gameros, Machining-induced thermal damage in cortical bone: necrosis and micro-mechanical integrity, Mater. Des. 197 (2020) 109215.

[18] A. Thakur, S. Gangopadhyay, State-of-the-art in surface integrity in machining of nickel-based super alloys, Int. J. Mach. Tool Manufact. 100 (2016) 25–54.

[19] I.S. Jawahir, E. Brinksmeier, R. M'saoubi, D.K. Aspinwall, J.C. Outeiro, D. Meyer, D. Umbrello, A.D. Jayal, Surface integrity in material removal processes: recent advances, CIRP Ann 60 (2011) 603–626.

[20] R. M'Saoubi, J.C. Outeiro, H. Chandrasekaran, O.W. Dillon Jr., I.S. Jawahir, A review of surface integrity in machining and its impact on functional performance and life of machined products, Int. J. Sustain. Manuf. 1 (2008) 203–236.

[21] D. Ulutan, T. Ozel, Machining induced surface integrity in titanium and nickel alloys: a review, Int. J. Mach. Tool Manufact. 51 (2011) 250–280.

[22] A.F. El-Sayed, Aircraft Propulsion and Gas Turbine Engines, CRC Press, 2017.

[23] Y.C. Ge, Z. Zhu, D. Wang, Z. Ma, D. Zhu, Study on material removal mechanism of electrochemical deep grinding, J. Mater. Process. Technol. 271 (2019) 510–519, https://doi.org/10.1016/j.jmatprotec.2019.04.033.

[24] L. Chang, L. Volpe, Y.L. Wang, M.G. Burke, A. Maurotto, D. Tice, S. Lozano-Perez, F. Scenini, Effect of machining on stress corrosion crack initiation in warm-forged type 304L stainless steel in high temperature water, Acta Mater. 165 (2019) 203–214.

[25] U. Zupanc, J. Grum, Effect of pitting corrosion on fatigue performance of shot-peened aluminium alloy 7075-T651, J. Mater. Process. Technol. 210 (2010) 1197–1202.

[26] Z. Pu, G.L. Song, S. Yang, J.C. Outeiro, O.W. Dillon, D.A. Puleo, I.S. Jawahir, Grain refined and basal textured surface produced by burnishing for improved corrosion performance of AZ31B Mg alloy, Corrosion Sci. 57 (2012) 192–201, https://doi.org/10.1016/j.corsci.2011.12.018.

[27] G.D. Revankar, R. Shetty, S.S. Rao, V.N. Gaitonde, Wear resistance enhancement of titanium alloy (Ti-6Al-4V) by ball burnishing process, J. Mater. Res. Technol. 6 (2017) 13–32, https://doi.org/10.1016/j.jmrt.2016.03.007.

[28] A.I. Hovorun, P. T, K.V. Berladir, V.I. Pererva, S.G. Rudenko, Martynov, Modern Materials for Automotive Industry, 2017.

[29] D. Axinte, Y. Guo, Z. Liao, A.J. Shih, R. M'Saoubi, N. Sugita, Machining of biocompatible materials — recent advances, CIRP Ann 68 (2019) 629–652, https://doi.org/10.1016/j.cirp.2019.05.003.

[30] Z. Liao, D. Axinte, M. Mieszala, R. M'Saoubi, A. Abelhafeez, J. Michler, M. Hardy, On the Influence of Gamma Prime upon Machining of Advanced Nickel Based Superalloy, CIRP Ann, 2018.

[31] F.S. Rad Hr, M.H. Idris, M.R. Kadir, Microstructure analysis and corrosion behavior of biodegradable Mg–Ca implant alloys, Mater. Des. 33 (2012) 88–97.

[32] Z. Shang, Z. Liao, J.A. Sarasua, J. Billingham, D. Axinte, On modelling of laser assisted machining: forward and inverse problems for heat placement control, Int. J. Mach. Tool Manufact. 138 (2019) 36–50.

[33] G. Hajdu, D, F. Borgioli, W. Michiels, T. Insperger, Stepan, Robust stability of milling operations based on pseudospectral approach, Int. J. Mach. Tool Manufact. (2020).

[34] P. Cavaliere P, E. Cerri, Leo, Effect of heat treatments on mechanical properties and fracture behavior of a thixocast A356 aluminum alloy, J. Mater. Sci. (2004).

[35] Z. Liao, D. Xu, D. Axinte, R. M'Saoubi, J. Thelin, A. Wretland, Novel Cutting Inserts with Multi-Channel Irrigation at the Chip-Tool Interface: Modelling, Design and Experiments, CIRP Ann, 2020.

[36] F. Borchers, B. Clausen, S. Eckert, L. Ehle, J. Epp, S. Harst, M. Hettig, A. Klink, E. Kohls, H. Meyer, M. Meurer, B. Rommes, S. Schneider, R. Strunk, Comparison of different manufacturing processes of AISI 4140 steel with regard to surface modification and its influencing depth, Metals 10 (2020) 895, https://doi.org/10.3390/met10070895.

[37] J.M. Davis, M. Saei, D.P. Mohanty, A. Udupa, T. Sugihara, S. Chandrasekar, Cutting of tantalum: why it is so difficult and what can be done about it, Int. J. Mach. Tool Manufact. (2020), 103607, https://doi.org/10.1016/j.ijmachtools.2020.103607.

[38] K. Ringgaard, Y. Mohammadi, C. Merrild, O. Balling, K. Ahmadi, Optimization of material removal rate in milling of thin-walled structures using penalty cost function, Int. J. Mach. Tool Manufact. (2019), 103430, https://doi.org/10.1016/j.ijmachtools.2019.103430.

[39] W. Huang, J. Yan, Surface formation mechanism in ultraprecision diamond turning of coarse-grained polycrystalline ZnSe, Int. J. Mach. Tool Manufact. (2020), https://doi.org/10.1016/j.ijmachtools.2020.103554.

[40] H. Otalora-Ortega, P.A. Osoro, P.J. Arrazola Arriola, Analytical modeling of the uncut chip geometry to predict cutting forces in orthogonal centric turn-milling operations, Int. J. Mach. Tool Manufact. (2019), 103428, https://doi.org/10.1016/j.ijmachtools.2019.103428.

[41] X. Luo, J. Palumbo, M. Papini, J.K. Spelt, Aerodynamic focusing of an abrasive air jet and its effect on machining resolution, Int. J. Mach. Tool Manufact. (2019) 92–106, https://doi.org/10.1016/j.ijmachtools.2019.05.005.

[42] E. Brinksmeier, S. Reese, A. Klink, L. Langenhorst, T. Lübben, M. Meinke, D. Meyer, O. Riemer, J. Sölter, Underlying mechanisms for developing process signatures in manufacturing, Nanomanufacturing Metrol 1 (2018) 193–208, https://doi.org/10.1007/s41871-018-0021-z.

[43] E. Brinksmeier, R. Gläbe, F. Klocke, D.A. Lucca, Process signatures - an alternative approach to predicting functional workpiece properties, Procedia Eng 19 (2011) 44–52, https://doi.org/10.1016/j.proeng.2011.11.078.

[44] D. Grguraš, L. Sterle, P. Krajnik, F. Pušavec, A novel cryogenic machining concept based on a lubricated liquid carbon dioxide, Int. J. Mach. Tool Manufact. (2019), 103456, https://doi.org/10.1016/j.ijmachtools.2019.103456.

[45] G. Li, W. Natsu, Z. Yu, Study on quantitative estimation of bubble behavior in micro hole drilling with EDM, Int. J. Mach. Tool Manufact. (2019), 103437, https://doi.org/10.1016/j.ijmachtools.2019.103437.

[46] M. Bellotti, J. Qian, D. Reynaerts, Breakthrough phenomena in drilling micro holes by EDM, Int. J. Mach. Tool Manufact. (2019), 103436, https://doi.org/10.1016/j.ijmachtools.2019.103436.

[47] D. Cha, D. Axinte, J. Billingham, Geometrical modelling of pulsed laser ablation of high performance metallic alloys, Int. J. Mach. Tool Manufact. (2019) 78–88, https://doi.org/10.1016/j.ijmachtools.2019.04.004.

[48] V. Villerius, H. Kooiker, J. Post, Y.T. Pei, Ultrashort pulsed laser ablation of stainless steels, Int. J. Mach. Tool Manufact. (2019) 27–35, https://doi.org/10.1016/j.ijmachtools.2018.11.003.

[49] D.S. Patel, V. Sharma, V.K. Jain, J. Ramkumar, Reducing overcut in electrochemical micromachining process by altering the energy of voltage pulse using sinusoidal and triangular waveform, Int. J. Mach. Tool Manufact. (2020), 103526, https://doi.org/10.1016/j.ijmachtools.2020.103526.

[50] L. Meng, Y. Zeng, D. Zhu, Wire electrochemical micromachining of Ni-based metallic glass using bipolar nanosecond pulses, Int. J. Mach. Tool Manufact. (2019), 103439, https://doi.org/10.1016/j.ijmachtools.2019.103439.

[51] X. Rao, F. Zhang, Y. Lu, X. Luo, F. Chen, Surface and subsurface damage of reaction-bonded silicon carbide induced by electrical discharge diamond grinding, Int. J. Mach. Tool Manufact. (2020), 103564, https://doi.org/10.1016/j.ijmachtools.2020.103564.

[52] K.K. Saxena, J. Qian, D. Reynaerts, A tool-based hybrid laser-electrochemical micromachining process: experimental investigations and synergistic effects, Int. J. Mach. Tool Manufact. 155 (2020), 103569, https://doi.org/10.1016/j.ijmachtools.2020.103569.

[53] X. Yang, X. Yang, K. Kawai, K. Arima, K. Yamamura, Highly efficient planarization of sliced 4H–SiC (0001) wafer by slurryless electrochemical mechanical polishing, Int. J. Mach. Tool Manufact. (2019), 103431, https://doi.org/10.1016/j.ijmachtools.2019.103431.

[54] W. Xu, L. Zhang, Heat effect on the material removal in the machining of fibre-reinforced polymer composites, Int. J. Mach. Tool Manufact. (2019) 1–11, https://doi.org/10.1016/j.ijmachtools.2019.01.005.

[55] D. Nguyen, S. Tooptong, K.H. Park, P. Kwon, Formation mechanism of alumina layer in protecting cubic boron nitride inserts in turning cast irons, Int. J. Mach. Tool Manufact. (2020), 103539, https://doi.org/10.1016/j.ijmachtools.2020.103539.

[56] Y. I S aynak, T. Lu, Jawahir, Cryogenic machining-induced surface integrity: a review and comparison with dry, MQL, and flood-cooled machining, Mach. Sci. Technol. (2014).

[57] A. Hasçalik, M. Ay, CO2 laser cut quality of Inconel 718 nickel - based superalloy, Optic Laser. Technol. 48 (2013) 554–564, https://doi.org/10.1016/j.optlastec.2012.11.003.

[58] A. Speidel, J. Mitchell-Smith, I. Bisterov, A.T. Clare, The importance of microstructure in electrochemical jet processing, J. Mater. Process. Technol. 262 (2018) 459–470, https://doi.org/10.1016/j.jmatprotec.2018.07.022.

[59] J.W. Liu, T.M. Yue, Z.N. Guo, An analysis of the discharge mechanism in electrochemical discharge machining of particulate reinforced metal matrix composites, Int. J. Mach. Tool Manufact. 50 (2010) 86–96, https://doi.org/10.1016/j.ijmachtools.2009.09.004.

[60] M.C. Kong, D. Axinte, W. Voice, Challenges in using waterjet machining of NiTi shape memory alloys: an analysis of controlled-depth milling, J. Mater. Process. Technol. 211 (2011) 959–971, https://doi.org/10.1016/j.jmatprotec.2010.12.015.

[61] M.C. Hardy, M. Detrois, E.T. McDevitt, C. Argyrakis, V. Saraf, P.D. Jablonski, J. A. Hawk, R.C. Buckingham, H.S. Kitaguchi, S. Tin, Solving recent challenges for wrought Ni-base superalloys, Metall. Mater. Trans. (2020), https://doi.org/10.1007/s11661-020-05773-6.

[62] R. M'Saoubi, D. Axinte, S.L. Soo, C. Nobel, H. Attia, G. Kappmeyer, S. Engin, W. M. Sim, High performance cutting of advanced aerospace alloys and composite materials, CIRP Ann. - Manuf. Technol. 64 (2015) 557–580, https://doi.org/10.1016/j.cirp.2015.05.002.

[63] M. Brown, P. Crawforth, R. M'Saoubi, T. Larsson, B. Wynne, A. Mantle, H. Ghadbeigi, Quantitative characterization of machining-induced white layers in Ti–6Al–4V, Mater. Sci. Eng. 764 (2019) 138220, https://doi.org/10.1016/j.msea.2019.138220.

[64] M.C. Hardy, C.R.J. Herbert, J. Kwong, W. Li, D.A. Axinte, A.R.C. Sharman, A. Encinas-Oropesa, P.J. Withers, Characterising the integrity of machined surfaces in a powder nickel alloy used in aircraft engines, Procedia CIRP 13 (2014) 411–416.

[65] Z. Liao, M. Polyakov, O.G. Diaz, D. Axinte, G. Mohanty, X. Maeder, J. Michler, M. Hardy, Grain refinement mechanism of nickel-based superalloy by severe plastic deformation - mechanical machining case, Acta Mater. 180 (2019) 2–14, https://doi.org/10.1016/j.actamat.2019.08.059.

[66] C. Herbert, D. Axinte, M. Hardy, P.D. Brown, Investigation into the characteristics of white layers produced in a nickel-based superalloy from drilling operations, Mach. Sci. Technol. 16 (2012) 40–52.

[67] X. ping Ren, Z. qiang Liu, Microstructure refinement and work hardening in a machined surface layer induced by turning Inconel 718 super alloy, Int. J. Miner. Metall. Mater. 25 (2018) 937–949, https://doi.org/10.1007/s12613-018-1643-2.

[68] Z. Chen, M.H. Colliander, G. Sundell, R.L. Peng, J. Zhou, S. Johansson, J. Moverare, Nano-scale characterization of white layer in broached Inconel 718, Mater. Sci. Eng. 684 (2017) 373–384.

[69] Q. Wang, Z. Liu, D. Yang, A.U.H. Mohsan, Metallurgical-based prediction of stress-temperature induced rapid heating and cooling phase transformations for high speed machining Ti-6Al-4V alloy, Mater. Des. 119 (2017) 208–218, https://doi.org/10.1016/j.matdes.2017.01.076.

[70] S.B. Hosseini, U. Klement, Y. Yao, K. Ryttberg, Formation mechanisms of white layers induced by hard turning of AISI 52100 steel, Acta Mater. 89 (2015) 258–267.

[71] R. M'Saoubi, D. Axinte, C. Herbert, M. Hardy, P. Salmon, Surface integrity of nickel-based alloys subjected to severe plastic deformation by abusive drilling, CIRP Ann. - Manuf. Technol. 63 (2014) 61–64, https://doi.org/10.1016/j.cirp.2014.03.067.

[72] A. la Monaca, Z. Liao, D. Axinte, A digital approach to automatically assess the machining-induced microstructural surface integrity, J. Mater. Process. Technol. (2020) 116703.

[73] X. Xu, J. Zhang, H. Liu, Y. He, W. Zhao, Grain refinement mechanism under high strain-rate deformation in machined surface during high speed machining Ti6Al4V, Mater. Sci. Eng. 752 (2019) 167–179, https://doi.org/10.1016/j.msea.2019.03.011.

[74] Y.J. Zhao, D.T. Liang, K.C. Song, Y.H. Yan, H.N. Li, Automatic measurement of grinding-induced white layer in titanium alloys based on image processing technique, Int. J. Adv. Manuf. Technol. (2019), https://doi.org/10.1007/s00170-019-04390-x.

[75] D. Xu, Z. Liao, D. Axinte, M. Hardy, A novel method to continuously map the surface integrity and cutting mechanism transition in various cutting conditions, Int. J. Mach. Tool Manufact. (2020) 103529.

[76] L.N. Brewer, M.A. Othon, Y. Gao, B.T. Hazel, W.H. Buttrill, Z. Zhong, Comparison of diffraction methods for measurement of surface damage in superalloys, J. Mater. Res. 21 (2006) 1775–1781.

[77] R. M'Saoubi, T. Larsson, J. Outeiro, Y. Guo, S. Suslov, C. Saldana, S. Chandrasekar, Surface integrity analysis of machined Inconel 718 over multiple length scales, CIRP Ann. Technol. 61 (2012) 99–102.

[78] R. Ding, C. Knaggs, H. Li, Y.G. Li, P. Bowen, Characterization of plastic deformation induced by machining in a Ni-based superalloy, Mater. Sci. Eng., A (2020) 139104.

[79] S. Birosca, F. Di Gioacchino, S. Stekovic, M. Hardy, A quantitative approach to studying the effect of local texture and heterogeneous plastic strain on the deformation micromechanism in RR1000 nickel-based superalloy, Acta Mater. 74 (2014) 110–124, https://doi.org/10.1016/j.actamat.2014.04.039.

[80] M.P. Echlin, A. Mottura, C.J. Torbet, T.M. Pollock, A new TriBeam system for three-dimensional multimodal materials analysis, Rev. Sci. Instrum. 83 (2012) 23701, https://doi.org/10.1063/1.3680111.

[81] D. Yang, Z. Liu, Quantification of microstructural features and prediction of mechanical properties of a dual-phase Ti-6Al-4V alloy, Materials 9 (2016) 1–14, https://doi.org/10.3390/ma9080628.

[82] D. Zander, A. Klink, S. Harst, F. Klocke, C. Altenbach, Influence of machining processes on rim zone properties and high temperature oxidation behavior of 42CrMo4, Mater. Corros. 70 (2019) 2190–2204, https://doi.org/10.1002/maco.201910928.

[83] M. Brown, D. Wright, R. M'Saoubi, J. McGourlay, M. Wallis, A. Mantle, P. Crawforth, H. Ghadbeigi, Destructive and non-destructive testing methods for characterization and detection of machining-induced white layer: a review paper, CIRP J. Manuf. Sci. Technol. (2018).

[84] J. Kwong, D.A. Axinte, P.J. Withers, The sensitivity of Ni-based superalloy to hole making operations: influence of process parameters on subsurface damage and residual stress, J. Mater. Process. Technol. 209 (2009) 3968–3977, https://doi.org/10.1016/j.jmatprotec.2008.09.014.

[85] A. Pramanik, A.K. Basak, Effect of wire electric discharge machining (EDM) parameters on fatigue life of Ti-6Al-4V alloy, Int. J. Fatig. 128 (2019) 105186, https://doi.org/10.1016/j.ijfatigue.2019.105186.

[86] A.D. Spear, A.R. Ingraffea, Effect of chemical milling on low-cycle fatigue behavior of an Al-Mg-Si alloy, Corrosion Sci. 68 (2013) 144–153, https://doi.org/10.1016/j.corsci.2012.11.006.

[87] M.S. Dargusch, S. Sun, J.W. Kim, T. Li, P. Trimby, J. Cairney, Effect of tool wear evolution on chip formation during dry machining of Ti-6Al-4V alloy, Int. J. Mach. Tool Manufact. 126 (2018) 13–17.

[88] C.R.J. Herbert, D.A. Axinte, M.C. Hardy, P.D. Brown, Investigation into the characteristics of white layers produced in a nickel-based superalloy from drilling operations, Procedia Eng 19 (2011) 138–143, https://doi.org/10.1016/j.proeng.2011.11.092.

[89] D.W. Schwach, Y.B. Guo, Feasibility of producing optimal surface integrity by process design in hard turning, Mater. Sci. Eng. 395 (2005) 116–123, https://doi.org/10.1016/j.msea.2004.12.012.

[90] Q. Wang, Z. Liu, B. Wang, Q. Song, Y. Wan, Evolutions of grain size and micro-hardness during chip formation and machined surface generation for Ti-6Al-4V in high-speed machining, Int. J. Adv. Manuf. Technol. 82 (2016) 1725–1736.

[91] H. Zhang, X. Shen, A. Bo, Y. Li, H. Zhan, Y. Gu, A multiscale evaluation of the surface integrity in boring trepanning association deep hole drilling, Int. J. Mach. Tool Manufact. 123 (2017) 48–56, https://doi.org/10.1016/j.ijmachtools.2017.07.005.

[92] G. Hübschen, I. Altpeter, R. Tschuncky, H.-G. Herrmann, Materials Characterization Using Nondestructive Evaluation (NDE) Methods, Woodhead Publishing, 2016.

[93] V. Bedekar, R. Voothaluru, J. Bunn, R.S. Hyde, Measurement and prediction of through-section residual stresses in the manufacturing sequence of bearing components, CIRP Ann 68 (2019) 57–60, https://doi.org/10.1016/j.cirp.2019.03.004.

[94] Y. Umakoshi, H.Y. Yasuda, Nondestruction lifetime prediction by magnetic measurements, in: K.H.J. Buschow, R.W. Cahn, M.C. Flemings, B. Ilschner, E. J. Kramer, S. Mahajan, P. Veyssière (Eds.), Encycl. Mater. Sci. Technol., Elsevier, Oxford, 2004, pp. 1–9, https://doi.org/10.1016/B0-08-043152-6/01930-6.

[95] A. Stupakov, M. Neslušan, O. Perevertov, Detection of a milling-induced surface damage by the magnetic Barkhausen noise, J. Magn. Magn Mater. 410 (2016) 198–209, https://doi.org/10.1016/j.jmmm.2016.03.036.

[96] M. Neslušan, J. Čížek, K. Kolařík, P. Minárik, M. Čilliková, O. Melikhova, Monitoring of grinding burn via Barkhausen noise emission in case-hardened steel in large-bearing production, J. Mater. Process. Technol. 240 (2017) 104–117, https://doi.org/10.1016/j.jmatprotec.2016.09.015.

[97] Fundamentals of Energy Dispersive X-Ray Analysis, Elsevier, 1984, https://doi.org/10.1016/c2013-0-04162-x.

[98] D.E. Newbury, N.W.M. Ritchie, Is scanning electron microscopy/energy dispersive X-ray spectrometry (SEM/EDS) quantitative? Scanning 35 (2013) 141–168, https://doi.org/10.1002/sca.21041.

[99] D.J. Smith, M.R. McCartney, Microscopy applications - semiconductors, in: Encycl. Anal. Sci., second ed., Elsevier Inc., 2004, pp. 84–91, https://doi.org/10.1016/B0-12-369397-7/00394-0.

[100] J. Riches, J. Drennan, Nanostructure characterisation using electron-beam techniques, in: Nanostructure Control Mater., Elsevier, 2006, pp. 57–75, https://doi.org/10.1533/9781845691189.57.

[101] A. Klink, Wire electro discharge trueing and dressing of fine grinding wheels, CIRP Ann. - Manuf. Technol. 59 (2010) 235–238, https://doi.org/10.1016/j.cirp.2010.03.076.

[102] M. Pacella, P.W. Butler-Smith, D.A. Axinte, M.W. Fay, FIB/TEM/EELS micro/nanometric investigations of the effects of laser ablation on the diamond/binder structure in polycrystalline diamond composites, J. Mater. Process. Technol. 214 (2014) 1153–1161, https://doi.org/10.1016/j.jmatprotec.2013.10.007.

[103] J.W. Murray, M.W. Fay, M. Kunieda, A.T. Clare, TEM study on the electrical discharge machined surface of single-crystal silicon, J. Mater. Process. Technol. 213 (2013) 801–809, https://doi.org/10.1016/j.jmatprotec.2012.11.028.

[104] L.C. Ehle, S. Schneider, A. Schwedt, S. Richter, A. Klink, J. Mayer, Electron microscopic characterization of surface zones thermo-chemically modified by electrical discharge machining, J. Mater. Process. Technol. (2020) 116596, https://doi.org/10.1016/j.jmatprotec.2020.116596.

[105] J.W. Murray, J.C. Walker, A.T. Clare, Nanostructures in austenitic steel after EDM and pulsed electron beam irradiation, Surf. Coating. Technol. 259 (2014) 465–472, https://doi.org/10.1016/j.surfcoat.2014.10.045.

[106] B.D. Cullity, Elements of X-Ray Diffraction, Addison-Wesley Publishing Company, 1978.

[107] X.Y. Wang, G.K.L. Ng, Z. Liu, L. Li, L. Bradley, EPMA microanalysis of recast layers produced during laser drilling of type 305 stainless steel, Thin Solid Films 453 (2004) 84–88, https://doi.org/10.1016/j.tsf.2003.11.158.
[108] D.R. Baer, S. Thevuthasan, Characterization of thin films and coatings, in: Handb. Depos. Technol. Film. Coatings, Elsevier Inc., 2010, pp. 749–864, https://doi.org/10.1016/B978-0-8155-2031-3.00016-8.
[109] B. Li, S. Zhang, R. Wang, Y. Fang, Toward understanding of metallurgical behaviours in dry machining of hardened steel: phase transformation and surface oxidation, J. Mater. Res. Technol. 8 (2019) 3811–3821, https://doi.org/10.1016/j.jmrt.2019.06.042.
[110] K. Fan, Z. Jin, J. Guo, Z. Wang, G. Jiang, Investigation on the surface layer formed during electrochemical modification of pure iron, Appl. Surf. Sci. 466 (2019) 466–471, https://doi.org/10.1016/j.apsusc.2018.10.072.
[111] B. Panda, X-ray photoelectron spectroscopy[1], in: Mater. Charact., ASM International, 2019, pp. 757–771, https://doi.org/10.31399/asm.hb.v10.a0006639.
[112] T.F. Kelly, M.K. Miller, Atom probe tomography, Rev. Sci. Instrum. 78 (2007), 031101, https://doi.org/10.1063/1.2709758.
[113] S.M. Reddy, D.W. Saxey, W.D.A. Rickard, D. Fougerouse, S.D. Montalvo, R. Verberne, A. van Riessen, Atom probe tomography: development and application to the geosciences, Geostand. Geoanal. Res. 44 (2020) 5–50, https://doi.org/10.1111/ggr.12313.
[114] S.B. Hosseini, M. Thuvander, U. Klement, G. Sundell, K. Ryttberg, Atomic-scale investigation of carbon atom migration in surface induced white layers in high-carbon medium chromium (AISI 52100) bearing steel, Acta Mater. 130 (2017) 155–163.
[115] T.G. Molnar, S. Berezvai, A.K. Kiss, D. Bachrathy, G. Stepan, Experimental investigation of dynamic chip formation in orthogonal cutting, Int. J. Mach. Tool Manufact. (2019), https://doi.org/10.1016/j.ijmachtools.2019.103429.
[116] S. Imbrogno, S. Rinaldi, D. Umbrello, L. Filice, R. Franchi, A. Del Prete, A physically based constitutive model for predicting the surface integrity in machining of Waspaloy, Mater. Des. 152 (2018) 140–155.
[117] M. Wan, D.Y. Wen, Y.C. Ma, W.H. Zhang, On material separation and cutting force prediction in micro milling through involving the effect of dead metal zone, Int. J. Mach. Tool Manufact. (2019), https://doi.org/10.1016/j.ijmachtools.2019.103452.
[118] S. Wojciechowski, M. Matuszak, B. Powałka, M. Madajewski, R.W. Maruda, G. M. Królczyk, Prediction of cutting forces during micro end milling considering chip thickness accumulation, Int. J. Mach. Tool Manufact. (2019), https://doi.org/10.1016/j.ijmachtools.2019.103466.
[119] Z. Liao, D. Gao, Y. Lu, Z. Lv, Multi-scale hybrid HMM for tool wear condition monitoring, Int. J. Adv. Manuf. Technol. 84 (2016) 2437–2448.
[120] V.A. Shaikh, T.W. Scharf, N. Boubekri, Microlubrication machining of 1018 steel: the effect of a biodegradable lubricant on the microstructural integrity, Lubric. Sci. 29 (2017) 357–376.
[121] C.R.J. Herbert, J. Kwong, M.C. Kong, D.A. Axinte, M.C. Hardy, P.J. Withers, An evaluation of the evolution of workpiece surface integrity in hole making operations for a nickel-based superalloy, J. Mater. Process. Technol. 212 (2012) 1723–1730.
[122] F. Guo, B. Y, A.W. Warren, Hashimoto, The basic relationships between resid-ual stress, white layer, and fatigue life of hard turned and ground surfaces inrolling contact, CIRP J. Manuf. Sci. Technol. (2010).
[123] J.G. Li, M. Umemoto, Y. Todaka, K. Tsuchiya, A microstructural investigation of the surface of a drilled hole in carbon steels, Acta Mater. 55 (2007) 1397–1406.
[124] M. Rancic, C. Colin, M. Sennour, J.-P. Costes, G. Poulachon, Microstructural investigations of the white and deformed layers close to the turned surface of Ti-6Al-4V, Metall. Mater. Trans. 48 (2017) 389–402.
[125] D. Xu, Z. Liao, D. Axinte, J.A. Sarasua, R. M'Saoubi, A. Wretland, Investigation of surface integrity in laser-assisted machining of nickel based superalloy, Mater. Des. (2020) 108851, https://doi.org/10.1016/j.matdes.2020.108851.
[126] T.L. Brown, C. Saldana, T.G. Murthy, J.B. Mann, Y. Guo, L.F. Allard, A.H. King, W. D. Compton, K.P. Trumble, S. Chandrasekar, A study of the interactive effects of strain, strain rate and temperature in severe plastic deformation of copper, Acta Mater. 57 (2009) 5491–5500.
[127] S.B. Hosseini, T. Beno, U. Klement, J. Kaminski, K. Ryttberg, Cutting temperatures during hard turning—measurements and effects on white layer formation in AISI 52100, J. Mater. Process. Technol. 214 (2014) 1293–1300.
[128] J. Wang, D. Zhang, B. Wu, M. Luo, Numerical and empirical modelling of machining-induced residual stresses in ball end milling of Inconel 718, Procedia CIRP 58 (2017) 7–12.
[129] W.F. Hosford, Mechanical Behavior of Materials, Cambridge university press, 2010.
[130] V. Bedekar, J.D. Poplawsky, W. Guo, R. Shivpuri, R.S. Hyde, Atomic migration of carbon in hard turned layers of carburized bearing steel, CIRP Ann 65 (2016) 85–88.
[131] H. A T Zhang, Alpas, Quantitative evaluation of plastic strain gradients generated during orthogonal cutting of an aluminum, Mater. Sci. Eng. (2002).
[132] M.R. Shankar, B.C. Rao, S. Lee, S. Chandrasekar, A.H. King, W.D. Compton, Severe plastic deformation (SPD) of titanium at near-ambient temperature, Acta Mater. 54 (2006) 3691–3700.
[133] S.L. Zherebtsov, V. S, G.S. Dyakonov, A.A. Salem, S.P. Malysheva, G. A. Salishchev, Semiatin, Evolution of grain and subgrain structure during cold rolling, Mater. Sci. Eng. (2011).
[134] J. Zhou, V. Bushlya, P. Avdovic, J.E. Ståhl, Study of surface quality in high speed turning of Inconel 718 with uncoated and coated CBN tools, Int. J. Adv. Manuf. Technol. 58 (2012) 141–151.
[135] G.K. Dosbaeva, S.C. Veldhuis, A. Elfizy, G. Fox-Rabinovich, T. Wagg, Microscopic observations on the origin of defects during machining of direct aged (DA) Inconel 718 superalloy, J. Mater. Eng. Perform. 19 (2010) 1193–1198.
[136] S.L. Soo, R. Hood, D.K. Aspinwall, W.E. Voice, C. Sage, Machinability and surface integrity of RR1000 nickel based superalloy, CIRP Ann. - Manuf. Technol. 60 (2011) 89–92, https://doi.org/10.1016/j.cirp.2011.03.094.
[137] D.A. Axinte, N. Gindy, K. Fox, I. Unanue, Process monitoring to assist the workpiece surface quality in machining, Int. J. Mach. Tool Manufact. 44 (2004) 1091–1108, https://doi.org/10.1016/j.ijmachtools.2004.02.020.
[138] A.I. Fernández-Abia, J. Barreiro, L.N.L. De Lacalle, S. Martinez, Effect of very high cutting speeds on shearing, cutting forces and roughness in dry turning of austenitic stainless steels, Int. J. Adv. Manuf. Technol. 57 (2011) 61–71.
[139] R.S. Pawade, S.S. Joshi, P.K. Brahmankar, M. Rahman, An investigation of cutting forces and surface damage in high-speed turning of Inconel 718, J. Mater. Process. Technol. 192 (2007) 139–146.
[140] D.A. Axinte, P. Andrews, W. Li, N. Gindy, P.J. Withers, T.H.C. Childs, Turning of advanced Ni based alloys obtained via powder metallurgy route, CIRP Ann. - Manuf. Technol. 55 (2006) 117–120, https://doi.org/10.1016/s0007-8506(07)60379-5.
[141] S.L. Truesdale, Y.C. Shin, Microstructural analysis and machinability improvement of Udimet 720 via cryogenic milling, Mach. Sci. Technol. 13 (2009) 1–19.
[142] B. Susuzlu, T, Hoogstrate, A. Karpuschewski, Initial research on the ultra-high pressure waterjet up to 700 MPa, J. Mater. Process. Technol. (2004).
[143] D. Liu, T. Nguyen, J. Wang, C. Huang, Mechanisms of enhancing the machining performance in micro abrasive waterjet drilling of hard and brittle materials by vibration assistance, Int. J. Mach. Tool Manufact. (2020), https://doi.org/10.1016/j.ijmachtools.2020.103528.
[144] H. Wei, C. Peng, H. Gao, X. Wang, X. Wang, On establishment and validation of a new predictive model for material removal in abrasive flow machining, Int. J. Mach. Tool Manufact. (2019), https://doi.org/10.1016/j.ijmachtools.2018.12.003.
[145] P.L. Torrubia, D.A. Axinte, J. Billingham, Stochastic modelling of abrasive waterjet footprints using finite element analysis, Int. J. Mach. Tool Manufact. 95 (2015) 39–51.
[146] M.C. Kong, D. Srinivasu, D. Axinte, W. Voice, J. McGourlay, B. Hon, On geometrical accuracy and integrity of surfaces in multi-mode abrasive waterjet machining of NiTi shape memory alloys, CIRP Ann. - Manuf. Technol. 62 (2013) 555–558, https://doi.org/10.1016/j.cirp.2013.03.021.
[147] A. Hascalik, U. Çaydaş, H. Gürün, Effect of traverse speed on abrasive waterjet machining of Ti-6Al-4V alloy, Mater. Des. (2007), https://doi.org/10.1016/j.matdes.2006.04.020.
[148] M. Mieszala, P.L. Torrubia, D.A. Axinte, J.J. Schwiedrzik, Y. Guo, S. Mischler, J. Michler, L. Philippe, Erosion mechanisms during abrasive waterjet machining: model microstructures and single particle experiments, J. Mater. Process. Technol. 247 (2017) 92–102.
[149] H.-T. Liu, Y. Hovanski, M.E. Dahl, J. Zeng, Applications of abrasive-waterjets for machining fatigue-critical aerospace aluminum parts, in: ASME 2009 Press. Vessel. Pip. Conf., American Society of Mechanical Engineers Digital Collection, 2009, pp. 1–18.
[150] Z. Liao, I. Sanchez, D. Xu, D. Axinte, G. Augustinavicius, A. Wretland, Dual-processing by abrasive waterjet machining–A method for machining and surface modification of nickel-based superalloy, J. Mater. Process. Technol. (2020) 116768.
[151] R. Melentiev, F. Fang, Recent advances and challenges of abrasive jet machining, CIRP J. Manuf. Sci. Technol. (2018).
[152] M.C. Kong, D. Axinte, W. Voice, Aspects of material removal mechanism in plain waterjet milling on gamma titanium aluminide, J. Mater. Process. Technol. 210 (2010) 573–584, https://doi.org/10.1016/j.jmatprotec.2009.11.009.
[153] T.Y.B. Yang, W.L. Kruer, R.M. More, A.B. Langdon, Absorption of laser light in overdense plasmas by sheath inverse bremsstrahlung, Phys. Plasmas 2 (1995) 3146–3154, https://doi.org/10.1063/1.871146.
[154] G. Weyl, A. Pirri, R. Root, Laser ignition of plasma off aluminum surfaces, AIAA Pap 19 (1980) 460–469.
[155] D. Bauerle, Laser Processing and Chemistry, 2011.
[156] R. Agrawal, C.(Peggy, Wang, Laser beam machining, in: B. Bhushan (Ed.), Encycl. Nanotechnol., Springer Netherlands, Dordrecht, 2016, pp. 1739–1753, https://doi.org/10.1007/978-94-017-9780-1_101020.
[157] J.M. Fishburn, M.J. Withford, D.W. Coutts, J.A. Piper, Study of the fluence dependent interplay between laser induced material removal mechanisms in metals: vaporization, melt displacement and melt ejection, Appl. Surf. Sci. 252 (2006) 5182–5188, https://doi.org/10.1016/j.apsusc.2005.07.053.
[158] M. Stafe, N. Niculae, A. Marcus, Pulsed Laser Ablation of Solids: Basics, Theory and Applications, 2014.
[159] J.H. Cho, S.J. Na, Implementation of real-time multiple reflection and Fresnel absorption of laser beam in keyhole, J. Phys. D Appl. Phys. 39 (2006) 5372–5378, https://doi.org/10.1088/0022-3727/39/24/039.
[160] S. Anisimov, B. Kapeliovich, T. Perel'Man, Electron emission from metal surfaces exposed to ultrashort laser pulses, Sov. J. Exp. Theor. Phys. 39 (1974) 776–781.
[161] L.J. Lewis, D. Perez, Laser ablation with short and ultrashort laser pulses: basic mechanisms from molecular-dynamics simulations, Appl. Surf. Sci. 255 (2009) 5101–5106, https://doi.org/10.1016/j.apsusc.2008.07.116.
[162] P. Lorazo, L.J. Lewis, M. Meunier, Short-pulse laser ablation of solids: from phase explosion to fragmentation, Phys. Rev. Lett. 91 (2003) 1–4, https://doi.org/10.1103/PhysRevLett.91.225502.

[163] D. Perez, L.J. Lewis, Ablation of solids under femtosecond laser pulses, Phys. Rev. Lett. 89 (2002) 1–4, https://doi.org/10.1103/PhysRevLett.89.255504.
[164] D. Perez, L.J. Lewis, Molecular-dynamics study of ablation of solids under femtosecond laser pulses, Phys. Rev. B Condens. Matter 67 (2003) 1–15, https://doi.org/10.1103/PhysRevB.67.184102.
[165] A. Miotello, R. Kelly, Critical assessment of thermal models for laser sputtering at high fluences, Appl. Phys. Lett. 67 (1995) 3535, https://doi.org/10.1063/1.114912.
[166] L.V. Zhigilei, E. Leveugle, B.J. Garrison, Y.G. Yingling, M.I. Zeifman, Computer simulations of laser ablation of molecular substrates, Chem. Rev. 103 (2003) 321–347, https://doi.org/10.1021/cr010459r.
[167] L.V. Zhigilei, Z. Lin, D.S. Ivanov, Atomistic modeling of short pulse laser ablation of metals: connections between melting, spallation, and phase explosion, J. Phys. Chem. C 113 (2009) 11892–11906, https://doi.org/10.1021/jp902294m.
[168] P. Parandoush, A. Hossain, A review of modeling and simulation of laser beam machining, Int. J. Mach. Tool Manufact. 85 (2014) 135–145.
[169] H.K. Sezer, L. Li, M. Schmidt, A.J. Pinkerton, B. Anderson, P. Williams, Effect of beam angle on HAZ, recast and oxide layer characteristics in laser drilling of TBC nickel superalloys, Int. J. Mach. Tool Manufact. 46 (2006) 1972–1982.
[170] W.T. Chien, S.C. Hou, Investigating the recast layer formed during the laser trepan drilling of Inconel 718 using the Taguchi method, Int. J. Adv. Manuf. Technol. 33 (2007) 308–316, https://doi.org/10.1007/s00170-006-0454-1.
[171] A. Reck, A.T. Zeuner, M. Zimmermann, Fatigue behavior of non-optimized laser-cut medical grade Ti-6Al-4V-ELI sheets and the effects of mechanical post-processing, Metals 9 (2019) 843.
[172] F. Li, X. Chen, W. Lin, H. Pan, X. Jin, X. Hua, Nanosecond laser ablation of Al-Si coating on boron steel, Surf. Coating. Technol. 319 (2017) 129–135, https://doi.org/10.1016/j.surfcoat.2017.03.038.
[173] J. Wei, Y. Ye, Z. Sun, L. Liu, G. Zou, Control of the kerf size and microstructure in Inconel 738 superalloy by femtosecond laser beam cutting, Appl. Surf. Sci. 370 (2016) 364–372.
[174] E. György, I.N. Mihailescu, P. Serra, A. Pérez del Pino, J.L. Morenza, Crown-like structure development on titanium exposed to multipulse Nd:YAG laser irradiation, Appl. Phys. Mater. Sci. Process 74 (2002) 755–759, https://doi.org/10.1007/s003390201307.
[175] J.K.M. Garofano, H.L. Marcus, M. Aindow, Characterization of microstructural effects in a percussion laser-drilled powder metallurgy Ni-based superalloy, J. Mater. Sci. 44 (2009) 680–684, https://doi.org/10.1007/s10853-008-3177-x.
[176] J.K.M. Garofano, H.L. Marcus, M. Aindow, Nanoscale carbide precipitation in the recast layer of a percussion laser-drilled superalloy, Scripta Mater. 61 (2009) 943–946.
[177] H. Wang, G. Xu, S. Zhu, W. Zhou, N. Ren, K. Xia, Comparison of percussion laser drilling quality with and without water- based ultrasonic assistance, J. Manuf. Process. 36 (2018) 175–180, https://doi.org/10.1016/j.jmapro.2018.10.001.
[178] D.K.Y. Low, L. Li, A.G. Corfe, Effects of assist gas on the physical characteristics of spatter during laser percussion drilling of NIMONIC 263 alloy, Appl. Surf. Sci. 154 (2000) 689–695, https://doi.org/10.1016/S0169-4332(99)00427-4.
[179] W. Zhao, Z. Yu, Self-cleaning effect in high quality percussion ablating of cooling hole by picosecond ultra-short pulse laser, Optic Laser. Eng. 105 (2018) 125–131, https://doi.org/10.1016/j.optlaseng.2018.01.011.
[180] N. Ali, S. Bashir, Umm-I-Kalsoom, M. Akram, K. Mahmood, Effect of dry and wet ambient environment on the pulsed laser ablation of titanium, Appl. Surf. Sci. 270 (2013) 49–57, https://doi.org/10.1016/j.apsusc.2012.12.049.
[181] S.I. Kudryashov, A.A. Samokhvalov, E.I. Ageev, A.A. Petrov, V.P. Veiko, Ultrasonic characterization of dry and wet nanosecond laser ablation of solids, Int. J. Heat Mass Tran. 127 (2018) 1095–1100, https://doi.org/10.1016/j.ijheatmasstransfer.2018.08.104.
[182] H.W. Kang, H. Lee, A.J. Welch, Laser ablation in a liquid-confined environment using a nanosecond laser pulse, J. Appl. Phys. 103 (2008), https://doi.org/10.1063/1.2905314.
[183] N.B.S.P.H. Dahotre, Laser Fabrication and Machining of Materials, 2007.
[184] H. Wang, S. Zhu, G. Xu, W. Zhou, L. Li, D. Hua, N. Ren, K. Xia, Influence of ultrasonic vibration on percussion drilling performance for millisecond pulsed Nd : YAG laser, Optic Laser. Technol. 104 (2018) 133–139, https://doi.org/10.1016/j.optlastec.2018.02.023.
[185] J.M. Allwood, T.H.C. Childs, A.T. Clare, A.K.M. De Silva, V. Dhokia, I. M. Hutchings, R.K. Leach, D.R. Leal-Ayala, S. Lowth, C.E. Majewski, A. Marzano, J. Mehnen, A. Nassehi, E. Ozturk, M.H. Raffles, R. Roy, I. Shyha, S. Turner, Manufacturing at double the speed, J. Mater. Process. Technol. 229 (2016) 729–757, https://doi.org/10.1016/j.jmatprotec.2015.10.028.
[186] B.-S. Yuan, D. Wang, Y. Dong, W. Zhang, G.-Y. Jin, Experimental study of the morphological evolution of the millisecond–nanosecond combined-pulse laser ablation of aluminum alloy, Appl. Optic. 57 (2018) 5743, https://doi.org/10.1364/ao.57.005743.
[187] N.I. Morar, R. Roy, J. Mehnen, S. Marithumu, S. Gray, T. Roberts, J. Nicholls, Investigation of recast and crack formation in laser trepanning drilling of CMSX-4 angled holes, Int. J. Adv. Manuf. Technol. 95 (2018) 4059–4070, https://doi.org/10.1007/s00170-017-1481-9.
[188] N. Ahmed, S. Darwish, A.M. Alahmari, M.A. Shar, Micro-channels by Nd:YAG laser beam machining: fabrication, microstructures, and micro-hardness profiles, Int. J. Adv. Manuf. Technol. 85 (2016) 1955–1968, https://doi.org/10.1007/s00170-015-7257-1.
[189] G. Lu, D.W. Sokol, Y. Zhang, J.L. Dulaney, Nanosecond pulsed laser-generated stress effect inducing macro-micro-nano structures and surface topography evolution, Appl. Mater. Today. 15 (2019) 171–184, https://doi.org/10.1016/j.apmt.2019.01.005.
[190] B.S. Yilbas, S.S. Akhtar, C. Karatas, Laser trepanning of a small diameter hole in titanium alloy: temperature and stress fields, J. Mater. Process. Technol. 211 (2011) 1296–1304, https://doi.org/10.1016/j.jmatprotec.2011.02.012.
[191] B.S. Yilbas, S.S. Akhtar, C. Karatas, Laser hole cutting into Ti-6Al-4V alloy and thermal stress analysis, Int. J. Adv. Manuf. Technol. 59 (2012) 997–1008, https://doi.org/10.1007/s00170-011-3551-8.
[192] A.F.M. Arif, B.S. Yilbas, B.J.A. Aleem, Laser cutting of thick sheet metals: residual stress analysis, Optic Laser. Technol. 41 (2009) 224–232, https://doi.org/10.1016/j.optlastec.2008.07.006.
[193] A. Maeda, Y. Jin, T. Kuboki, Light press of sheet metal edge for reducing residual stress generated by laser cutting considering mechanical properties and intensity of residual stress, J. Mater. Process. Technol. 225 (2015) 178–184.
[194] D. Cha, O.G. Diaz, Z. Liao, D. Gilbert, D. Axinte, J. Kell, A. Norton, M. O'Key, M. R. Osborne, D. Main, Development of a novel system for in-situ repair of aeroengine airfoil via pulsed laser ablation, J. Manuf. Syst. 55 (2020) 126–131.
[195] X. Liu, D. Du, G. Mourou, Laser ablation and micromachining with ultrashort laser pulses, IEEE J. Quant. Electron. 33 (1997) 1706–1716, https://doi.org/10.1109/3.631270.
[196] K.M. Tanvir Ahmmed, C. Grambow, A.M. Kietzig, Fabrication of micro/nano structures on metals by femtosecond laser micromachining, Micromachines 5 (2014) 1219–1253, https://doi.org/10.3390/mi5041219.
[197] K.C. Phillips, H.H. Gandhi, E. Mazur, S.K. Sundaram, Ultrafast laser processing of materials: a review, Adv. Optic Photon 7 (2015) 684, https://doi.org/10.1364/aop.7.000684.
[198] B.N. Chichkov, C. Momma, S. Nolte, F. Von Alvensleben, A. Tünnermann, Femtosecond, picosecond and nanosecond laser ablation of solids, Appl. Phys. A 63 (1996) 109–115.
[199] H. Liu, W. Lin, Z. Lin, L. Ji, M. Hong, Self-organized periodic microholes array formation on aluminum surface via femtosecond laser ablation induced incubation effect, Adv. Funct. Mater. 29 (2019) 1–7, https://doi.org/10.1002/adfm.201903576.
[200] D. Giguère, G. Olivié, F. Vidal, S. Toetsch, G. Girard, T. Ozaki, J.-C. Kieffer, O. Nada, I. Brunette, Laser ablation threshold dependence on pulse duration for fused silica and corneal tissues: experiments and modeling, J. Opt. Soc. Am. A 24 (2007) 1562, https://doi.org/10.1364/josaa.24.001562.
[201] D. Strickland, G. Mourou, Compression of amplified chirped optical pulses, Optic Commun. 56 (1985) 219–221, https://doi.org/10.1016/0030-4018(85)90120-8.
[202] J. Byskov-Nielsen, J.M. Savolainen, M.S. Christensen, P. Balling, Ultra-short pulse laser ablation of metals: threshold fluence, incubation coefficient and ablation rates, Appl. Phys. Mater. Sci. Process 101 (2010) 97–101, https://doi.org/10.1007/s00339-010-5766-1.
[203] C. McDaniel, A. Flanagan, G.M. O'Connor, Evidence for increased incubation parameter in multi-pulse ablation of a Pt:SS alloy using a femtosecond laser at high repetition rates, Appl. Surf. Sci. 295 (2014) 1–7, https://doi.org/10.1016/j.apsusc.2013.12.034.
[204] F. Di Niso, C. Gaudiuso, T. Sibillano, F.P. Mezzapesa, A. Ancona, P.M. Lugarà, Role of heat accumulation on the incubation effect in multi-shot laser ablation of stainless steel at high repetition rates, Optic Express 22 (2014) 12200, https://doi.org/10.1364/oe.22.012200.
[205] C. Kerse, H. Kalaycloğ Lu, P. Elahi, B. Çetin, D.K. Kesim, Ö. Akçaalan, S. Yavaş, M. D. Aşlk, B. Öktem, H. Hoogland, R. Holzwarth, F.Ö. Ilday, Ablation-cooled material removal with ultrafast bursts of pulses, Nature 537 (2016) 84–88, https://doi.org/10.1038/nature18619.
[206] H. qiang Dou, C. zhen Yao, H. Liu, Y. Wan, R. jie Ding, X. dong Yuan, S. zhen Xu, Femtosecond laser ablation of Al-Mg alloy in vacuum and air, Appl. Surf. Sci. 447 (2018) 388–392, https://doi.org/10.1016/j.apsusc.2018.04.003.
[207] B.N. Zolotykh, The mechanism of electrical erosion of metals in liquid dielectric media, Sov. Phys. Tech. Phys. 4 (1959) 1370.
[208] R. Snoeys, Investigations of EDM operations by means of thermomathematical models, Ann. CIRPI. 20 (1971) 35–36.
[209] J. Tao, J. Ni, A.J. Shih, Modeling of the anode crater formation in electrical discharge machining, J. Manuf. Sci. Eng. 134 (2012) 11002–11011, https://doi.org/10.1115/1.4005303.
[210] R. Fujimoto, Observation of electrode wear phenomena, JSEME 6 (1972) 48.
[211] S. Hayakawa, T. Doke, F. Itoigawa, T. Nakamura, Observation of flying debris scattered from discharge point in EDM process, in: 16th Int. Symp. Electromachining, ISEM 2010, Shanghai Jiaotong University Press, 2010, pp. 121–125.
[212] X. Yang, J. Guo, X. Chen, M. Kunieda, Molecular dynamics simulation of the material removal mechanism in micro-EDM, Precis. Eng. (2011), https://doi.org/10.1016/j.precisioneng.2010.09.005.
[213] M. Kunieda, B. Lauwers, K.P. Rajurkar, B.M. Schumacher, Advancing EDM through fundamental insight into the process, CIRP Ann. - Manuf. Technol. 54 (2005) 599–622, https://doi.org/10.1016/s0007-8506(07)60020-1.
[214] B. Lauwers, J.P. Kruth, W. Liu, W. Eeraerts, B. Schacht, P. Bleys, Investigation of material removal mechanisms in EDM of composite ceramic materials, J. Mater. Process. Technol. 149 (2004) 347–352.
[215] X. Yang, J. Guo, X. Chen, M. Kunieda, Molecular dynamics simulation of the material removal mechanism in micro-EDM, Precis. Eng. 35 (2010) 51–57.
[216] H. Ramasawmy, L. Blunt, K.P. Rajurkar, Investigation of the relationship between the white layer thickness and 3D surface texture parameters in the die sinking EDM process, Precis. Eng. 29 (2005) 479–490.
[217] G. Cusanelli, A. Hessler-Wyser, F. Bobard, R. Demellayer, R. Perez, R. Flükiger, Microstructure at submicron scale of the white layer produced by EDM technique, J. Mater. Process. Technol. 149 (2004) 289–295.

[218] B.H. Yan, Y.C. Lin, F.Y. Huang, Surface modification of Al–Zn–Mg alloy by combined electrical discharge machining with ball burnish machining, Int. J. Mach. Tool Manufact. 42 (2002) 925–934, https://doi.org/10.1016/S0890-6955(02)00026-3.
[219] H.C. Tsai, B.H. Yan, F.Y. Huang, EDM performance of Cr/Cu-based composite electrodes, Int. J. Mach. Tool Manufact. 43 (2003) 245–252, https://doi.org/10.1016/S0890-6955(02)00238-9.
[220] A. Simchi, H. Danninger, Effects of porosity on delamination wear behaviour of sintered plain iron, Powder Metall. 47 (2004) 73–80.
[221] L. Zhang, X. Qu, B. Duan, X. He, M. Qin, Effect of porosity on wear resistance of SiCp/Cu composites prepared by pressureless infiltration, Trans. Nonferrous Metals Soc. China 18 (2008) 1076–1082, https://doi.org/10.1016/S1003-6326(08)60184-3.
[222] B. Ekmekci, Residual stresses and white layer in electric discharge machining (EDM), Appl. Surf. Sci. 253 (2007) 9234–9240.
[223] H.T. Lee, T.Y. Tai, Relationship between EDM parameters and surface crack formation, J. Mater. Process. Technol. 142 (2003) 676–683.
[224] T.Y. Tai, S.J. Lu, Improving the fatigue life of electro-discharge-machined SDK11 tool steel via the suppression of surface cracks, Int. J. Fatig. 31 (2009) 433–438, https://doi.org/10.1016/j.ijfatigue.2008.07.013.
[225] O.A.A. Zeid, On the effect of electrodischarge machining parameters on the fatigue life of AISI D6 tool steel, J. Mater. Process. Technol. 68 (1997) 27–32, https://doi.org/10.1016/b978-008042140-7/50010-x.
[226] T.M. Mower, Degradation of titanium 6Al-4V fatigue strength due to electrical discharge machining, Int. J. Fatig. 64 (2014) 84–96, https://doi.org/10.1016/j.ijfatigue.2014.02.018.
[227] K.M. Patel, P.M. Pandey, P. Venkateswara Rao, Surface integrity and material removal mechanisms associated with the EDM of Al2O3 ceramic composite, Int. J. Refract. Metals Hard Mater. 27 (2009) 892–899.
[228] D. Firrao, P. Matteis, G. Scavino, G. Ubertalli, M.G. Ienco, M.R. Pinasco, E. Stagno, R. Gerosa, B. Rivolta, A. Silvestri, G. Silva, A. Ghidini, Relationships between tensile and fracture mechanics properties and fatigue properties of large plastic mould steel blocks, Mater. Sci. Eng. A. 468–470 (2007) 193–200, https://doi.org/10.1016/j.msea.2006.07.166.
[229] C. Li, X. Xu, Y. Li, H. Tong, S. Ding, Q. Kong, L. Zhao, J. Ding, Effects of dielectric fluids on surface integrity for the recast layer in high speed EDM drilling of nickel alloy, J. Alloys Compd. 783 (2019) 95–102, https://doi.org/10.1016/j.jallcom.2018.12.283.
[230] Y. Zhang, Y. Liu, R. Ji, B. Cai, Study of the recast layer of a surface machined by sinking electrical discharge machining using water-in-oil emulsion as dielectric, Appl. Surf. Sci. 257 (2011) 5989–5997, https://doi.org/10.1016/j.apsusc.2011.01.083.
[231] B. Ekmekci, A.E. Tekkaya, A. Erden, A semi-empirical approach for residual stresses in electric discharge machining (EDM), Int. J. Mach. Tool Manufact. 46 (2006) 858–868.
[232] S. Das, M. Klotz, F. Klocke, EDM simulation: finite element-based calculation of deformation, microstructure and residual stresses, J. Mater. Process. Technol. 142 (2003) 434–451.
[233] A. Klink, Y.B. Guo, F. Klocke, Surface integrity evolution of powder metallurgical tool steel by main cut and finishing trim cuts in wire-EDM, Procedia Eng 19 (2011) 178–183, https://doi.org/10.1016/j.proeng.2011.11.098.
[234] Y.F. Luo, The dependence of interspace discharge transitivity upon the gap debris in precision electrodischarge machining, J. Mater. Process. Technol. 68 (1997) 121–131.
[235] Y.S. Wong, L.C. Lim, I. Rahuman, W.M. Tee, Near-mirror-finish phenomenon in EDM using powder-mixed dielectric, J. Mater. Process. Technol. 79 (1998) 30–40.
[236] P. Peças, E. Henriques, Influence of silicon powder-mixed dielectric on conventional electrical discharge machining, Int. J. Mach. Tool Manufact. 43 (2003) 1465–1471.
[237] H.K. Kansal, S. Singh, P. Kumar, Parametric optimization of powder mixed electrical discharge machining by response surface methodology, J. Mater. Process. Technol. 169 (2005) 427–436, https://doi.org/10.1016/j.jmatprotec.2005.03.028.
[238] J.W. Murray, R.B. Cook, N. Senin, S.J. Algodi, A.T. Clare, N. Senin, S.J. Algodi, A. T. Clare, Defect-free TiC/Si multi-layer electrical discharge coatings, Mater. Des. 155 (2018) 352–365, https://doi.org/10.1016/j.matdes.2018.06.019.
[239] F.Q. Hu, F.Y. Cao, B.Y. Song, P.J. Hou, Y. Zhang, K. Chen, J.Q. Wei, Surface properties of SiCp/Al composite by powder-mixed EDM, Procedia CIRP 6 (2013) 101–106.
[240] P. Sivaprakasam, P. Hariharan, S. Gowri, Experimental Investigations on Nano Powder Mixed Micro-wire EDM Process of Inconel-718 Alloy, 2019, https://doi.org/10.1016/j.measurement.2019.07.072.
[241] K.L. Wu, B.H. Yan, F.Y. Huang, S.C. Chen, Improvement of surface finish on SKD steel using electro-discharge machining with aluminum and surfactant added dielectric, Int. J. Mach. Tool Manufact. 45 (2005) 1195–1201, https://doi.org/10.1016/j.ijmachtools.2004.12.005.
[242] F. Klocke, D. Lung, G. Antonoglou, D. Thomaidis, The effects of powder suspended dielectrics on the thermal influenced zone by electrodischarge machining with small discharge energies, J. Mater. Process. Technol. 149 (2004) 191–197, https://doi.org/10.1016/j.jmatprotec.2003.10.036.
[243] S.L. Chen, M.H. Lin, G.X. Huang, C.C. Wang, Research of the recast layer on implant surface modified by micro-current electrical discharge machining using deionized water mixed with titanium powder as dielectric solvent, Appl. Surf. Sci. 311 (2014) 47–53, https://doi.org/10.1016/j.apsusc.2014.04.204.
[244] T. Moro, N. Mohri, H. Otsubo, A. Goto, N. Saito, Study on the surface modification system with electrical discharge machine in the practical usage, J. Mater. Process. Technol. 149 (2004) 65–70, https://doi.org/10.1016/j.jmatprotec.2003.10.058.
[245] S.J. Algodi, J.W. Murray, P.D. Brown, A.T. Clare, Wear performance of TiC/Fe cermet electrical discharge coatings, Wear 402–403 (2018) 109–123, https://doi.org/10.1016/j.wear.2018.02.007.
[246] S.J. Algodi, J.W. Murray, A.T. Clare, P.D. Brown, Modelling and characterisation of electrical discharge TiC-Fe cermet coatings, Procedia CIRP 68 (2018) 28–33, https://doi.org/10.1016/j.procir.2017.12.017.
[247] J.W. Murray, S.J. Algodi, M.W. Fay, P.D. Brown, A.T. Clare, Formation mechanism of electrical discharge TiC-Fe composite coatings, J. Mater. Process. Technol. 243 (2017) 143–151, https://doi.org/10.1016/j.jmatprotec.2016.12.011.
[248] Y.-L. Hwang, C.-L. Kuo, S.-F. Hwang, The coating of TiC layer on the surface of nickel by electric discharge coating (EDC) with a multi-layer electrode, J. Mater. Process. Technol. 210 (2010) 642–652, https://doi.org/10.1016/j.jmatprotec.2009.11.013.
[249] P. Janmanee, A. Muttamara, Surface modification of tungsten carbide by electrical discharge coating (EDC) using a titanium powder suspension, Appl. Surf. Sci. 258 (2012) 7255–7265, https://doi.org/10.1016/j.apsusc.2012.03.054.
[250] T.C. Lu, J. Yang, Z. Suo, A.G. Evans, R. Hecht, R. Mehrabian, Matrix cracking in intermetallic composites caused by thermal expansion mismatch, Acta Metall. Mater. 39 (1991) 1883–1890, https://doi.org/10.1016/0956-7151(91)90157-V.
[251] N. Sumi, C. Kato, K. Shimada, T. Yuzawa, H. Teramoto, A. Mizutani, T. Kuriyagawa, Mechanism of defect generation in the TiC layer and Si layer by electrical discharge coating, Procedia CIRP 42 (2016) 221–225, https://doi.org/10.1016/j.procir.2016.02.275.
[252] A. Klink, M. Holsten, L. Hensgen, Crater morphology evaluation of contemporary advanced EDM generator technology, CIRP Ann. - Manuf. Technol. 66 (2017) 197–200, https://doi.org/10.1016/j.cirp.2017.04.137.
[253] M. Wu, J. Liu, J. He, X. Chen, Z. Guo, Fabrication of surface microstructures by mask electrolyte jet machining, Int. J. Mach. Tool Manufact. (2020), https://doi.org/10.1016/j.ijmachtools.2019.103471.
[254] G. Liu, Y. Zhang, W. Natsu, Influence of electrolyte flow mode on characteristics of electrochemical machining with electrolyte suction tool, Int. J. Mach. Tool Manufact. (2019), https://doi.org/10.1016/j.ijmachtools.2019.04.010.
[255] K.P. Rajurkar, M.M. Sundaram, A.P. Malshe, Review of electrochemical and electrodischarge machining, 2013, pp. 13–26.
[256] R.J. Leese, A. Ivanov, Electrochemical micromachining: an introduction, Adv. Mech. Eng. 8 (2016), https://doi.org/10.1177/1687814015626860, 168781401562686.
[257] W.G. Clark, J.A. McGeough, Temperature distribution along the gap in electrochemical machining, J. Appl. Electrochem. 7 (1977) 277–286, https://doi.org/10.1007/BF01059167.
[258] F. Klocke, A. Klink, D. Veselovac, D.K. Aspinwall, S.L. Soo, M. Schmidt, J. Schilp, G. Levy, J.P. Kruth, Turbomachinery component manufacture by application of electrochemical, electro-physical and photonic processes, CIRP Ann. - Manuf. Technol. 63 (2014) 703–726, https://doi.org/10.1016/j.cirp.2014.05.004.
[259] P. Vlcak, J. Fojt, J. Drahokoupil, V. Brezina, J. Sepitka, T. Horazdovsky, J. Miksovsky, F. Cerny, M. Lebeda, M. Haubner, Influence of surface pre-treatment with mechanical polishing, chemical, electrochemical and ion sputter etching on the surface properties, corrosion resistance and MG-63 cell colonization of commercially pure titanium, Mater. Sci. Eng. C (2020) 111065.
[260] F. Klocke, S. Harst, L. Ehle, M. Zeis, A. Klink, Surface integrity in electrochemical machining processes: an analysis on material modifications occurring during electrochemical machining, Proc. Inst. Mech. Eng. Part B J. Eng. Manuf. 232 (2018) 578–585, https://doi.org/10.1177/0954405417703422.
[261] K.K. Saxena, J. Qian, D. Reynaerts, A review on process capabilities of electrochemical micromachining and its hybrid variants, Int. J. Mach. Tool Manufact. 127 (2018) 28–56, https://doi.org/10.1016/j.ijmachtools.2018.01.004.
[262] J. Mitchell-Smith, A. Speidel, J. Gaskell, A.T. Clare, Energy distribution modulation by mechanical design for electrochemical jet processing techniques, Int. J. Mach. Tool Manufact. 122 (2017) 32–46, https://doi.org/10.1016/j.ijmachtools.2017.05.005.
[263] V. Sharma, D.S. Patel, V.K. Jain, J. Ramkumar, Wire electrochemical micromachining: an overview, Int. J. Mach. Tool Manufact. 155 (2020) 103579, https://doi.org/10.1016/j.ijmachtools.2020.103579.
[264] R. Schuster, Electrochemical micromachining, Science 80 (289) (2000) 98–101, https://doi.org/10.1126/science.289.5476.98.
[265] R. Yi, Y. Zhang, X. Zhang, F. Fang, H. Deng, A generic approach of polishing metals via isotropic electrochemical etching, Int. J. Mach. Tool Manufact. (2020) 103517.
[266] A. Speidel, R. Su, J. Mitchell-Smith, P. Dryburgh, I. Bisterov, D. Pieris, W. Li, R. Patel, M. Clark, A.T. Clare, Crystallographic texture can be rapidly determined by electrochemical surface analytics, Acta Mater. 159 (2018) 89–101, https://doi.org/10.1016/j.actamat.2018.07.059.
[267] D. Landolt, P.F. Chauvy, O. Zinger, Electrochemical micromachining, polishing and surface structuring of metals: fundamental aspects and new developments, in: Electrochim. Acta, Elsevier Ltd, 2003, pp. 3185–3201, https://doi.org/10.1016/S0013-4686(03)00368-2.
[268] M. Datta, Jet and laser-jet electrochemical micromachining of nickel and steel, J. Electrochem. Soc. 136 (1989) 2251, https://doi.org/10.1149/1.2097282.
[269] T. Kawanaka, S. Kato, M. Kunieda, J.W. Murray, A.T. Clare, Selective surface texturing using electrolyte jet machining, in: 2nd CIRP Conf. Surf. Integr., 2014.

[270] I. Strode, M.B. Bassett, The effect of electrochemical machining on the surface integrity and mechanical properties of cast and wrought steels, Wear 109 (1986) 171–180, https://doi.org/10.1016/0043-1648(86)90262-0.
[271] D. Landolt, Fundamental aspects of electropolishing, Electrochim. Acta 32 (1987) 1–11, https://doi.org/10.1016/0013-4686(87)87001-9.
[272] J. Kozak, The effect of electrochemical machining on the fatigue strength of heat resistance alloys, Fatigue Aircr. Struct. 2011 (2011), https://doi.org/10.2478/v10164-010-0038-2.
[273] A.D. Davydov, T.B. Kabanova, V.M. Volgin, Electrochemical machining of titanium, Review, Russ. J. Electrochem. 53 (2017) 941–965, https://doi.org/10.1134/S102319351709004X.
[274] N. Casillas, Pitting corrosion of titanium, J. Electrochem. Soc. 141 (1994) 636, https://doi.org/10.1149/1.2054783.
[275] J. Soltis, Passivity breakdown, pit initiation and propagation of pits in metallic materials – Review, Corrosion Sci. 90 (2015) 5–22, https://doi.org/10.1016/j.corsci.2014.10.006.
[276] W. Liu, S. Ao, Y. Li, Z. Liu, H. Zhang, S.M. Manladan, Z. Luo, Z. Wang, Effect of anodic behavior on electrochemical machining of TB6 titanium alloy, Electrochim. Acta 233 (2017) 190–200, https://doi.org/10.1016/j.electacta.2017.03.025.
[277] D. Sazou, K. Saltidou, M. Pagitsas, Understanding the effect of bromides on the stability of titanium oxide films based on a point defect model, Electrochim. Acta 76 (2012) 48–61, https://doi.org/10.1016/j.electacta.2012.04.158.
[278] D. Baehre, A. Ernst, K. Weißhaar, H. Natter, M. Stolpe, R. Busch, Electrochemical dissolution behavior of titanium and titanium-based alloys in different electrolytes, Procedia CIRP 42 (2016) 137–142, https://doi.org/10.1016/j.procir.2016.02.208.
[279] A. Speidel, J. Mitchell-Smith, I. Bisterov, A.T. Clare, Oscillatory behaviour in the electrochemical jet processing of titanium, J. Mater. Process. Technol. 273 (2019) 116264, https://doi.org/10.1016/j.jmatprotec.2019.116264.
[280] G. Chi, D. Yi, H. Liu, Effect of roughness on electrochemical and pitting corrosion of Ti-6Al-4V alloy in 12 wt.% HCl solution at 35 °C, J. Mater. Res. Technol. 9 (2020) 1162–1174, https://doi.org/10.1016/j.jmrt.2019.11.044.
[281] W. Liu, H. Zhang, Z. Luo, C. Zhao, S. Ao, F. Gao, Y. Sun, Electrochemical micromachining on titanium using the NaCl-containing ethylene glycol electrolyte, J. Mater. Process. Technol. 255 (2018) 784–794, https://doi.org/10.1016/j.jmatprotec.2018.01.009.
[282] W. Liu, Z. Luo, M. Kunieda, Electrolyte jet machining of Ti1023 titanium alloy using NaCl ethylene glycol-based electrolyte, J. Mater. Process. Technol. 283 (2020) 116731, https://doi.org/10.1016/j.jmatprotec.2020.116731.
[283] D. Wang, Z. Zhu, N. Wang, D. Zhu, H. Wang, Investigation of the electrochemical dissolution behavior of Inconel 718 and 304 stainless steel at low current density in NaNO3 solution, Electrochim. Acta 156 (2015) 301–307, https://doi.org/10.1016/j.electacta.2014.12.155.
[284] Y. Zeng, H. Ji, X. Fang, Y. Wang, N. Qu, Analysis and reduction of stray-current attack in reciprocated traveling wire electrochemical machining, Adv. Mech. Eng. 6 (2014) 505932, https://doi.org/10.1155/2014/505932.
[285] X. Wang, N. Qu, X. Fang, Reducing stray corrosion in jet electrochemical milling by adjusting the jet shape, J. Mater. Process. Technol. 264 (2019) 240–248, https://doi.org/10.1016/j.jmatprotec.2018.09.017.
[286] P.T. Pajak, A.K.M. Desilva, D.K. Harrison, J.A. Mcgeough, Precision and efficiency of laser assisted jet electrochemical machining, Precis. Eng. 30 (2006) 288–298, https://doi.org/10.1016/j.precisioneng.2005.09.006.
[287] M.M. Lohrengel, K.P. Rataj, T. Münninghoff, Electrochemical Machining—mechanisms of anodic dissolution, Electrochim. Acta 201 (2016) 348–353, https://doi.org/10.1016/j.electacta.2015.12.219.
[288] M. Burger, L. Koll, E.A. Werner, A. Platz, Electrochemical machining characteristics and resulting surface quality of the nickel-base single-crystalline material LEK94, J. Manuf. Process. 14 (2012) 62–70, https://doi.org/10.1016/j.jmapro.2011.08.001.
[289] X. Wang, N. Qu, P. Guo, X. Fang, X. Lin, Electrochemical machining properties of the laser rapid formed inconel 718 alloy in NaNO 3 solution, J. Electrochem. Soc. 164 (2017), https://doi.org/10.1149/2.1221714jes. E548–E559.
[290] J. Kozak, M. Zybura-Skrabalak, Some problems of surface roughness in electrochemical machining (ECM), Procedia CIRP 42 (2016) 101–106, https://doi.org/10.1016/j.procir.2016.02.198.
[291] T. Haisch, E.J. Mittemeijer, J.W. Schultze, On the influence of microstructure and carbide content of steels on the electrochemical dissolution process in aqueous NaCl-electrolytes, Mater. Corros. 53 (2002) 740–755, https://doi.org/10.1002/1521-4176(200210)53:10<740::AID-MACO740>3.0.CO;2-J.
[292] F. Klocke, S. Harst, F. Karges, M. Zeis, A. Klink, Modeling of the electrochemical dissolution process for a two-phase material in a passivating electrolyte system, Procedia CIRP 58 (2017) 169–174, https://doi.org/10.1016/j.procir.2017.03.214.
[293] M.M. Malouche, N. Stein, J. Lecomte, C. Boulanger, M. Rancic, Influence of the electrolyte composition on the electrochemical dissolution behavior of forged Inconel 718, J. Appl. Electrochem. 50 (2020) 197–206, https://doi.org/10.1007/s10800-019-01386-z.
[294] D. Zhu, L. Yu, R. Zhang, Dissolution effects with different microstructures of inconel 718 on surface integrity in electrochemical machining, J. Electrochem. Soc. 165 (2018), https://doi.org/10.1149/2.0761816jes. E872–E878.
[295] M. Datta, Anodic dissolution of metals at high rates, IBM J. Res. Dev. 37 (1993) 207–226, https://doi.org/10.1147/rd.372.0207.
[296] M.M. Lohrengel, C. Rosenkranz, Microelectrochemical surface and product investigations during electrochemical machining (ECM) in NaNO3, Corrosion Sci. 47 (2005) 785–794, https://doi.org/10.1016/j.corsci.2004.07.023.
[297] Z. Liao, D. Axinte, D. Gao, On modelling of cutting force and temperature in bone milling, J. Mater. Process. Technol. 266 (2019) 627–638.
[298] V. Kryzhanivskyy, R.M. Saoubi, J.E. Ståhl, V. Bushlya, Tool–chip thermal conductance coefficient and heat flux in machining: theory, model and experiment, Int. J. Mach. Tool Manufact. (2019), 103468, https://doi.org/10.1016/j.ijmachtools.2019.103468.
[299] C.F. Yao, Q.C. Jin, X.C. Huang, D.X. Wu, J.X. Ren, D.H. Zhang, Research on surface integrity of grinding inconel718, Int. J. Adv. Manuf. Technol. 65 (2013) 1019–1030, https://doi.org/10.1007/s00170-012-4236-7.
[300] C.H. Che-Haron, A. Jawaid, The effect of machining on surface integrity of titanium alloy Ti-6% Al-4% v, J. Mater. Process. Technol. 166 (2005) 188–192, https://doi.org/10.1016/j.jmatprotec.2004.08.012.
[301] M.H. Sadeghi, M.J. Haddad, T. Tawakoli, M. Emami, Minimal quantity lubrication-MQL in grinding of Ti–6Al–4V titanium alloy, Int. J. Adv. Manuf. Technol. 44 (2009) 487–500.
[302] J.C. Outeiro, J.C. Pina, R. M'saoubi, F. Pusavec, I.S. Jawahir, Analysis of residual stresses induced by dry turning of difficult-to-machine materials, CIRP Ann. Technol. 57 (2008) 77–80.
[303] J.C. Outeiro, A.C. Batista, M.J. Marques, Residual stresses induced by dry and cryogenic cooling during machining of AZ31B magnesium alloy, in: Adv. Mater. Res., Trans Tech Publ, 2014, pp. 658–663.
[304] A.B. Sadat, Effect of high cutting speed on surface integrity of AISI 4340 steel during turning, Mater. Sci. Technol. 6 (1990) 371–375, https://doi.org/10.1179/mst.1990.6.4.371.
[305] N. Krstulović, S. Shannon, R. Stefanuik, C. Fanara, Underwater-laser drilling of aluminum, Int. J. Adv. Manuf. Technol. 69 (2013) 1765–1773, https://doi.org/10.1007/s00170-013-5141-4.
[306] B. Adelmann, C. Ngo, R. Hellmann, High aspect ratio cutting of metals using water jet guided laser, Int. J. Adv. Manuf. Technol. 80 (2015) 2053–2060, https://doi.org/10.1007/s00170-015-7161-8.
[307] H. Zhu, J. Wang, P. Yao, C. Huang, Heat transfer and material ablation in hybrid laser-waterjet microgrooving of single crystalline germanium, Int. J. Mach. Tool Manufact. 116 (2017) 25–39, https://doi.org/10.1016/j.ijmachtools.2017.01.002.
[308] Y. Wang, Z. Zhang, G. Zhang, B. Wang, W. Zhang, Study on immersion waterjet assisted laser micromachining process, J. Mater. Process. Technol. 262 (2018) 290–298.
[309] S. Mullick, Y.K. Madhukar, S. Roy, A.K. Nath, An investigation of energy loss mechanisms in water-jet assisted underwater laser cutting process using an analytical model, Int. J. Mach. Tool Manufact. 91 (2015) 62–75.
[310] Y.K. Madhukar, S. Mullick, A.K. Nath, Development of a water-jet assisted laser paint removal process, Appl. Surf. Sci. 286 (2013) 192–205, https://doi.org/10.1016/j.apsusc.2013.09.046.
[311] M. Coteață, H.P. Schulze, L. Slătineanu, Drilling of difficult-to-cut steel by electrochemical discharge machining, Mater. Manuf. Process. 26 (2011) 1466–1472, https://doi.org/10.1080/10426914.2011.557286.
[312] M. Hajian, M.R. Razfar, S. Movahed, A.H. Etefagh, Experimental and Numerical Investigations of Machining Depth for Glass Material in Electrochemical Discharge Milling ☆, 2017, https://doi.org/10.1016/j.precisioneng.2017.10.007.
[313] M. Goud, A.K. Sharma, C. Jawalkar, A review on material removal mechanism in electrochemical discharge machining (ECDM) and possibilities to enhance the material removal rate, Precis. Eng. 45 (2016) 1–17, https://doi.org/10.1016/j.precisioneng.2016.01.007.
[314] Z. Xu, C. Zhang, A tube electrode high-speed electrochemical discharge drilling method without recast layer, in: Procedia CIRP, Elsevier B.V., 2018, pp. 778–782, https://doi.org/10.1016/j.procir.2017.12.154.
[315] X. Zhu, Y. Liu, J. Zhang, K. Wang, H. Kong, Ultrasonic-assisted electrochemical drill-grinding of small holes with high-quality, J. Adv. Res. 23 (2020) 151–161, https://doi.org/10.1016/j.jare.2020.02.010.
[316] B.K. Bhuyan, C. Garg, L. Gupta, Design and development of tabletop electrochemical grinding setup, in: Mater. Today Proc., Elsevier Ltd, 2020, pp. 1479–1482, https://doi.org/10.1016/j.matpr.2019.11.058.
[317] D.T. Curtis, S.L. Soo, D.K. Aspinwall, C. Sage, Electrochemical superabrasive machining of a nickel-based aeroengine alloy using mounted grinding points, CIRP Ann. - Manuf. Technol. 58 (2009) 173–176, https://doi.org/10.1016/j.cirp.2009.03.074.
[318] H. Li, S. Fu, Q. Zhang, S. Niu, N. Qu, Simulation and experimental investigation of inner-jet electrochemical grinding of GH4169 alloy, Chin. J. Aeronaut. 31 (2018) 608–616, https://doi.org/10.1016/j.cja.2017.08.014.
[319] Y. Yang, H. Li, Z. Liao, D. Axinte, W. Zhu, A. Beaucamp, Controlling of compliant grinding for low-rigidity components, Int. J. Mach. Tool Manufact. (2020) 103543.
[320] W. Le Zhu, A. Beaucamp, Compliant grinding and polishing: a review, Int. J. Mach. Tool Manufact. (2020), https://doi.org/10.1016/j.ijmachtools.2020.103634.
[321] Y. Mizoue, B. Sencer, A. Beaucamp, Identification and optimization of CNC dynamics in time-dependent machining processes and its validation to fluid jet polishing, Int. J. Mach. Tool Manufact. (2020), 103648, https://doi.org/10.1016/j.ijmachtools.2020.103648.
[322] J. Zhang, H. Wang, A. Senthil Kumar, M. Jin, Experimental and theoretical study of internal finishing by a novel magnetically driven polishing tool, Int. J. Mach. Tool Manufact. (2020), https://doi.org/10.1016/j.ijmachtools.2020.103552.
[323] Z. Chen, S. Johansson, D. Gustafsson, O. Widman, R.L. Peng, J. Moverare, Effect of cooling and shot peening on residual stresses and fatigue performance of milled inconel 718, Mater. Res. Proc. 2 (2017).

[324] T. Deng, J. Li, Z. Zheng, Fundamental aspects and recent developments in metal surface polishing with energy beam irradiation, Int. J. Mach. Tool Manufact. (2020), 103472, https://doi.org/10.1016/j.ijmachtools.2019.103472.
[325] E. Willenborg, Polishing with laser radiation, in: Tailored Light 2, Laser Appl. Technol., 2011, pp. 196–202.
[326] E. V Bordatchev, A.M.K. Hafiz, O. Remus Tutunea-Fatan, Performance of laser polishing in finishing of metallic surfaces, (n.d.). https://doi.org/10.1007/s00170-014-5761-3.
[327] W. Dai, J. Li, W. Zhang, Z. Zheng, Evaluation of fluences and surface characteristics in laser polishing SKD 11 tool steel, J. Mater. Process. Technol. 273 (2019) 116241, https://doi.org/10.1016/j.jmatprotec.2019.05.022.
[328] T.L. Perry, D. Werschmoeller, X. Li, F.E. Pfefferkorn, N.A. Duffie, Pulsed laser polishing of micro-milled Ti6A14V samples, J. Manuf. Process. 11 (2009) 74–81, https://doi.org/10.1016/j.jmapro.2009.10.001.
[329] J. Zhou, C. Liao, H. Shen, X. Ding, Surface and property characterization of laser polished Ti6Al4V. https://doi.org/10.1016/j.surfcoat.2019.125016, 2019.
[330] Y. Uno, A. Okada, K. Uemura, P. Raharjo, T. Furukawa, K. Karato, High-efficiency finishing process for metal mold by large-area electron beam irradiation, Precis. Eng. 29 (2005) 449–455.
[331] Y. Uno, A. Okada, K. Uemura, P. Raharjo, S. Sano, Z. Yu, S. Mishima, A new polishing method of metal mold with large-area electron beam irradiation, J. Mater. Process. Technol. 187–188 (2007) 77–80, https://doi.org/10.1016/j.jmatprotec.2006.11.080.
[332] A. Okada, H. Yonehara, Y. Okamoto, Fundamental study on micro-deburring by large-area EB irradiation, Procedia CIRP 5 (2013) 19–24, https://doi.org/10.1016/j.procir.2013.01.004.
[333] J.W. Murray, A.T. Clare, Repair of EDM induced surface cracks by pulsed electron beam irradiation, J. Mater. Process. Technol. 212 (2012) 2642–2651, https://doi.org/10.1016/j.jmatprotec.2012.07.018.
[334] I. Yamada, Low-energy cluster ion beam modification of surfaces, Nucl. Instrum. Methods Phys. Res. Sect. B Beam Interact. Mater. Atoms 148 (1999) 1–11, https://doi.org/10.1016/S0168-583X(98)00875-1.
[335] X.P. Zhu, M.K. Lei, T.C. Ma, Surface morphology of titanium irradiated by high-intensity pulsed ion beam, Nucl. Instrum. Methods Phys. Res. Sect. B Beam Interact. Mater. Atoms 211 (2003) 69–79, https://doi.org/10.1016/S0168-583X(03)01124-8.
[336] T. Deng, J. Li, Z. Zheng, Fundamental aspects and recent developments in metal surface polishing with energy beam irradiation, Int. J. Mach. Tool Manufact. 148 (2020) 103472.
[337] Z. Fang, Y. Zhang, R. Li, Y. Liang, H. Deng, An efficient approach for atomic-scale polishing of single-crystal silicon via plasma-based atom-selective etching, Int. J. Mach. Tool Manufact. (2020), 103649, https://doi.org/10.1016/j.ijmachtools.2020.103649.
[338] D.M. Allen, P. Shore, R.W. Evans, C. Fanara, W. O'Brien, S. Marson, W. O'Neill, Ion beam, focused ion beam, and plasma discharge machining, CIRP Ann. - Manuf. Technol. 58 (2009) 647–662, https://doi.org/10.1016/j.cirp.2009.09.007.
[339] N.I. Chkhalo, E.B. Kluenkov, A.E. Pestov, V.N. Polkovnikov, D.G. Raskin, N. N. Salashchenko, L.A. Suslov, M.N. Toropov, Manufacturing of XEUV mirrors with a sub-nanometer surface shape accuracy. https://doi.org/10.1016/j.nima.2008.12.160, 2009.
[340] G. Zhou, Y. Bi, Y. Ma, L. Wang, X. Wang, Y. Yu, A. Mutzke, Large current ion beam polishing and characterization of mechanically finished titanium alloy (Ti6Al4V) surface, Appl. Surf. Sci. 476 (2019) 905–913, https://doi.org/10.1016/j.apsusc.2019.01.120.
[341] W. Dai, J. Li, Z. Zheng, Q. Huang, Surface finishing by atmospheric pressure micro plasma beam irradiation, Mater. Manuf. Process. 31 (2016) 1216–1222, https://doi.org/10.1080/10426914.2015.1048364.
[342] H. Ramasawmy, L. Blunt, 3D surface topography assessment of the effect of different electrolytes during electrochemical polishing of EDM surfaces, Int. J. Mach. Tool Manufact. 42 (2002) 567–574, https://doi.org/10.1016/S0890-6955(01)00154-7.
[343] L.-F. Li, J.-P. Celis, Pickling of austenitic stainless steels (a review), Can. Metall. Q. 42 (2003) 365–376, https://doi.org/10.1179/cmq.2003.42.3.365.
[344] Y. Yue, C. Liu, E. Asselin, P. Shi, M. Jiang, Kinetics of passive film growth on 304 stainless steel in H 2 SO 4 pickling solution under chemical oxidation, Corrosion 74 (2018) 705–714, https://doi.org/10.5006/2680.
[345] H. Sidhom, F. Ghanem, T. Amadou, G. Gonzalez, C. Braham, Effect of electro discharge machining (EDM) on the AISI316L SS white layer microstructure and corrosion resistance, Int. J. Adv. Manuf. Technol. 65 (2013) 141–153, https://doi.org/10.1007/s00170-012-4156-6.
[346] P. Tyagi, T. Goulet, C. Riso, R. Stephenson, N. Chuenprateep, J. Schlitzer, C. Benton, F. Garcia-Moreno, Reducing the roughness of internal surface of an additive manufacturing produced 316 steel component by chempolishing and electropolishing, Addit. Manuf. 25 (2019) 32–38, https://doi.org/10.1016/j.addma.2018.11.001.